MS53035 MSE MSc Thesis

Perovskite Solar Cells

Development of Perovskite Absorber Layers synthesised by Techniques Compatible with Non-flat Substrates

Jasmeen Nespoli

Delft University of Technology
MSc Materials Science and Engineering
Faculty of Mechanical, Maritime and Materials Engineering

MS53035 MSE MSc Thesis

Perovskite Solar Cells

Development of Perovskite Absorber Layers synthesised by Techniques Compatible with Non-flat Substrates

by

Jasmeen Nespoli

to obtain the degree of Master of Science
at the Delft University of Technology,
to be defended publicly on Monday November 29, 2021 at 11:30 AM.

Student number:	5136172	
Project duration:	February 1, 2021 – November 29, 2021	
Thesis committee:	Dr. P. Taheri	TU Delft, Associate Professor & supervisor
	Dr. L. Mazzarella	TU Delft, Assistant Professor & daily supervisor
	Prof. A. J. Houtepen	TU Delft, Full Professor

TU Delft Delft University of Technology

Preface

While coming to the end of this graduation project and of my MSc in Materials Science and Engineering at the same time, I feel I have increased my awareness of the fascinating complexity of nature and of how important the role of engineers and of Science more in general is in the attempt of shaping the present towards a better future, not only for mankind but also for every living being on planet Earth. The tiny but nonetheless relevant contribution I may have in this has made me realise that I would really like research to become part of my life. In order to pursue this goal, I hope the curiosity and the zeal that have always characterised me since childhood will never abandon me in the years to come. This personal achievement have been made possible by the people that surrounded me during my years of study. For this reason, I would like to express special thanks to my daily supervisor Luana Mazzarella for the inspiration and support beyond belief; to the PhD Jin Yan for the countless hours spent together in the laboratory providing me with incommensurable professional and emotional backing; to the PhD Valentina Caselli for her more than precious help, encouragement and patience; to my supervisor Tom J. Savenije for all the fruitful conversations and the incentive in continually ask questions to myself in order to truly understand what the eyes cannot always see; to my supervisors Peyman Taheri and Olindo Isabella for taking part to the graduation project. I would also like to thank all the members of the Opto-electronic Materials group in the Chemical Engineering department for the professional but also very kind and friendly work environment they have been able to create and for the many interesting presentations. Then, I want to express my immense affection and gratitude to my parents Alessandro and Lorenza, my little brother Marco, and my relatives, in particular to my beloved grandmother Germana. Finally, I cannot forget to thank all my friends, especially Alessia, Davide, Esmeralda, Giulia, Leon, Luca, Luigi, Manas, Myrto, Roy, Sofia, Tom for always loving and believing in me, even when I was not able to do it myself. Last but not least, I can't help but express all my love to my Yang, my sister not by blood but by choice, my lifelong best friend Nabila.

Jasmeen Nespoli
Delft, November 2021

Abstract

Among the emerging photovoltaic (PV) technologies under development to supply sustainable energy worldwide, perovskite solar cells (PSCs) stood out in the last decade as one the fastest advancing solar technology to date, reaching a power conversion efficiency of 25.5% in 2020. Perovskite (PVK) absorbers show great versatility thanks to compositional and bandgap engineering, which make them attractive for multi-junction solar cells application.

In this MSc Thesis Project, multications mixed-halides PVK thin-films of composition $Cs_xFA_{1-x}PbI_{3-x}Br_x$ are developed. Multiple-source layer-by-layer thermal evaporation and sequential thermal evaporation/spin coating hybrid synthesis techniques are investigated because of their compatibility with non-flat substrates. As they would enable the conformal growth of PVK on the microsized pyramidal textured surface of a c-Si-based solar cell, the long-term goal is the application in a monolithic (2-T) PVK/Si tandem.

PVK engineering is carried out through tuning the main processing parameters with the aim of obtaining high-quality absorber layers. The optimisation of the PVK thin-films is based on criteria such as composition, phase, bandgap, crystallinity, homogeneity, uniformity and charge carrier transport properties. After optimising the annealing thermal treatment, the homogeneous and uniform thin-films resulting from the thermal evaporation of CsBr, PbI_2 and FAI show a highly crystalline photoactive α phase of PVK, as well as a sharp-edge absorption onset corresponding to a bandgap (E_g) of E_g~1.60 eV and high absorption coefficient (α) in the order of $\alpha \sim 10^4$-10^5 cm^{-1}. Then, the two-step spin coating technique is explored as a preliminary study to develop the hybrid method, with the aim of analysing the surface wettability and reactivity of an inorganic layer of PVK inorganic precursors (CsBr and PbI_2) when an organic solution (FAI in IPA) is spun on it. In spite of the optimisation of the FAI solution spun volume and concentration and the annealing parameters, the spin-coated thin-films present a mixture of photoactive and non-photoactive phases, i.e. $PbI_{2-x}Br_x$ and α-, γ- and δ-PVK phases. The ineffective interdiffusion reaction leading to inhomogeneous and non-uniform PVK thin-films shows that the processing parameters need further fine-tuning. However, as spin coating does not allow to deposit PVK on top of non-flat substrates, the thermal evaporation/spin coating hybrid method is developed. The solution of FAI in IPA has been spun on a thermally evaporated inorganic bilayer of CsBr/PbI_2. Albeit incomplete conversion to PVK is under suspicion, the resulting α-PVK thin-film shows good crystallinity and homogeneity and acceptable uniformity. It also presents high absorption (A~70%) for $\lambda \lesssim 500$ nm (blue light) and low absorption for $\lambda \gtrsim 500$ nm (from green to red light), although the bandgap of E_g~1.53 eV needs to be further optimised by adjusting the content of Cs^+ and most importantly Br^-.

On top of that, for all the synthesis techniques under research some unsuccessfully deposited PVK thin-films show signs of thermal and atmospheric degradation, leading to the decomposition of the α phase of PVK and formation of PbI_2 and other non-photoactive phases, along with poor optical properties. Such degradation phenomena, which might be ascribed to the ineffective incorporation of Cs^+ leading to structural instabilities, highlights the difficulties and limitations of PVK engineering.

This MSc Thesis Project offers the guidelines for the future improvement through further optimisation of thermal evaporation and thermal evaporation/spin coating hybrid techniques to obtain high-quality large-area fully-textured PSCs for monolithic PVK/Si tandem applications.

Contents

Acronyms

ALD Atomic Layer Deposition
ARC Anti-Reflection Coating
a-Si amorphous Silicon

BSEs Backscattered Electrons

CB Conduction Band
CBM Conduction Band Minimum
CIGS Copper Indium Gallium diselenide
CIS Cadmium Indium diselenide
CL Cathodoluminescence
c-Si crystalline Silicon

DSSC Sye-sensitized Solar Cells

EDS or **EDX** Energy-Dispersive X-ray Spectrometry
EQE External Quantum Efficiency
EPBT Energy Payback Time
ETL Electron Transport Layer

FF Fill Factor
FTO Fluorine-doped Tin Oxide
FWHM Full Width at Half Maximum

GB Grain Boundary
GIWAXS Grazing Incidence Wide Angle Scattering

HIT Heterojunction with Intrinsic Thin layer
HTL Hole Transport Layer
HV High Vacuum

IBC Interdigitated Back Contact
ITO Indium Tin Oxide
IZO Indium Zinc Oxide

LCA Life-Cycle Assessment

QCM Quartz Crystal Microbalance

PCE Power Conversion Efficiency
PL Photoluminescence
PSC Perovskite Solar Cell
PV Photovoltaics
PVK Perovskite

RT Room Temperature

SEs Secondary Electrons
SEM Scanning Electron Microscopy (or Microscope)
SHJ Silicon Heterojunction
SQ Shockley-Queisser
STP Standard Temperature and Pressure

TCO Transparent Conductive Oxide
TRMC Time-Resolved Microwave Conductivity
TRPL Time-Resolved Photoluminescence

UV-Vis-NIR Ultraviolet-Visible-Near Infrared

VB Valence Band
VBM Valence Band Maximum

XPS X-Ray Photoelectron Spectroscopy
XRD X-Ray Diffraction

2-T Two-terminal
3D Three-dimensional
3-T Three-terminal
4-T Four-terminal

1 Introduction

1.1. Global Energy Demand and Solar Energy

As reported in the Statistical Review of World Energy 2021 by BP plc, the total global primary energy consumption is equal to 556.63 EJ (~ 154619 TWh) [1]. In more detail, the electricity consumption worldwide has increased over the last decade by 2.9%, reaching 26823.2 TWh [1] in 2020. At this pace, the global electricity demand is expected to grow further to ~ 330000 TWh by 2050 [2].

To date, more than the 80% of the global energy demand is satisfied by fossil fuels [3], among which oil continues to hold the largest share of the energy mix (31.2%), followed by coal (27.2%) and natural gas (24.7%) [1]. To be more precise, more than 60% of the world's electricity is generated from fossil fuels [1, 4]. In this case, coal dominates this sector with a share of 35.1% [1]. Fossil fuels are of great concern due to the their forecast limited availability in the future and the negative effect that their consumption has on the equilibrium of planet Earth. In fact, they are the primary cause of carbon dioxide (CO_2) and other poisonous gases emissions, which eventually lead to global warming and climate changes. In 2020, 33.9 Gt of CO_2 have been released into the Earth's atmosphere [4]. The electricity generation sector accounts for the 36% of the total global energy-related CO_2 emissions [4]. As much as 30% of these come from coal-fired power plants alone [4]. The progress of this phenomenon will have calamitous consequences on humanity [3]. Thus, in order to find a sustainable balance between the continuous evolution of mankind and the preservation of the resources present in our biosphere for the future generations, the implementation of renewable energy sources for power generation is of paramount importance [2].

Nowadays, the contribution of renewable energies to global primary energy consumption is only 12.5% [1]. Nevertheless, in terms of worldwide power generation the contribution of renewables (excluding hydropower) has grown annually by an average of 15.9% over the last decade, showing a record increase of 358 TWh in 2020 for a total amount of generated electricity of 3147 TWh [1]. This corresponds to a renewables' record share of 11.71% in terms of electricity generation (Fig. 1.1(A)) [1]. However, considerable improvements are still needed to foster the energy transition from fossil fuels to renewables in the foreseeable future.

As solar energy is the most abundant energy source on planet Earth, photovoltaics (PV) surpasses by orders of magnitude the potential of all other renewable energy resources combined (Fig. 1.1(B)), it is meant to play a central role in the sustainable energy supply of the world to come [3]. In addition, solar energy is a readily available resource in most locations in the world and PV technologies have exceptional versatility of application [5]. The theoretical potential of solar power has been estimated at 89300 TW [2]. The share of solar in the global power generation mix has continually increased over the last 10 years. At the present time the world's cumulative installed PV capacity is over 707.5 GWp, which corresponds to the 27% of renewable power generation, albeit just 3.2% of power generation worldwide. In spite of that, solar power generation and solar capacity have increased strongly of respectively of 20.5% (148 TWh) and 21.5% (127 GW) in 2020 [1]. Considering the average annual solar capacity growth rate of 38.3% [1], the total cumulative installed PV capacity is estimated to rise to 5200 GWp by 2035 [2] and it is destined to increase further as the PV global market will continue to grow greatly in the future.

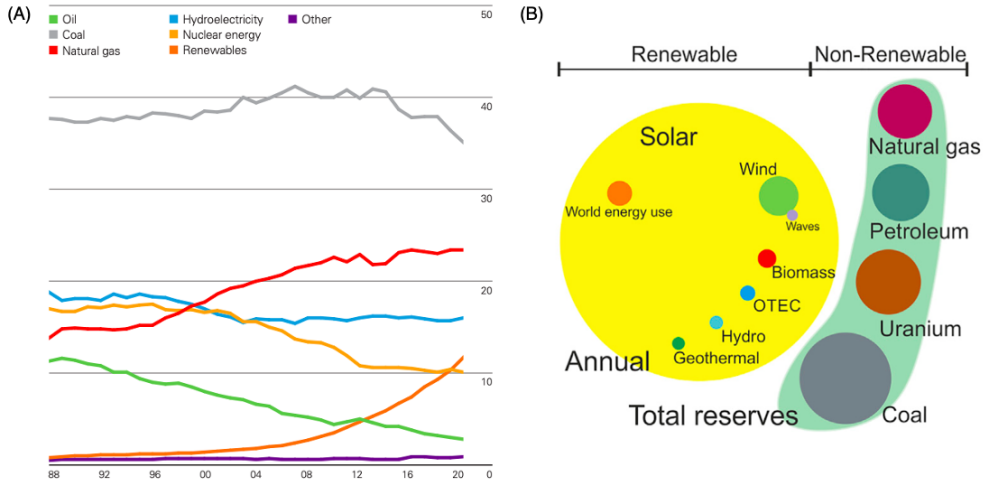

Figure 1.1: (A) Percentage share of global electricity generation by fuel over the years. Hydropower is considered separately from the other renewable resources [1]. (B) Comparison of non-renewable and renewable energy reserves on planet Earth in 2015. In this representation, nuclear energy is not considered a fully renewable energy source and thus it is included in the non-renewables category. For the non-renewable resources, total recoverable reserves are represented, whilst for the renewable ones the yearly potential is shown [3].

1.2. Photovoltaics

1.2.1. Photovoltaic Technologies

Solar cells are generally classified into three categories of PV technologies [5]:

- First-generation wafer-based crystalline silicon (c-Si) technology, in which mono- and polycrystalline silicon technologies are distinguished;
- Second-generation conventional thin-film technology, comprising gallium arsenide (GaAs), copper indium gallium diselenide (CIGS), cadmium telluride (CdTe), cadmium indium diselenide (CIS) and amorphous silicon (a-Si) thin-film PV technologies;
- The third-generation emerging thin-film technology, in which quantum dot solar cells, dye-sensitized solar cells (DSSC), organic PV solar cells and perovskite solar cells (PSCs) PV technologies can be classified.

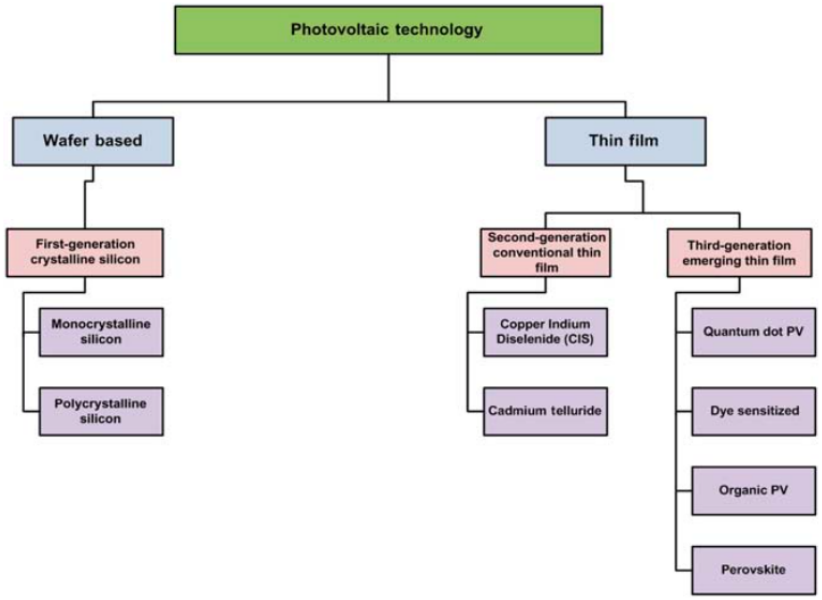

Figure 1.2: Classification of the different existent photovoltaic technologies [5].

The wafer-based crystalline silicon (c-Si) technology currently dominates the PV market, accounting for about 95% of world production in 2020 [6]. To date, the best research c-Si-based solar cell power conversion efficiency (PCE or η) is η=26.7% [7, 8]. However, this PV technology has only marginally improved during the last 15 years, with a record lab PCE which is close to the theoretical maximum one of 29.4% [9, 10]. Meanwhile, other types of new generation PV technologies are being placed at the center of the attention both scientifically and economically. In detail, emerging third-generation thin-film PV technologies are showing a strong potential thanks to properties as high efficiency, light-weight, low material use, simple manufacturing processes, flexibility, colour variation and semitransparency combined with low costs and thereby forecast low energy payback time (EPBT) [2]. Among the PV technologies falling in this category, PSCs, containing perovskite (PVK) as photoactive material, stand out as one of the fastest advancing technology in terms of PCE, starting from η=3.8% in 2009 [5, 7] and reaching over 11 years of research a record lab cell PCE of η=25.5% in 2020 (Fig. 1.3), which is a comparable value to the one of the well-established c-Si-based PV technology [7]. Interestingly, these two PV technologies can be combined in monolithic (2-T) PVK/Si tandem solar cells (see Section 2.3.2) to go beyond the PCE theorethical Shockley-Queisser (SQ) limit for a single-junction solar cell. To date, the best-performing 2-T PVK/Si tandem solar cells shows η=29.80% [11].

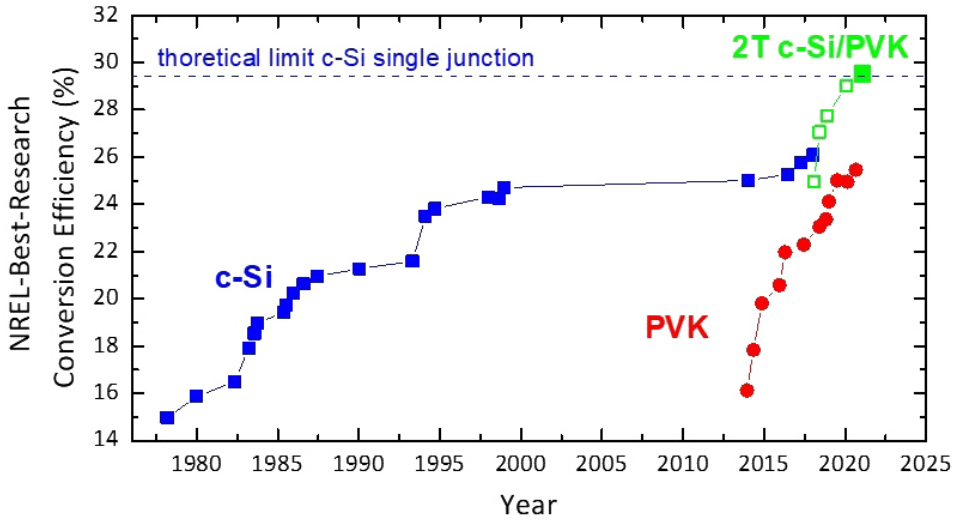

Figure 1.3: Timeline of the best reported PCEs of different PV technologies solar cells, namely c-Si- (blue squares), PVK-based solar cells (red dots) and 2T c-Si/PVK tandems (green squares). The record lab PCE for c-Si-based solar cells is η=26.7%. In detail, the best-performing c-Si-based solar cells are silicon heterostructures , which are also known as heterojunction with intrinsic thin layer (HIT). On the other side, the rapid growth of the PCE of PSCs over time has resulted in a record lab PCE of η=25.5%. The record in PCE for 2-T PVK/Si tandem has recently been broken (2021) by a solar cell presenting η=29.80% (not shown) [11]. Adapted from [7].

1.2.2. Perovskite Solar Cells

Perovskite solar cells are based on a perovskite-structured material as photoactive layer (absorber) which generates charge carriers under illumination. PVKs present an ABX_3 crystal structure (Fig. 1.4), where A is a mono/divalent cation, B is a di/tetravalent cation and X is a mono/divalent anion. Furthermore, PVKs demonstrate excellent semiconductor properties, so it guarantees the mobility of the electric charges to transport them to the adjacent layers [2, 5, 12].

As depicted by Fig. 1.4, it is possible to recognise many types of ABX_3 PVK systems. This MSc Thesis Project focuses on the most promising and currently researched hybrid organic-inorganic halide perovskites in PV applications, which present organic-inorganic atomic bonds as a consequence of the organic cation in the A site of the ABX_3 PVK crystal structure [5]. The solar cells based on these PVK systems show high absorption coefficient extended to a wide range of wavelengths, appropriate and tunable direct bandgap, high crystallinity, relatively low defect density and distinctive defect tolerance. All these characteristics lend PVK superlative charge transport properties, such as high carrier mobility and long electron and hole-diffusion lengths. As a result, high PCEs can be achieved in the relevant PSCs, which can be fabricated by combining with the PVK absorber one or more thin layers of chemically different materials (metal, plastic, ceramic materials, glass, etc.) via various multi-step processes [2, 5].

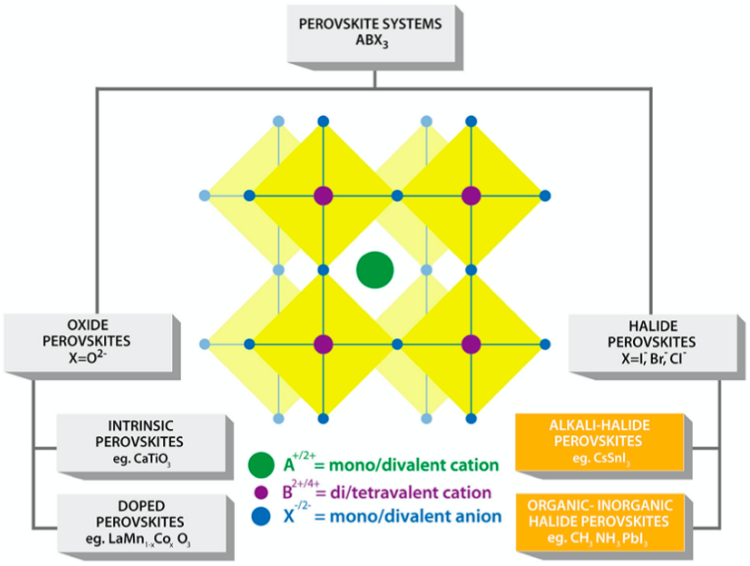

Figure 1.4: Perovskite crystal structure and classification of the different PVK systems [2].

PSCs most noteworthy properties are [2, 5]:

- High efficiency, comparable to the one of the well-established Si-based PV technology (η=26.7% [7, 8]). The record lab efficiency for PVK solar cells of η=25.5% has been reached in 2020 [7], after only 11 years of research starting from η=3.8% in 2009 [5, 7];
- Excellent light absorption properties leading to thin-film architecture, thus reduction of the total thickness, amount of materials used and weight of the solar cell;
- Versatility, namely the possibility to engineer the PVK material and the PSC architecture through selection of abundantly available, low-cost, non-hazardous and less pollutant materials, while improving the PCE;
- Prospects of utilizing PSCs in multi-junction solar cells aiming to PCE beyond the theorethical SQ limit of η=33.1% for a single-junction solar cell [13];
- Potentially very cheap scaling-up thanks to low-cost manufacturing processes;
- Color and transparency tunability;
- Flexibility;
- Forecast low EPBT, although further life-cycle assessment (LCA) studies are needed.

In spite of the extraordinary properties that make them look a really promising PV technology for the foreseeable future, PSCs have not yet been commercialised yet, being still in a development phase [5].

1.3. Objectives and Outline

The focus of this MSc Thesis is developing and optimising multications mixed-halides perovskite (PVK) absorber layers via thermal evaporation and thermal evaporation+spin coating hybrid synthesis techniques in the provision to fabricate fully-textured PSCs with inverted planar p-i-n architecture. The long-term goal is to apply the PSC as top subcell in combination with a c-Si-based bottom subcell in a monolithic tandem device. These synthesis techniques would enable to obtain high-quality large-area fully-textured multi-junction solar cells going beyond the PCE SQ limit for a single-junction solar cell [3].

The main research objectives of the herein MSc Thesis Project are:

1. Developing multications mixed-halides PVK polycrystalline thin-films of composition $Cs_xFA_{1-x}PbI_{3-x}Br_x$ via (i) multiple-source layer-by-layer thermal evaporation and (ii) thermal evaporation/spin coating hybrid synthesis techniques and exploring and optimising their processing parameters;
2. Taylor the deposition process to control the PVK thin-films composition, crystal structure, crystallinity, homogeneity, optical properties, uniformity and charge carrier transport properties;

3. Optimise the annealing thermal treatment parameters of the PVK polycrystalline thin-films.

4. Obtaining PVK thin-films presenting an homogeneous and stable photoactive dark α phase;

5. Applying the PVK compositional engineering concepts to increase the bandgap (E_g) and get close to the optimal value (E_g~1.65-1.73 eV) for a 2-T tandem solar cell application in combination with a c-Si-based solar cell;

After a general introduction about photovoltaics (Chapter 1), this MSc Thesis Project report presents the fundamental chemical, physical and optoelectronic properties of PVK. The material composition versatility and bandgap tuning through PVK engineering concepts are then expounded. This is followed by the description of the PSC inverted planar p-i-n architecture which is conceived to be placed on the top of a Si-based solar cell to create a monolithic tandem device. Moreover, the degradation phenomena of PVK are briefly analysed as one of the main problems affecting PSCs (Chapter 2). Afterwards, the precursor materials and methods used to produce multications mixed-halides PVK polycrystalline thin-films and the advantages and disadvantages of thermal evaporation, spin coating and thermal evaporation/spin coating hybrid synthesis techniques are defined, as well as the specific characterization techniques for the analysis of the so obtained PVK polycrystalline thin-films (Chapter 3). The research findings are discussed in view of highlighting the properties of the PVK absorber layers deposited via thermal evaporation (Chapter 4) and thermal evaporation/spin coating hybrid (Chapter 5) synthesis techniques and analysing the main challenges that still need to be addressed to deposit high-quality large-area PVK thin-films on non-flat substrates. The final part of the report summarises the main conclusions that can be drawn from this MSc Thesis Project about PSCs and offers some recommendations for further development of this MSc Thesis Project (Chapter 6).

2

Fundamentals

2.1. Perovskite

As described in Section 1.2.2, this MSc Thesis Project concentrates on PSCs which contain organic-inorganic halide ABX_3 PVKs as absorber layer material. The chemical, physical and optoelectronic properties of these specific PVKs are explained in the herein Section 2.1.

2.1.1. Crystal Structure

Perovskite is the name given to the naturally formed mineral of $CaTiO_3$ [5]. Perovskite-structured materials are described by the formula ABX_3 where A is a mono/divalent cation, B is a di/tetravalent cation and X is a mono/divalent anion [2, 5, 12]. A representation of the atomic arrangement in the PVK crystal structure can be seen in Fig. 2.1 [2].

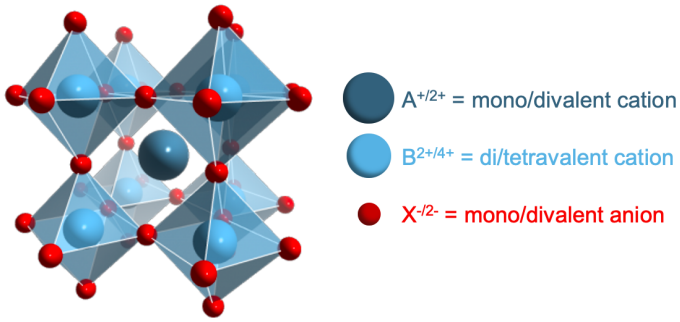

Figure 2.1: Perovskite ABX_3 crystal structure, showing its A, B and X constituents. Adapted from [14].

In the configuration of the highest symmetry resulting in the best physico-chemical and optoelectronic properties, PVK consists of an ideal ABX_3 cubic structure ($Pm\bar{3}m$ space group) made of a three-dimensional (3D) network of corner sharing BX_6 octahedra, where the B-X-B bond angle is of 180°. The X anions are defining the vertices of each octahedron at the centre of which are B cations which thus have a 6-fold coordination. The B cations form in turn cubic voids, i.e. the cubic structure itself, that can be observed by visualizing a connection between the centres of the octahedra. The A cations are placed in the center of each cubic void in a 12-fold cuboctahedral coordination, neutralizing the charge of the octahedral networks [5].

In 3D hybrid organic-inorganic ABX_3 PVK systems the two cations must have a valence equal to 3, thus showing a I-II-VII_3 PVK composition [5]. A is a monovalent organic cation, B is a smaller metal divalent cation and X is a halide anion. Typically, methylammonium (MA^+, $CH_3NH_3^+$), formamidinium (FA^+, $CH(NH_2)_2^+$), caesium (Cs^+) or rubidium (Rb^+) cations can be found in the A sites, B sites are usually occupied by lead (Pb^{2+}) or tin (Sn^{2+}) cations, while the X sites usually correspond to chlorine (Cl^-), bromine (Br^-) or iodine (I^-) anions. In spite of that, combinations of these and other ions are also studied to optimise PVK properties [5, 12]. Methylammonium lead iodide perovskite ($CH_3NH_3PbI_3$) is the most widely used and analysed [5]. This MSc Thesis report analyses the properties of PVK with composition $Cs_xFA_{1-x}PbI_{3-x}Br_x$.

Three main types of chemical bonds and molecular interactions can be found in $Cs_xFA_{1-x}PbI_{3-x}Br_x$. Firstly, the PbX_3^- anionic framework shows mixed ionic/covalent heteropolar bonds. Pb and the octahedral framework made of halide ions form hybridized orbitals. These constitute the electronic band structure, which will be described in Section 2.1.2 [5]. Secondly, intermolecular interactions between the slightly polar organic FA^+ cations in the A site and the PbX_6^- inorganic framework are present. The electric polarization of the organic cations inside the inorganic network in presence of an electric field determines the orientation disorder of the PVK structure and it may affect its paraelectric, ferroelectric, superparaelectric and antiferroelectric behaviors [5]. Finally, there is an electrostatic potential keeping the organic cations in the A sites within the inorganic frameworks. Considering the charge of the FA^+ molecule and its orientation, the nonpolar constituents in the PVK crystal structure may become polarized in a so-called charge-dipole interaction. Moreover, the small electric dipole moment of FA^+ can also polarize the X^- ions in a typical induced-dipole interaction (Debye forces). The latter correlates the molecular orientation of organic cations and the potential deformation of the inorganic framework [5].

2.1.2. Electronic Band Structure

Regarding the electronic band structures of $Cs_xFA_{1-x}PbI_{3-x}Br_x$, the valence band (VB) and conduction band (CB) derive from the sp^3d^2 hybridization of the $6s^26p^05d^0$ orbitals of lead ion and $5p^6$ and $4p^6$ orbitals of respectively iodide and bromine ions. The valence band maximum (VBM) consists of the strong hybrid antibonding state of Pb-6s orbitals, I-5p and Br-4p orbitals, while the conduction band minimum (CBM) is essentially formed by a non-bonding hybrid state of Pb-6p orbitals, I-5p and Br-4p orbitals, where the first ones contribute the most [5, 15].

The distance between the VBM and the CBM determines the energy bandgap (E_g) of PVK. This has a preeminent importance for PV applications, since it is associated with the light absorption properties of the material. PVKs are direct bandgap semiconductors. The bandgap can vary between a wide range of values and it can also be modified artificially by bandgap engineering techniques, as it will be explained in Section 2.2.2. The selection of the appropriate bandgap is crucial for certain PV applications, e.g. in case of PSC integration as top cell in a tandem device (i.e. a two-junction solar cell) with a c-Si-based bottom cell (see Section 2.3.2) [5].

2.1.3. Optoelectronic Properties

The optoelectronic properties of PVK depends on the constituents of which it is made, the stoichiometry of its structure, the deformation of its geometry and other external factors as temperature, pressure and surrounding environment. In the following Section, these properties will be analysed for 3D hybrid organic-inorganic PVKs polycrystalline thin-films (henceforth generally referred to as PVKs).

Absorption

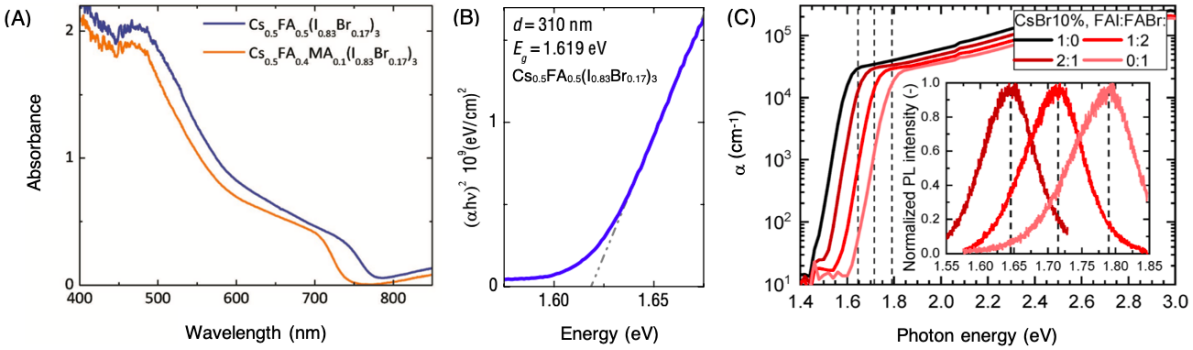

Figure 2.2: (A) Absorption spectra of two multications mixed-halides PVKs of different composition (the Pb^{2+} cation is omitted from the legend). The optical bandgap of $Cs_{0.5}FA_{0.5}Pb(I_{0.83}Br_{0.17})_3$ is around 1.62 eV [19]. (B) Bandgap estimation from the Tauc plot for $Cs_{0.5}FA_{0.5}Pb(I_{0.83}Br_{0.17})_3$ [19]. (C) Absorption coefficient as a function of the photon energy of $Cs_xFA_{1-x}Pb(I_xBr_{1-x})_3$ fabricated via sequential two-step hybrid deposition method. In the legend, the percentage shows the evaporation rates ratio between the Cs to PbI_2, whereas the proportion indicates the mixing ratio of FAI to FABr in the spin-coated solution. The absorption edges vary between 1.54 and 1.74 eV. The corresponding photoluminescence (PL) spectra is shown in the inset [20].

PVKs have outstanding light absorption properties. They are characterised by a sharp optical onset absorption, with no deep state present for photon energies below the bandgap. With regards to this, they typ-

ically show an Urbach energy in the order of a few tens of meV, which is in fact related to the low density of sub-bandgap states near the band edges [5, 16, 17]. In addition, PVKs present excellent absorption over the entire visible spectrum (Fig. 2.2(A)(B)). This properties prove the presence of a direct bandgap [5] and they also make PVKs a potential candidate for multi-junction devices. Furthermore, they are characterised by high absorption coefficient (α ~10^4-10^5 cm^{-1} [18]) showing an exponential increase higher than four orders of magnitude in the region above the bandgap [5, 18], as it can be seen in Fig. 2.3. As mentioned before, there is the possibility to modify the limits of optical absorption (i.e. the bandgap) by PVK engineering (see Section 2.2) [5] (Fig. 2.2(C)).

On top of that, PVKs exhibit superior energy utilization, i.e. a more than remarkable amount of photons energy is not lost in the conversion process from light to electricity. Standard excitonic-based, organic-based solar cells generally loose the 50% of the absorbed photon energy. Conversely, PVK solar cells show a much lower loss, as can be seen in Fig. 2.4.

In fact, less than 1 μm of material (typically ~200-400 nm [21]) is able to effectively capture the similar quantity of sunlight and collect the same number of charge carriers of much thicker absorber layers (2 μm or much more, as in the case of the average 160 μm of c-Si-based aborbers [22]) that characterise other solar cells PV technologies [5].

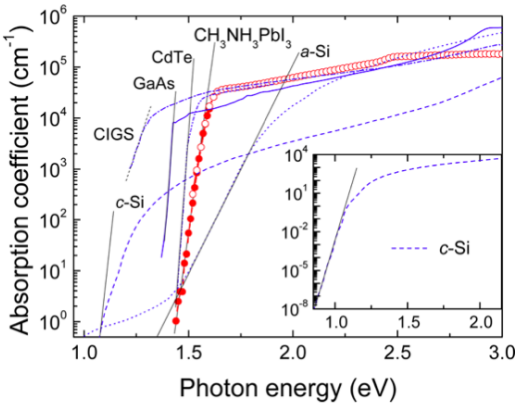

Figure 2.3: (Optical absorption coefficient as a function of the photon energy of a PVK thin-film of composition $MAPbI_3$ compared to other PV technologies materials, i.e c-Si, a-Si, GaAs, CIGS, CdTe. The slope of the Urbach tail for each material is also visible. The inset focuses on low absorption values for c-Si. Values measured at RT [18].

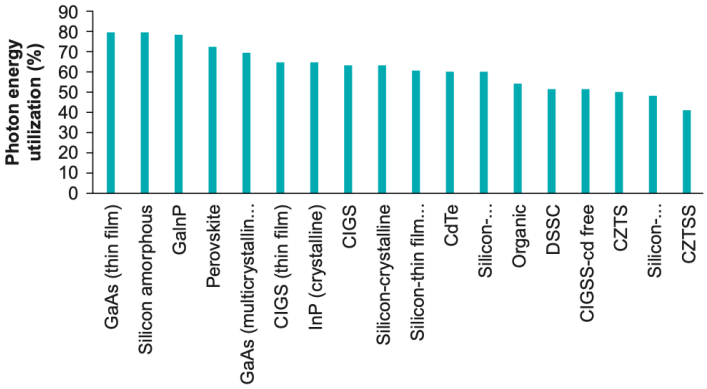

Figure 2.4: Percentage of photon energy utilisation of PVK material with respect to other PV technologies [5].

Charge-Carriers Dynamics and Transport

PVKs stand out with respect to conventional semiconductors thanks to their peculiar charge carrier dynamics and ambipolar charge transport properties [5].

PVKs generates the electron-hole pairs almost instantaneously and subsequently the excitons dissociate in few ps (~10^{-12} s) [23], given that they present a very low exciton binding energy (R^*) in the order of tens of

meV or even less compared to the thermal energy at Room Temperature (RT~298 K, which corresponds to a thermal energy of k_BT~0.025eV) and to a lot of other PV materials [24, 25].

It has been proven that the photocarrier dynamics is better described by a free carrier model than by an exciton model, although several aspects are still being researched [5].

After photogeneration, electrons are transported and injected into the electron transport layer (ETL) in less than 1 ps. On the other hand, holes are injected in the hole transport layer (HTL). The materials and functions of the transport layers belonging to a PSC architecture will be better described in Section 2.3) [5, 23].

Excellent electronic transport is shown by materials characterised by a high value of the product between the charge carrier mobility (μ) and lifetime (τ). Mobility is inversely proportional to the charge carrier effective mass (m^*) and proportional to the carrier average scattering time ($\bar{\tau}$), as shown in Eq. (10):

$$\mu = (\frac{q}{m^*})\bar{\tau} \tag{10}$$

On the other side, charge carrier lifetimes are associated with recombination and trapping probabilities. Therefore, it is important to underline that long lifetimes do not always result unquestionably in high mobilities [26].

The charge carrier effective mass is an important parameter affecting the electronic band structure and the ambipolar charge transport properties in PSCs. The higher the effective mass, the smaller the band edges curvature ($\frac{\partial^2\epsilon(k)}{\partial k^2}$) (Eq. (11)), factor that affects the determination of the bandgap, and the lower the mobility of the photocarrier into the crystal lattice [27]:

$$\frac{\partial^2\epsilon(k)}{\partial k^2} = \frac{\hbar^2}{m^*} \tag{11}$$

where $\hbar$ is the Planck constant, ϵ(k) are the band edge eigenvalues and k is the wave vector.

PVKs are characterised by small charge carrier effective masses [26], considering an ideal scenario where phonon-scattering effects, defects or any impurities are neglected [27]. For some PVK compositions as $MAPbI_3$, they are relatively in line with the values of silicon [28]. Depending on the PVK composition, the mobility may be either slightly larger for electrons than for holes suggesting an higher electron mobility or vice versa. Electrons and holes may also present the same mobility [5, 23, 29–31]. PSCs power conversion performance should be improved by engineering the materials of the different layers of the device architecture to achieve a balanced charge transport of charge carriers and the highest possible mobility values [5, 23].

PVKs polycrystalline thin-films show relatively modest charge carrier mobility (μ=1-100 cm^2/V·s) [5, 26, 32–34]. The electron and hole mobilities of PVKs can be one order of magnitude lower than those of Si and other inorganic PV materials, but much higher than organic ones. The charge carrier mobilities of popular PV materials at RT are compared in Table 2.1 [26].

Table 2.1: Comparison of charge carrier mobilities of common PV materials at RT [26].

Material	**Electron mobility ($\frac{cm^2}{Vs}$)**	**Hole mobility ($\frac{cm^2}{Vs}$)**
GaAs crystal	~8000	~400
Si crystal	~1500	~500
CdTe crystal	≤~1000	≤~100
PbTe	~6000	~4000
PbS	~600	~700
CIS crystal	1	≤~300
CZTSSe crystal	10-200	~1
Organic crystal	≤~0.1	≤~15
$MASnI_3$ crystal, pellet	1	200-300
$MAPbI_3$ and $MAPbBr_3$ crystals	≤~100	≤~100

Finally, it should be pointed out that the effective values of mobility in a real PSCs where interfacial effects are taking place can remarkably decrease with respect to PVK thin-films [5].

PVKs show also very long charge carrier lifetimes ($\tau \geq 1\mu$s) and significantly long charge carrier diffusion length for both electrons and holes ($L_D > 1\mu$m [26]) [5, 32]. The relationship between the charge carrier diffusion length, mobility and lifetime is shown in Eq. (12) [26]:

$$L_D = \sqrt{D\tau} \quad \text{where} \quad D = \frac{\mu q}{k_B T} \tag{12}$$

where D is the carrier diffusion coefficient, q is the elementary charge, k_B is the Boltzmann constant and T is the absolute temperature.

Specifically, the best-performing PVKs with composition $Cs_xFA_{1-x}PbI_{3-x}Br_x$ are characterised by superior charge carrier mobilities (11–40 $\frac{cm^2}{Vs}$) and diffusion lengths (0.8-4.4 mm) [35].

Two main theories attempt to explain the carrier dynamics and the ambipolar charge transport mechanism in PVKs, namely carrier-phonon scattering and polaron-dominated conduction [5, 26]. However, these phenomena are far from being completely understood and further theoretical models and experimental data are needed to investigate them [5, 26].

Influence of Defects and Contact Interfaces

PVKs typically exhibit high sufferance for defects and a relatively low trap-states density, which in turn justify the high crystallinity and small Urbach tail energy. The low level of material disorder leads to a low recombination rate of charge carriers and generally favours drastically higher mobilities, which in turn results in high open circuit voltage (V_{oc}). For instance, considering the open-circuit voltage of a PVK solar cell, $V_{oc,\,PVK}$>1.2 V [36, 37], which can be compared to $V_{oc,\,c\text{-}Si}$~0.76 V for a c-Si-based device [38].

However, it should be pointed out that a certain amount of defects is always present in the material. Defects origin, charge and distribution can widely vary depending on the synthesis technique, additives and light exposure conditions. In general terms, the effect of defects on chemico-physical and optoelectronic properties of PVKs is known [5]. They affect the local PL, electroluminescence, conductivity, carrier lifetime and surface potential. However, the nature and impact of material disorder in PVKs still need to be completely understood. This limits both the performance and the reproducibility of PSCs [5].

Generally, the dominant defects in PVKs are point defects with low formation energies which can only create shallow defect states near the band edges. On the other hand, the defects creating deep trap states located in the mid bandgap region present relatively high formation energies [39]. The almost total absence of deep defect states hampers the non-radiative recombination mechanisms to a great extent. In fact, this can only take place in correspondence of deep-level traps regions, which would act as recombination centers reducing the minority charge carrier lifetime and in turn the V_{oc} and the PCE. Consequently, uncommonly long carrier diffusion lengths, lifetimes and exceptional PL emissive quantum yields are observed in PVKs [5].

Interestingly, certain point defects can play the role of either donors or acceptors, which can determine whether a certain PVK is n- or p-type. By varying the synthesis technique conditions, e.g. the precursors and their proportion during PVK production, it is possible to control the type, amount and distribution of defects and form either n- or p-doped PVKs [5].

Furthermore, PVKs containing I_- ions in the X-sites seem characterised by intrinsically benign Grain Boundaries (GBs) which do not create any deeply located states. In fact, the atoms located at the GBs have similar chemical environments of defects such as individual interstitials and vacancies, thus they form only shallow trap states [39]. Although GBs act typically as electrostatic potential barriers for charge carrier transport and recombination sites in polycrystalline PV materials (Fig. 2.5(A)), in these PVKs trap states at GBs might consist of accumulated positively charged I vacancies (V_I), which might become electronically neutral when filled by photogenerated electrons during illumination (Fig. 2.5(B)). Therefore, the filled traps at GBs may be even beneficial, improving charge carrier transport and reducing recombination [40].

However, different research studies present conflicting results and it is still not fully clear how the grain boundaries act on charge carriers recombination and V_{oc} of the PSC. It seems that the exact role of GBs on recombination is dependent on the PVK synthesis technique, which induce chemical modifications on them [40].

Apart from that, GBs undoubtedly have a negative effect on the hysteresis behavior and long-term stability of the devices as they favour ion migration, as it will be explained in Section 2.4 [40].

On top of that, the contact interfaces between the PVK absorber and the neighbouring layers (ETL and HTL) play a key role for the PSC performance. The defect states in combination with ion migration phenomena at the interfaces influence the chemical, physical and optoelectronic properties of PVK. By creating trap sites lying at the sub-bandgap region of the energy bandgap, the band structure undergoes some changes, namely the position of the Fermi energy level (E_F) can shift upwards or downwards [5]. However, defect states may also act as interfacial recombination sites, thus limiting the performance of the PSC. Nonetheless,

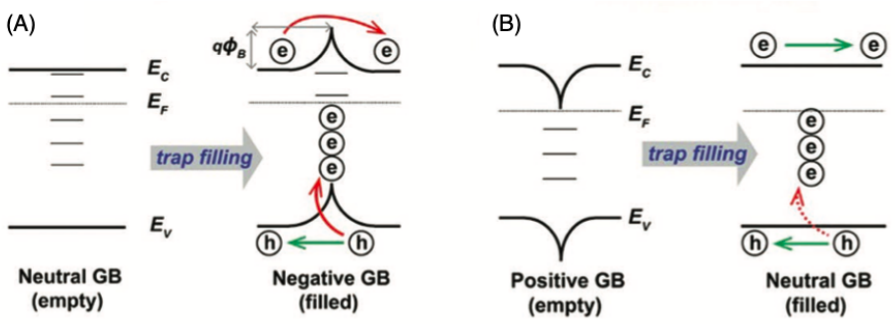

Figure 2.5: Illustration of the effect of GBs on charge carriers transport properties. (A) In polycrystalline PV materials, GBs typically create empty neutral traps, which generate a potential barrier for charge carrier transport when they are filled. (B) In PVK, empty positively charged traps are created by the accumulation of iodine vacancies. Charge carrier transport could be facilitated when the traps become neutral as soon as they are filled [40].

it is possible to passivate these surface states by incorporating certain additives or exposing it to illumination (photo-cleaning) [5]. Finally, charge accumulation can occur within the PVK absorber layer. This phenomenon increases the intrinsic bandgap of the material. Additionally, it is strictly related to the hysteresis behaviour of the device (see Section 2.4 [5].

2.2. Perovskite Engineering

2.2.1. Compositional Engineering

In the past few years the improvements in the choice of the precursor material mixtures and the great advances in synthesis techniques for PSCs production made extensive and increasingly precise manipulation of the composition and crystal structure of PVK to optimise its properties possible. The analysis proposed in the following Section will focus on 3D hybrid organic-inorganic PVKs, showing ABX_3 crystal structure (henceforth generally referred to as PVKs) [5].

It is possible to intervene on the distortion of the ideal geometry of the cubic crystal structure of PVK to tune its chemico-physical and optoelectronic properties. By varying the PVK composition, the crystal structure can be misshapen. Four deformation mechanisms are commonly observed [5]:

- Tilt of octahedral complexes;
- Off-centering of the octahedrally coordinated cations;
- Distortion of the octahedral cage;
- Off-centering of the 12-fold coordinated site.

The distortion depends on three variables, namely the size effect, the Jahn Teller effect and the change in crystal structure and composition of ABX_3 due to external perturbations, i.e. temperature, pressure and the surrounding environment (oxidative or reductive) [5]. This Section 2.2.1 focuses mainly on the size effect and temperature-dependent structural variations, i.e. phase transitions.

Size Effect

PVKs must be in the ideal cubic α phase ($Pm\bar{3}m$). As mentioned in Section 2.1.1, this configuration is not only photoactive, but it also show the best physico-chemical and optoelectronic properties. In fact, the chemical bonds in its PbX_3^- anionic framework present a high degree of ionic character in contrast with the covalent counterpart, which is favourable for charge carrier generation and transport.

In relation to the size effect, the geometrical relationship associated with the ideal cubic geometry of PVK is expressed by Eq. (13):

$$(r_A + r_X) = \sqrt{2}(r_B + r_X) \tag{13}$$

where r_A, r_B and r_X are the radii of A, B and X ions, respectively [5].

The distortion and stability of the PVK structure can be described by the ratio between the two aforementioned cell lengths indicated in Fig. 2.6. This ratio is called the Goldschmidt tolerance factor (t) and it is shown in Eq. (14):

$$t = \frac{(r_A + r_X)}{\sqrt{2}(r_B + r_X)} \tag{14}$$

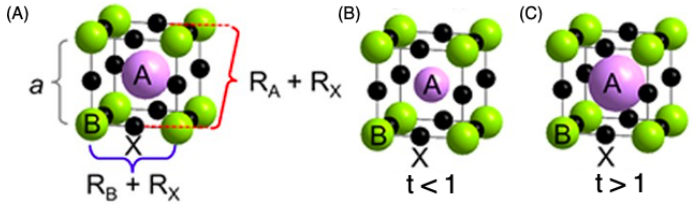

Figure 2.6: Simplified illustration of the packing of ions in an ideal cubic PVK crystal structure showing (A) PVK crystal cell with lattice constant a and cell lenghts defining the Goldschmidt tolerance factor, (B) loosely packed crystal structure with small-sized cation A and t<1 and (C) tightly packed crystal structure with large-sized cation A and t>1 [41].

The ideal cubic α phase for halide PVK exists in the range of 0.85<t<1. A change in the PVK composition due to the replacement of the A, B and X constituents modifies the value of t and it may cause a phase transition. The size of the organic cation present in the A site can reduce the symmetry of the PVK crystal structure. Its ionic radius should be greater than the one of the B cation, but it should also be smaller enough to fit in the 12-fold coordinated cubic voids created by the inorganic framework of octahedra. If the A cation is sufficiently small (t<0.85), a partial distortion of BX_6 octahedra is introduced. The B-X and A-X bonds undergo compression and tension, respectively, and the octahedra tilting to fill the void space and accommodate the induced stress. Thus, as the A cation gets smaller, crystal structures of PVK such orthorhombic and rhombohedral (or trigonal) and may be observed. On the contrary, if the A cation is bigger or alternatively the B cation is small enough (t>1), hexagonal or tetragonal phases are expected [5].

Phase Transitions

PVKs are characterised by different crystal structures at different temperatures and pressures which depend on the composition of the material (size effect).

Considering the same pressure conditions, PVK crystal structure symmetry increases with temperature. Generally, three distinct phases can be recognised, i.e. a high temperature α phase, an intermediate temperature β phase and a low-temperature γ phase. However, since they depend on the specific PVK, it is not always possible to observe all these precise phases and the nomenclature assigned to the different crystal structures may vary. For instance, certain PVKs may show a stable δ phase at RT [5]. On the other side, phase transitions to crystal structures with lower symmetry occur by increasing the pressure. Above a certain value, amorphisation of the PVK is observed [42, 43].

At ambient pressure conditions, PVK ideally presents a cubic symmetry (photoactive α-phase PVK or black phase, $Pm\bar{3}m$ space group) at RT, but phase trasformation into lower symmetry tetragonal, rhombohedral, hexagonal and orthorhombic crystal structures can be observed by decreasing the temperature while keeping the same pressure. Some of them may result stable at RT [5, 44]. The PVK phase transitions leading to crystal structures other than the cubic α phase must be avoided in the operating temperature range of a solar cell (~288-338 K) as they alter the chemical, physical and optoelectronic properties of PVK and thereby the PSC performance [5].

In the case of $Cs_xFA_{1-x}PbI_{3-x}Br_x$, the phase transitions of $FAPbI_3$ ans $CsPb_3$ can be taken as references [44]. The best-performing PVK thin-films of this composition present a small Cs^+ content between 0.1<x<0.3 [35], which determines the Br^- content too. The presence of small molar fractions of Cs^+ and Br^- ions replacing FA^+ ions in the A sites and I^- ions in the X-sites respectively creates a slight distortion of the crystal structure [44]. With regards to the cations in the A sites, $FAPbI_3$ and $CsPbI_3$ α phases exist at the upper (large ionic radius) and lower limit (small ionic radius) of the Goldschmidt tolerance factor range, respectively. Thus, the mixture of FA^+ and Cs^+ ions in the A sites generates a stable pseudo-cubic α phase. In addition, these cations counteract the propensity of both these PVKs to transform into the unwanted δ phases [35]. In fact, the main issue of $Cs_xFA_{1-x}PbI_{3-x}Br_x$ is the transition from the photoactive cubic α phase (dark phase) to the non-photoactive δ phase (yellow phase) which may occur at RT. Nevertheless, the α phase can be restored at high temperature [44]. On the other side, the mixing of I^- and Br_- in the X-sites principally reduces the Goldschmidt tolerance factor and modifies the octahedra tilting of a certain angle ϕ [44].

The crystal structures of both $FAPbI_3$ and $CsPbI_3$ at different temperatures are illustrated in (Fig. 2.7) [44].

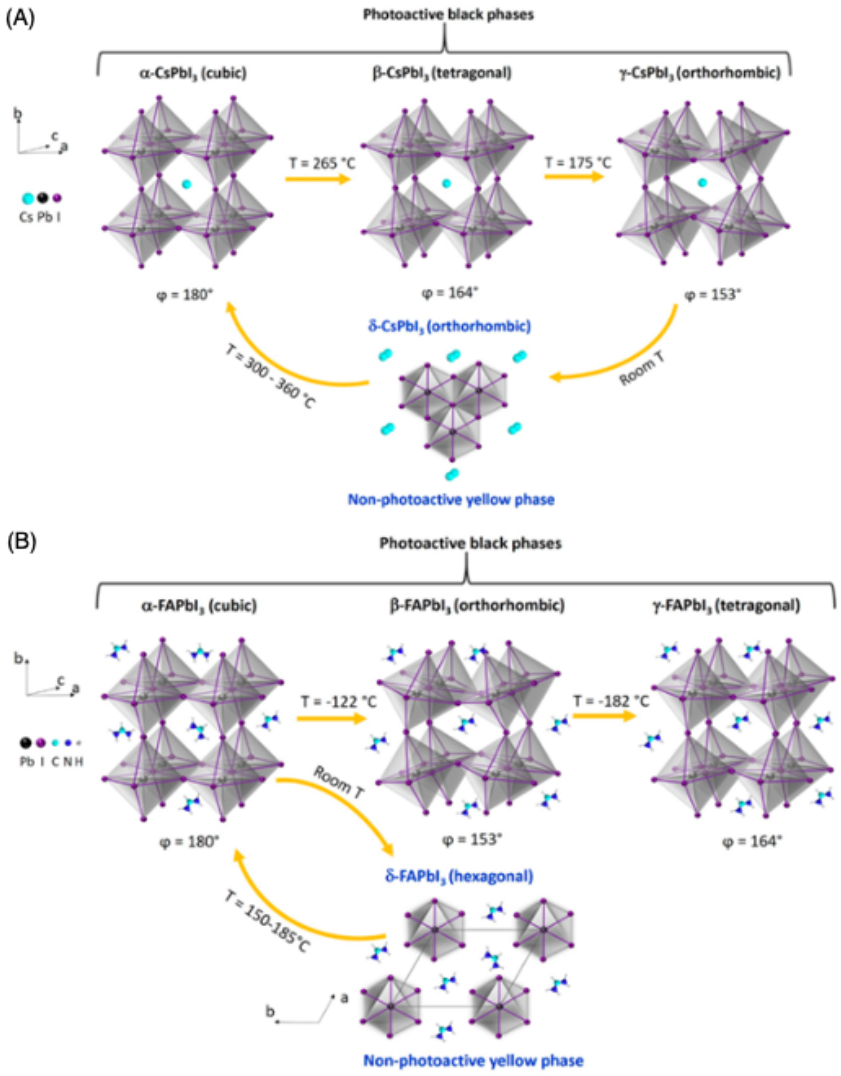

Figure 2.7: Illustration of the crystal structures of the reference (A) $CsPbI_3$ and (B) $FAPbI_3$ PVKs at different temperatures (ambient pressure conditions). In $Cs_xFA_{1-x}PbI_{3-x}Br_x$, a certain molar fraction of Cs^+ and Br^- ions substitutes FA^+ and I^- ions, respectively. The deformation of the BX_6 octahedra network expressed in terms of the B-X-B tilting angle (ϕ) as a consequence of the orthorombic and tetragonal phase transitions are shown. Further distorsions are caused by the mixtures of A-site cations and X-site anions, depending on the size of the ions (Goldschmidt tolerance factor) [44].

In conclusion, the organic and inorganic constituents are interdependent in PVKs. A substitution or deformation involving the organic cation A correspond instantaneously to an effect on the inorganic counterpart BX_6 (sublattice) and vice versa. The modifications and the interactions within each BX_6 octahedron, related to the octahedral factor, and between the different components of the PVK geometry, associated with the Goldschmidt tolerance factor, play a key role in determining the exceptional properties of this material. This soft dynamical behaviors of the crystal structure affect the electronic band structure and thus the optoelectronic properties of PVK [5].

2.2.2. Bandgap Tuning

PVK engineering allows to modify with high flexibility the composition of PVK and consequently alter its electronic band structure and bandgap. This not only opens up the possibility of improving the light absorption and other optoelectronic properties of PVK, but also of adapting them to the desired material functionalities and applications, from single-junction PSCs to both top and bottom cells in PVK-containing multi-junction solar cells.

As regards halide PVKs with ABX_3 crystal structure, the bandgap can be changed not only by replacing

the A, B and X constituents of PVK, but also deforming the PVK geometry and changing the temperature and pressure conditions [5]. As shown by Fig. 2.8, the bandgap can be extensively and easily tuned. In detail, it can be modified to energies between 1.03 and 3.54 eV, which correspond to the 350-1200 nm wavelength range [3].

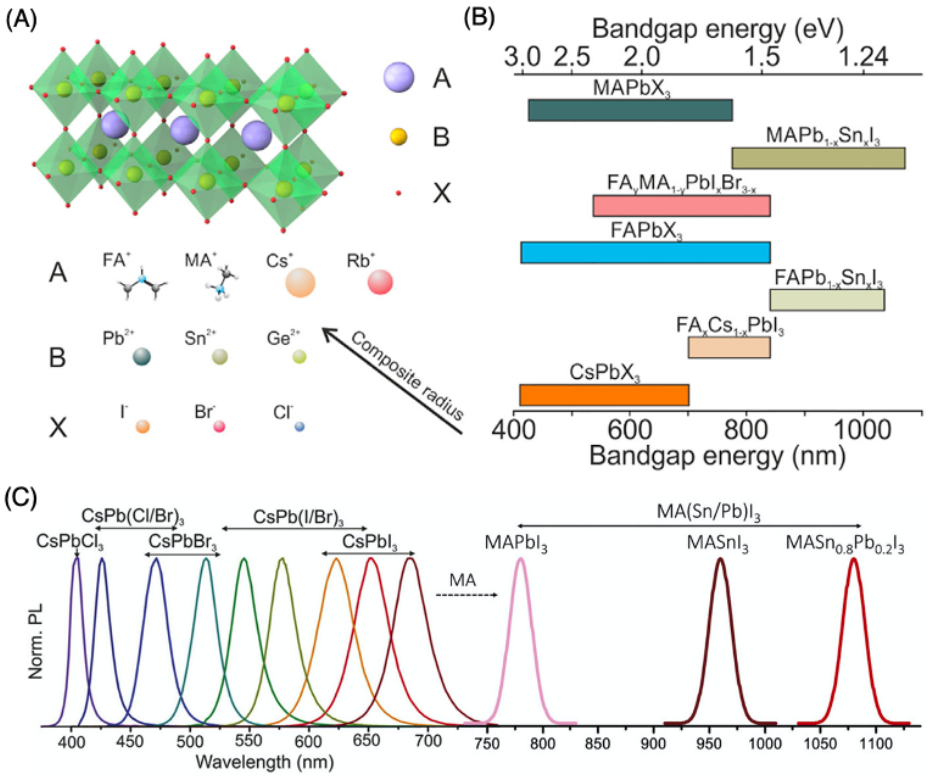

Figure 2.8: (A) Illustration of the halide PVK with ABX_3 crystal structure with its potential constituent elements and their location. (B) Bandgap energies of halide PVKs showing the possibility of bandgap tunability by modifying the combination of elements in the PVK structure [3]. (C) PL spectra of different halide PVKs [45].

The current research efforts are focused on PVK absorber layers based on mixtures of organic and inorganic cations and halogen anions in the A sites and X sites, respectively, of the ABX_3 crystal structure of PVK. These PVKs allow to fabricate PSCs with η >20% and a relatively high degree of reproducibility [3, 5]. This MSc Thesis Project focuses on a multications mixed-halides PVK of composition $Cs_xFA_{1-x}PbI_{3-x}Br_x$.

Cation A

A change in the A cation has minimal effect on the electronic band structure and the optoelectronic properties of PVK. In fact, as anticipated in Section 2.1.2, the top of the VB is formed by the B-s and X-p antibonding state and the bottom of the CB is mainly resulting from the B-p state. Hence, the electronic levels of the A cation lie deep within the VB and CB [5].

Nonetheless, the dimension of the cation A affects the Goldschmidt tolerance factor and therefore the bond distance between the metal cation in site B and the halide in site X and the spacing between the $[BX_6]^{4-}$ octahedra. Thus, the PVK electronic band structure and the bandgap are modified in turn. Both the size and the shape of the cation A have an influence on the bandgap.

A significantly small-sized cation A decreases the bandgap. However, when the organic cation is too small the PVK exhibits instability due to the $[BX_6]^{4-}$ octahedra tilting as mentioned in Section 2.2.1. This deformation affects the electronic properties and it causes a further reduction of the bandgap [5, 44].

Furthermore, it has to be taken into account that an organic cation, which has generally a larger size than an inorganic one, can induce a lattice dilatation, i.e. a larger lattice constant, which in turn can significantly increase the charge carriers effective masses, reduce the band edges curvature and increase the bandgap compared to an inorganic cation. This would affect both the light absorption and the charge carriers transport properties as described in Section 2.1.3 [5, 28].

In contrast with the previous observations, it is also true that when the ionic radius of cation A is sufficiently large, t→1 and thus a higher packing symmetry is obtained. Therefore, in this case an increasing ionic radius induces a reduction in the bandgap in an analogous way as small-sized cations. Consequently, the use of larger cations is convenient for improved light harvesting at longer wavelengths. However, excessively large A cations might generate low-dimensional PVKs, as briefly described in **??** [5].

To conclude, the optimization of the ionic radius of the A cation (r_A) must be taken into account [5].

The most widely researched 3D halide PVKs can contain in the A sites FA^+, MA^+, Cs^+ or less often Rb^+. The ionic size of Cs^+, MA^+ and FA^+ increases from 181, 270 to 279 pm, respectively [46]. As the A site cation gets bigger moving from inorganic to organic ions, the bandgap decreases from 1.67-1.73 eV ($CsPbI_3$), 1.52-1.57 eV ($MAPbI_3$) to 1.45-1.48 eV ($FAPbI_3$) (Fig. 2.9(A)) [5, 47]. Either only one of them or a mixture of them (mixed A-cation PVK) may characterise the PVK composition [3, 5].

To date, the organic cation MA^+ and the related $MAPbI_3$ are, respectively, the most widely studied A cation and hybrid organic-inorganic PVK for PV applications. However, to improve the power performance, stability and degradation issues of PSCs (see Section 2.4), new multications PVKs are also being investigated [3, 5]. This MSc Thesis Project focuses on a PVK of composition $Cs_xFA_{1-x}PbI_{3-x}Br_x$, where a mixture of FA^+ and Cs^+ is present in the A sites.

The size of the organic cation FA^+ creates a higher symmetry, lower bandgap and thus high-performance PSC, as the red-shifted optical absorption allows to absorb longer wavelengths of the solar spectrum, thus increasing the short circuit current density (J_{sc}) and reaching η >20% [5]. Furthermore, the asymmetric shape of the FA^+ molecular cation produces a distortion of the FA-X bonds which in turn causes FA^+ ions to be positioned slighty off-center in the octahedra of the PVK geometry. This further contributes to decrease the bandgap [5]. Lastly, PVKs containing FA^+ show structural stability of the cubic α phase at both RT and significantly high temperatures (T=423-458 K) [5, 44]. However, pure FA-based PVKs are particularly sensitive to moisture-induced degradation [5].

In order to overcome this and other problems, the inorganic cation Cs^+ is added to form a mixture of Cs^+ and FA^+ cations in the A sites of the PVK crystal structure.

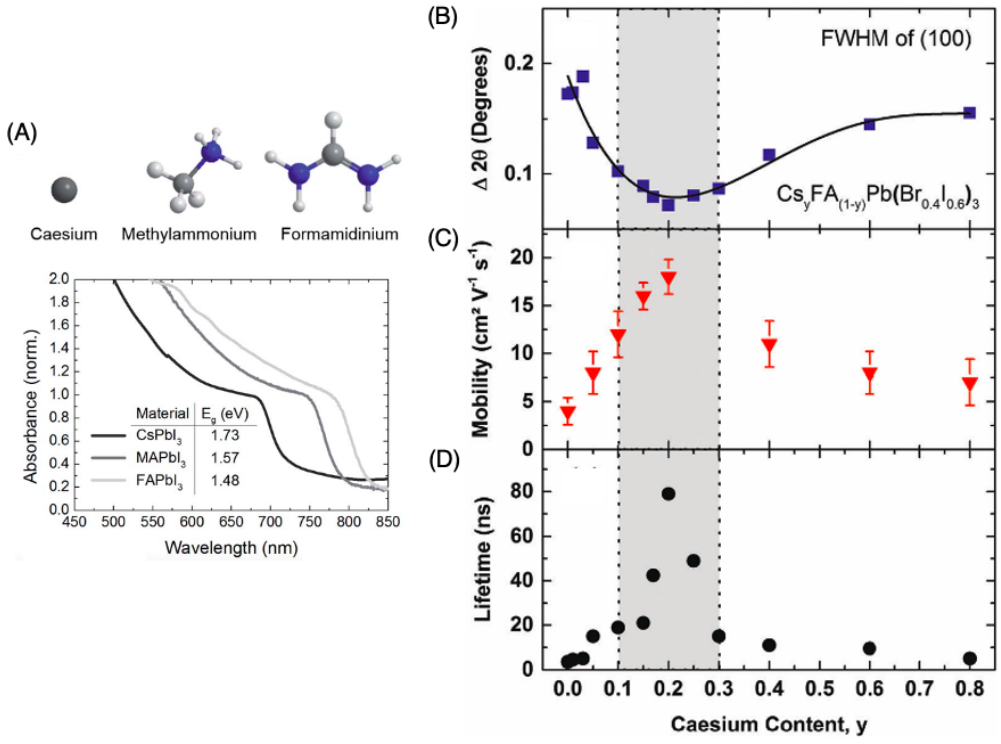

Figure 2.9: (A) Cs^+ atomic structure, MA^+ and FA^+ molecular structures as potential A-site cations in $APbI_3$, along with the absorbance spectra showing the bandgap variation associated with the correspondent A cations replacement in the ABX_3 crystal structure [47]. (B) Full width at half maximum (FWHM) of the (100) X-rays diffraction (XRD) peak, (C) effective charge-carrier mobilities and (D) charge-carrier lifetimes at 400 nm excitation wavelength of PVKs of composition $Cs_yFA_{1-y}Pb(Br_{0.4}I_{0.6})_3$ as a function of the Cs^+ content, which varies as 0.0<y>0.8. The grey band highlights the Cs^+ amount that results in the highest crystallinity and best stability of the related PVKs [35].

As indicated in Section 2.2.1, while FA^+ increases the Goldschmidt tolerance factor, Cs^+ decreases it. This allows to stabilise a pseudo-cubic α phase (Fig. 2.9(B)) and curbs the phase transition to the non-photoactive yellow δ phase that pure FA-based PVKs easily encounter at RT [35, 48]. Moreover, the incorporation of Cs^+ appears beneficial as it mitigates the moisture sensitivity of pure FA-based PVKs thanks to the stronger interaction between FA^+ and I^- as a consequence of reduction of the octahedral cage volume in the PVK geometry [49]. It also suppresses the halide segregation in mixed-halides PVKs containing both I^- and Br^- [19] and favours higher mobilitiey and longer charge carrier lifetime (Fig. 2.9(C) and (D)) by reducing the trap (defect) states density close to the VB and the charge recombination related to them [35, 49, 50]. As mentioned previously (see Section 2.2.1), PVK shows high-quality crystallinity and enhanced charge carrier mobilities and lifetimes when the Cs^+ content is between $0.1<x<0.3$ [35]. Finally, the addition of the small-sized Cs^+ increases the bandgap slightly [5].

For all the aforementioned reasons, Cs^+ generally seems to stabilise the PCE of the PSC and improve its resistance against degradation [5].

As a final remark, it is important to underline that the optoelectronic properties of multications PVKs can be taylored by changing the value of x according to the technological requirements [3].

Cation B

The cations in the B sites of PVK profoundly influence the bandgap, which can be modified much more effectively by their substitution than in the case of organic A cations replacement. Furthermore, as presented in Section 2.1.2, s and p orbitals of the cations in the B sites affect the VBM and the CBM states positions, respectively, and thereby the bandgap. To be more specific, the B-p orbitals primarily form the CBM [5]. The PVK of composition $Cs_xFA_{1-x}PbI_{3-x}Br_x$ analysed in this report presents only Pb^{2+} cations in the B sites.

Pb^{2+} is the most commonly used B cation thanks to its superior performance as well as stability. In spite of the Pb^{2+} advantages, the human health and environmental concerns related to lead-containing PSCs (see **??**) have prompted the research community to focus on replacing the cation B with non-toxic alternatives. Lead-free pure Sn-based PVKs and mixed isovalent metal PVKs obtained by alloying Pb^{2+} and Sn^{2+} cations in the B sites have been investigated [2, 5]. However, it should be considered that the lower the position of the metal cations B within Group 14 of the periodic table, the lower the electronegativity and the higher the bandgap [5]. In particular, the substitution of Pb^{2+} by Sn^{2+} causes a significant decrease in the bandgap, but also a detrimental reduction of the stability of PVK against oxidation. In fact, the tendency of Group 14 cations to oxidized to IV oxidation state upon exposure to air makes the octahedral framework unstable, consequently causing poor PV performance due to the substantial V_{oc} deficit (Fig. 2.10) [3, 5].

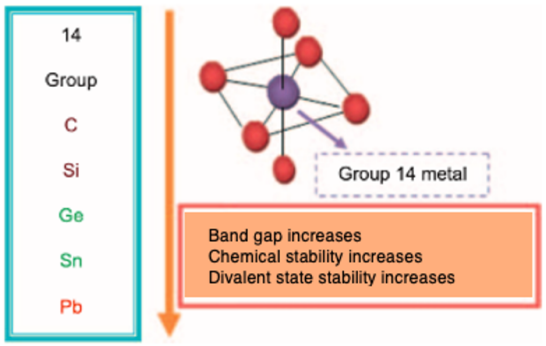

Figure 2.10: PVK bandgap tunability based on the replacement of Group 14 metal cations in B sites of the ABX_3 crystal structure [5].

Anion X

The substitution of halogen anions in the X sites of PVK can abundantly modify the bandgap, generating more pronounced shifts as compared to the replacement of organic cations in site A. The bandgap alteration is mainly related to the modification of the VBM, as the X-p orbitals are involved in its formation (see Section 2.1.2) [5]. [5]. The X-3p, X-4p or X-5p orbitals of the anions that contribute to the formation of the VBM change when Cl^-, Br^- or I^-, respectively, are substituted at the X sites. Moving from Cl^- to I^- along the Group 17 in the periodic table, the ionic radius increases, while the electronegativity and ionization potential (electron binding energy) decrease. When the electronegativity value of the halogen anion matches well with the

Pb^{2+} cation, the Pb-X bonding develops a more covalent character. Furthermore, the bandgap also becomes progressively smaller by replacing the Cl^-, Br^- and I^- anions at the X sites in this sequence, causing a redshift in the energy absorption [2, 5].

The bandgap can be tuned by alloying the halogen anions in the X sites and thus creating mixed-halides PVKs [3, 5], as in the case of the PVK with composition $Cs_xFA_{1-x}PbI_{3-x}Br_x$ under investigation.

The I^- anion is one of the most investigated for occupying the X sites in halide PVKs thanks to the possibility to obtain high-efficiency PSCs. It has a good match with the Pb^{2+} cation since they have an alike covalent structure. Thus, together they generally constitute a very stable system. However, I^- tends to get oxidized under certain perturbations, undermining the stability of the device [5].

When Br^- is incorporated in the PVK and mixes with I^- in the X sites, a compressive stress is generated on the existent Pb-I bonds. This creates a structural disorder which in turn alters the bandgap. Consequently, a progressive blue shift of the absorption band edge can be obtained by increasing the Br^- content (Fig. 2.11(A)) [5] and the appropriate variation of the I:Br ratio allows to tune the bandgap of PVK. Moreover, Br^- has been used to obtain good thermal stability in PSCs, since I^- and Br^- have comparable ionic sizes (220 pm and 196 pm, respectively [51]) [5]. However, this small difference in the ionic radii, especially for high Br^- content, causes the cubic α phase of Cs^+/FA^+ lead mixed-halides PVKs to be less thermodynamically favourable, the charge carrier recombination to be larger due to an increase in trap states density and the charge carrier mobility to be lower as a consequence of extrinsic disorder or intrinsic electron-phonon interactions [35]. In addition, the crystal disorder can lead to photo-induced halide segregation in mixed-halides PVKs. The mechanism at the basis of the segregation of the X anions in the form of I-rich and Br-rich domains upon exposure to light are still not fully clear, but it seems that GBs, defects and amorphous regions favours the phenomenon. Nevertheless, it has been found that the ion migration spontaneously reverse in few minutes after removing the illumination and that high-quality crystalline PVK is more stable against it [35]. For this reason, as explained in Section 2.2.2, the Cs^+ content should be kept between $0.1<x<0.3$, so that the crystal structure can be stabilised against both structural changes and photo-induced halide segregation. This allows to obtain excellent crystallinity and charge carriers dynamics and transport properties in PVK while largely tuning the I:Br ratio (Fig. 2.11(B)) [35].

In conclusion, it is possible to produce PSCs based on mixed-halides PVKs with high conversion efficiency and stability [5].

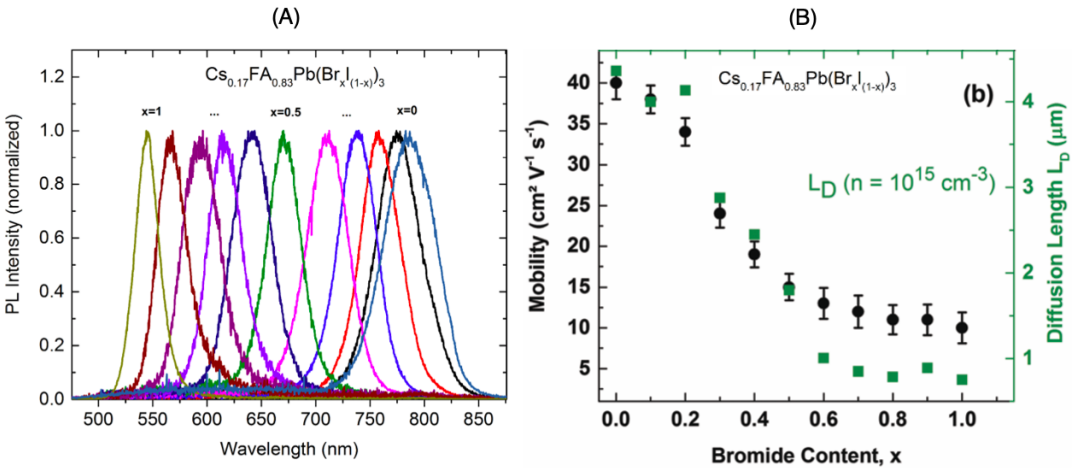

Figure 2.11: (A) PL spectra of PVK thin-films of composition $Cs_{0.17}FA_{0.83}Pb(Br_xI_{1-x})_3$ normalized to the peak emission, indirectly showing the effect of the variation of the anion X in the ABX_3 crystal structure, looking at how the Br^- content affect the direct bandgap of PVK. (B) Effective charge carrier mobilities (black dots, with error bars) and charge carrier diffusion length (green squares) of PVK of composition $Cs_{0.17}FA_{0.83}Pb(Br_xI_{1-x})_3$ as a function of the Br^- content [35].

2.3. Perovskite Solar Cell Architecture

Several different PSC architectures have been implemented over time. A thoughtful selection of the architecture type and materials is crucial in order to optimise the trade-off between efficiency, stability and costs and thus fabricate successful and commercially attractive PSCs [5]. The materials for the different layers should be selected and designed to facilitate the extraction of the charge carriers and their transport to the electrical

contacts and show a low recombination rate, so that electrons can be successfully collected and flow through an external circuit, which thereby supplies electrical energy. Electronic properties (band-edge alignment between each layer and the neighbouring ones, exciton binding energy, charge carrier diffusion length and lifetime, etc.), optical properties (absorbance, reflectance, transmittance, etc.), physical properties (surface coverage of films, density of pinholes and other surface defects, etc.) and materials matching at the interfaces have to be taken into account. Finally, the long-term stability of PSCs can be ameliorated by designing particular architectures involving moisture passivation, hydrophobic, self-cleaning, etc. layers [5].

2.3.1. Single-junction Solar Cell

The simplest way to exploit the potential of PVK absorber layers is by applying them in single-junction PSCs. In a single-junction PSC it is generally possible to identify certain typical layers with specific functionalities in each architecture type, i.e. the PVK absorber (photoactive) layer, the Electron Transport Layer (ETL), the Hole Transport Layer (HTL), the electrodes (anode and cathode), i.e. a metal electrical contact and a Transparent Conductive Oxide (TCO) layer as the other electrical contact, and finally the solar cell substrate. In addition, other extra interconnecting functional layers can also be found as architecture components. The whole system is usually incapsulated to protect it from the external agents [5].

Moreover, considering the typical thin-film nature of PSCs, a PSC can be fabricated in either superstrate or substrate configurations. In the first (conventional) case, the light enters the cells through the substrate, which thus must be made of transparent materials. Conversely, in the second case the light strikes the cell from the opposite side of the substrate, i.e. the film side (not shown in this MSc Thesis report). The substrate can be thereby realised using a broader range of materials. In the substrate configuration the deposition sequence of each layer and related interfaces have to be inverted with respect to the superstrate one [52].

This MSc Thesis Project has been developed with a view to the long-term fabrication of an inverted planar p-i-n glass/ITO/MoO_x/PVK/C_{60}/Ag PSC architecture in the superstrate configuration.

Inverted Planar p-i-n Solar Cell

The inverted planar architecture consists of a heterojunction with an p-i-n structure. This means that the inverted planar solar cell architecture is comprised of a TCO anode, a p-type HTL, an intrinsic PVK layer, an n-type ETL and a thin metal layer as cathode (Fig. 2.12) [5].

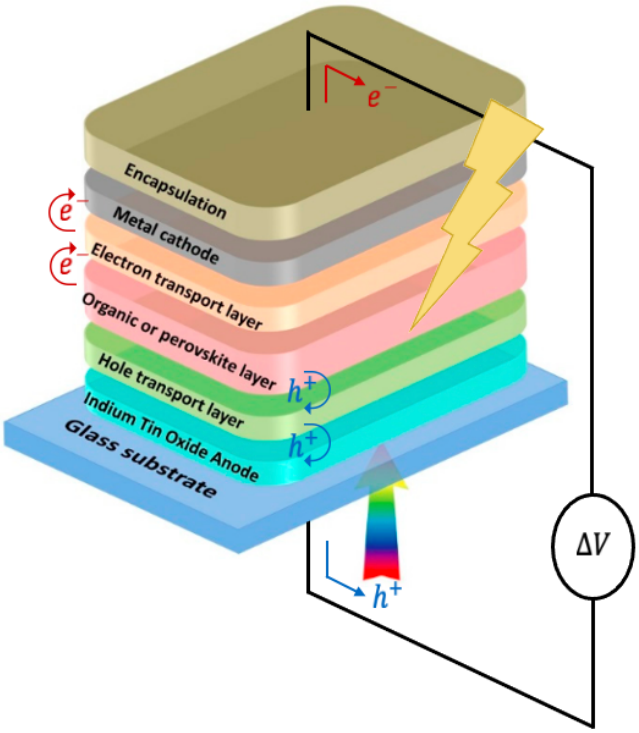

Figure 2.12: Schematic representation of an inverted planar (p-i-n) PSC architecture with its main constituents in superstrate configuration and the path of the photogenerated charge carriers and relative photocurrent typical of this type of PSC. Adapted from [53, 54].

This solar cell architecture has been defined as "inverted" given that it shows an opposite stacking sequence in the deposition of the different layers with respect to the regular planar configuration, which is characterised by a n-i-p structure. On the other hand, the term "planar" derives from the presence of a thick and dense PVK absorber layer. The PVK absorber layer can be deposited over the HTL by different synthesis techniques, i.e. solution-based, vapour-based or hybrid [5].

Among the wide variety of materials and morphologies that can be used, the single-junction PSC of this MSc Thesis Project presents a substrate made of glass and TCO of Indium Tin Oxide (ITO). The TCO must be highly transparent to reduce the parasitic absorption, given that is the first layer through which light first passes before reaching the PVK absorber, and conductive to allow the lateral transport of the current across the top of the PSC [55]. Furthermore, considering the conventional situation where the light illuminates the solar cell from the substrate side (superstrate configuration), the TCO itself can fulfil both the substrate and anti-reflection surface functions [5].

As previously described, in p-i-n inverted planar devices the PVK is deposited directly on the HTL. Hence, the HTL chemico-physical features are very important, as they affect the growth and in turn the properties of the PVK absorber layer. Consequently, the V_{oc} and thereby the performance of the PSC vary too. The HTL can be made of either organic or inorganic materials [5] and it can be processed without any dopants when the PSC is in the p-i-n configuration [102]. HTLs made of inorganic materials have been investigated to overcome the issues of high costs and poor stability associated with organic materials, especially after exposure to moisture [5, 57]. In this MSc Thesis Project, molybdenum oxide (MoO_x) has been selected as HTL material to be deposited by thermal evaporation.

On the other side, in case of an inverted planar p-i-n architecture the ETL should present properties such as transparency, wide bandgap, suitable band-edge alignment with PVK and the TCO and resistance against degradation, as well as the ability to hinder the hysteresis behaviour of the PSC as much as possible (see Section 2.4) [56]. As the HTL, the ETL can be either organic or inorganic derivation too. In this MSc Thesis Project, the PSC presents an ETL made of an organic material, namely fullerene (C_{60}), which satisfies the aforementioned requirements and offers the advantage to be deposited at low temperature via thermal evaporation, thus allowing the implementation of innovative PV devices such as fully thermally evaporated multi-junction devices [5].

Lastly, silver (Ag) has been chosen as metal electrical contact of the PSC developed in this MSc Thesis Project.

The inverted planar p-i-n PSCs are characterised by easy and low-temperature fabrication, thin HTL and ETL that reduce parasitic absorption leading to higher photogeneration current density (J_{ph}) and good compatibility with flexible substrates. Thus, they are particularly promising for multi-junction solar cells application (see Section 2.3.2) [63–65, 102]. Additionally, they show low or negligible current-voltage (J-V) hysteresis in comparison to regular planar n-i-p solar cells [63, 64], a phenomenon that negatively affects the determination of the PCE and stability of the PSC.

However, the best-performing p-i-n PSCs typically present lower PCE than those of the highest-efficiency devices with an n-i-p architecture (>22% and >25%, respectively) [66]. This is mainly due to lower open-circuit voltages, as inverted planar PSCs usually show V_{oc}<1.1 V with respect to the planar PSCs characterised by V_{oc}>1.2 V. The voltage drop might be caused by non-radiative recombination both inside the PVK layer and at the interfacial contacts [64], as well as by the presence of a barrier for holes extraction at the p-contact [67]. Nevertheless, the progress in the fields of PVK synthesis techniques and interface engineering has lead to a reduction of the V_{oc} loss [63].

The inverted p-i-n planar solar cells have shown continuous improvements over the years, in terms of both efficiency (photon-to-electron conversion rate) and stability (hysteresis and device degradation after exposure to certain environmental factors). This is making them tremendously attractive for future commercialisation [5].

Acknowledging the particular materials and functions of the components of a PSC architecture is particularly useful to understand the characteristics and advantages of the inverted planar p-i-n PSC made of glass/ITO/MoO_x/PVK/C_{60}/Ag on which this MSc Thesis Project focuses, in the perspective of applying it in a multi-junction solar cell, more precisely a 2-T PVK/Si tandem.

2.3.2. Multi-junction Solar Cell

Multi-junction solar cells consist in a stack of two or more solar cells (subcells). Each junction converts a specific portion of the solar spectrum into electricity, thanks to the presence of at least two absorber layers

of different bandgaps, which can be made of either the same or different types of photoactive materials. They have been developed in order to further optimise the energy utilization of the solar spectrum and to go beyond the PCE SQ limit of a single-junction solar cell (see Section 1.2.2) [2, 3].

Considering a double-junction (also known as tandem) solar cell, which is the long-term goal related to this MSc thesis project, the top cell absorbs the shorter wavelengths (blue light) and thus it uses more energetic photons for the charge carries generation, whilst the bottom cell has an absorption onset corresponding to longer wavelengths (red light), converting the less energetic photons into electricity, as can be observed from Fig. 2.13. Consequently, photocurrent and potential losses that take typically place in single-junction solar cells when the photon energy (E_{ph}) is $E_{ph}<E_g$ and $E_{ph}>E_g$, respectively, are minimised [3]. As a result, the final potentially obtainable PCE of the entire multi-junction solar cell is higher compared to the individual cells of which it is composed [2].

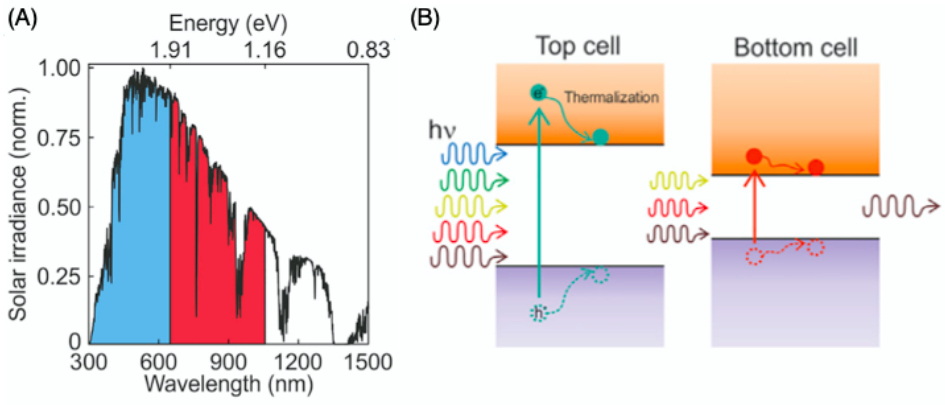

Figure 2.13: (A) Ideal spectral response of a tandem solar cell in reference to the AM1.5 solar spectrum irradiance, where the top cell (blue) harvests the high energy photons with short wavelengths and the bottom cell (red) the low energy ones with longer wavelengths. (B) Energy-band diagram for a tandem solar cell showing the absorption of photons with higher energies in the top cell along with the potential thermalisation losses and the absorption of photons with lower energies that penetrate deeper into the device in the bottom cell, which are thus harvested to avoid photocurrent losses [3].

it is important to specify that, similarly to the single-junction solar cells, a PCE SQ limit can also be determined for any multi-junction solar cells. Several aspects related to the optical and electric design of these devices have to be taken into account to approach their own PCE SQ limit and optimise their stability [3].

First of all, the selection of the photoactive materials of the different subcells is of paramount importance. The choice of the optimal bandgap combination, composition and thickness of the absorber layers of the subcells is fundamental, so that both the front and rear cells present optimum absorption properties to work simultaneously [3].

Then, all the multi-junction solar cell materials and components should be selected and designed to accomplish good charge carriers transport properties, low resistance (high conductivity), appropriate energy band alignment between the different layers in the architecture, minimum parasitic absorption that occurs at the substrate, ETL, HTL, contacts and other layers and minimum reflection losses in the wavelength range λ=350-1200 nm [3]. With regards to a PSC, the most commonly used materials have been already presented in Section 2.3.1. In addition to this, each layer thickness in the PSC architecture needs to be optimised to maximise both the photocurrent of the PSC and the photocurrent matching between the subcells. Lastly, the shape, texture and surface characteristics of the layers in the multi-junction device architecture play a fundamental role [3].

Furthermore, it is important to appropriately apply light management strategies in to reduce reflection losses and enhance light trapping. A transparent Anti-Reflection Coating (ARC) is usually deposited on top of the front TCO to reduce the reflection losses. However, these layers lead to the loss of a fraction of the light that would have been absorbed, since when the photons pass through the front cell, they do not have a second chance to be absorbed as would have happened if a metal contact would have been used [3]. Moreover, a non-flat random-pyramid texture at the rear side of the multi-junction solar cell can be created to favour the internal reflection and hamper the absorption of light in the metal back reflector, thereby reducing the losses [55, 68–70]. On top of that, photonic crystals, metamaterials, surface textures, light scatterers and or metallic nanostructures exhibiting plasmonic resonances can be implemented to improve the light management of the multi-junction device [3].

It has also to be taken into account that some of the commonly employed fabrication techniques and thermal annealing treatments for the deposition of the transparent contacts and the ETL layer (in case of an inverted planar p-i-n configuration, described in Section 2.3.1 as potential PSC architecture in this MSc thesis project) might damage the absorber or the other layers in the multi-junction solar cell architecture [3, 55]. To prevent negative effects, a protective buffer layer can be pre-deposited [3, 71]. The buffer layer is designed to be very thin, so that it has just a small optical and electrical influence on the solar cell [3].

In addition to all the previous observations, the whole multi-junction solar cell configuration is another aspect of paramount importance. They can present different configurations on the basis of how the subcells are mechanically stacked and the electric connection between their electrodes. It is mainly possible to distinguish between two-terminal or monolithic (2-T) and four-terminal (4-T) multi-junction solar cells [3]. Besides, three-terminal (3-T) multi-junction devices can also be fabricated [69], but given that they are less common they will not be discussed in this MSc thesis report.

In the 2-T monolithic multi-junction solar cell case (Fig. 2.14(A)), the subcells are connected in series forming a monolithic stack, thus they are electrically and mechanically coupled. Hence, the current densities through the different subcells must be the same (current-matching condition) and it is thereby limited by the subcell that produces the lowest photocurrent. Finally, a tunnel junction acting as recombination layer is required between them to achieve charge neutrality, i.e. to make the non-collected electrons coming from the PVK front cell and holes arising from the c-Si-based rear cell recombine. This layer can be made of different materials, e.g. ITO [72], indium zinc oxide (IZO) [9] and nanocrystalline silicon (nc-Si:H) [70]. Regarding the optical and electrical properties, a recombination layer must be transparent for the photon wavelengths which have to reach the rear cells and be characterised by high conductivity. It has in fact to fulfill the function of make charge carriers diffuse in the direction perpendicular to the stacking of layers along with favouring their recombination [3].

On the other hand, a 4-T multi-junction solar cell is composed of two or more independently working subcells, which can be externally connected either in series or in parallel. It is possible to define two different 4-T configurations. In the first case, the subcells are electrically decoupled and mechanically stacked (Fig. 2.14(B)). Transparent contacts and an insulating layers are required in between each subcell and the other, as well as two electrodes for each subcell. In the second case, the subcells are instead electrically and mechanically decoupled but optically coupled. They involve the use of an optical filter, which consists in a dichroic mirror. This is able to split the incident solar radiation by reflecting the photons with short wavelengths and transmitting the ones with long wavelengths (Fig. 2.14(C)) [3].

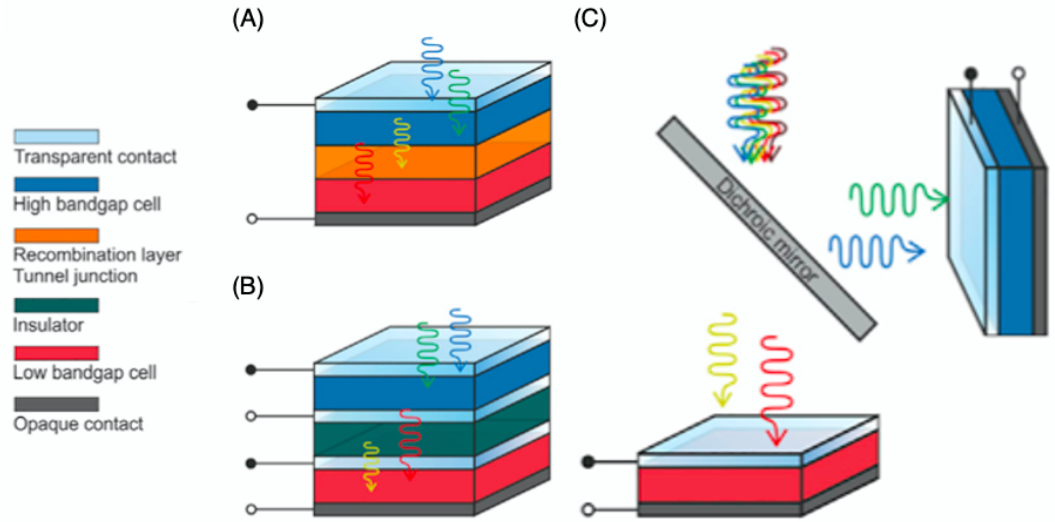

Figure 2.14: Schematics of the three different configurations for a double-junction tandem cell: (A) Electrically and mechanically coupled two-terminal (2-T), (B) electrically decoupled and mechanically coupled four-terminal (4-T) and (C) electrically and mechanically decoupled but optically coupled four-terminal (4-T) [3].

As mentioned above, this MSc thesis report examines 2-T monolithic tandem solar cells in more detail, envisioning a future application of PSCs in this type of devices. In comparison to the other configurations, 2-T multi-junction solar cells present lower parasitic absorption. However, they must fulfil the current-matching condition, which poses more constraints on the choice of the subcells materials considering their bandgaps.

Moreover, 2-T multi-junction solar cells also show the disadvantage of not being able to harvest the energy emitted in the form of photons as a result of radiative recombination between electrons and holes in the intermediate recombination layer between the subcells. Additionally, the fabrication techniques of the different junctions need to be compatible to avoid the damage to the cell layers as a result of certain deposition methods. In spite of that, 2-T monolithic multi-junction solar cells are more attractive for up-scaling the manufacturing process to an industrial level, as they generally show better PV performance than 4-T devices and result cheaper due to the smaller amount of transparent conductive layers and electrodes required in the complete device [3].

PVK/Si Tandem Solar Cells

Among the different PV technologies, the PSCs implementation in PVK/Si tandem solar cells, where the PVK subcell works as top cell and the c-Si-based one as bottom cell, looks particularly promising. c-Si-based solar cells constitute an extensively researched and acknowledged PV technology, which dominates the PV market. High-performance c-Si-based solar cells, more precisely presenting the interdigitated back contact (IBC) configuration, can reach J_{sc}>42 mA/cm^2 [73] and a record lab efficiency of η=26.7% [7, 8], close to the single-junction c-Si solar cells intrinsic SQ limit set at η=29.4% [10] considering the non-radiative intrisic losses. It is noteworthy that the record lab PSC with efficiency η=25.5% is progressively approaching the value of η=26.7% of the best-performing c-Si-based solar cell.

The theorethical SQ limit of a PVK/Si tandem solar cell is η=44.1%, reduced to η=35.7% when taking into account the intrinsic non-radiative losses [74]. However, several issues such as their life cycle and manufacturing costs related to components, architecture and fabrication techniques need to be addresses before they can enter the PV market in their own right [2, 3].

The optimal bandgap for the PVK top cell of a 2-T PVK/Si tandem solar cell is around E_g~1.65-1.73 eV in order to be perfectly coupled with the absorption of a c-Si bottom cell, whose bandgap is E_g=1.12 eV [74–76]. Some multications mixed-halides PVKs of specific composition present a bandgap close to the required value, as shown in Fig. 2.15(A) [3].

However, when the a PSC presents E_g>1.65, its V_{oc} is generally below the 90% of the respective SQ limit for its particular bandgap and its efficiency remains below η <20%. The highest efficiencies (η >22%) of the PSC are instead reached for lower values of the bandgap (E_g~1.5 eV and below) (Fig. 2.15(B)). This means that the the V_{oc}-to-bandgap losses due to non-radiative recombination are high in the PVK top cell characterised by an optimal bandgap for a 2-T PVK/Si tandem solar cell. This is undoubtedly a problem of primary importance for these tandem devices and will require further research in terms of PVK compositional and bandgap engineering [76].

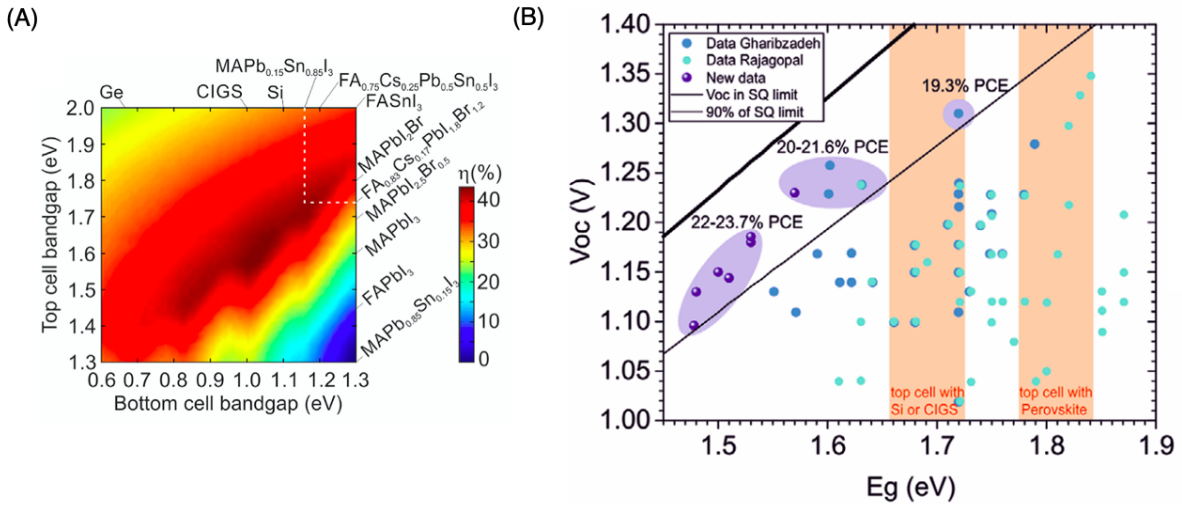

Figure 2.15: (A) Expected efficiency for ideal PVK tandem devices as a function of the bandgaps of the photoactive materials that may be used in both the top and bottom cells. Some of the most commonly studied absorber materials for PV applications are shown. An an example, the white dashed lines indicate that an efficiency close to the optimum η=44.1% can be reached by coupling a $FA_{0.83}Cs_{0.17}PbI_{1.8}Br_{1.2}$ PVK as top cell and a $MAPb_{0.15}Sn_{0.85}I_3$ PVK as bottom cell in a all-PVK tandem device [3]. (B) V_{oc} as a function of E_g, where the purple areas highlight the region of optimum PCE and the orange bands indicate the optimal bandgaps for a PVK top cell with different PV technologies as bottom cell, considering c-Si-based solar cells. The data are retrieved from different papers [76].

Particularly in relation to tandem solar cells comprising a PSC, another critical aspect is that usually characterised by a flat front side. In fact, the PVK top cell is typically fully planar because it is routinely deposited on the flat front side of the bottom cell. This polished and flat surface facilitates the deposition of one cell on top of the other, as PVK top cells are often deposited by solution-based synthesis techniques which are not allowing conformal growth on the sub-μm random-pyramid texturing that may be present at the front side of the bottom cell (e.g. in case of a c-Si-based bottom cell) [69, 70, 77]. Nevertheless, some synthesis techniques allow to deposit the PVK top cell on a double-side-textured bottom cell to fabricate a fully textured 2-T PVK/Si tandem solar cells [70].

PVK/Si tandem solar cells showing the highest PCE whose compositions are known are typically showing a p-i-n inverted planar PSC top cell, presenting multications mixed-halides PVKs as absorber layer material, and a a-Si:H/c-Si Silicon Heterojunction (SHJ) bottom cell, namely the best-performing c-Si-based technology [3, 79]. Moreover, the best-performing 2-T PVK/Si tandems typically show a texture based on randomly distributed pyramids at the rear side of the Si-based bottom cell, which, as previously mentioned, can be created to decrease the reflection losses and increase the optical path length of light in the cell, i.e. improving the light trapping [3, 55, 68, 70, 72]. Double-side-textured c-Si-based bottom cell can also be integrated to fabricate fully textured 2-T PVK/Si tandem solar cells. In order to enable a conformal growth of the PVK absorber and the other different layers of the tandem device architecture on the microsized pyramids of the double-side-textured c-Si-based bottom cell, alternative techniques as thermal evaporation, atomic layer deposition (ALD) and sputtering are required [70]. However, these fully textured 2-T PVK/Si tandem solar cells are still under research. To date, the best-performing PVK/Si tandem device has a 2-T monolithic configuration and it shows η=29.80%. Unfortunately, its precise composition and architecture structure have not been published yet [7, 11]. Therefore, even though the PV performance of these devices should be further improved to approach the SQ limit, an important breakthrough is that 2-T monolithic PVK/Si tandem solar cells have recently broken the record for single junction c-Si-based solar cells (η=29.80% versus η=26.7%) [7, 11, 74].

In conclusion, the field of multi-junction solar cells involving PSCs is still at an early stage and therefore offers great opportunities for future development. Further research is needed to fully compete with the PV performance of the well-established c-Si and other Si-based PV technologies.

2.4. Challenges and Potential Solutions

PSCs present several excellent properties, but their commercialisation is hindered by poor stability and short-life time. Degradation phenomena, J-V characteristic hysteresis and material toxicity as a consequence of Pb^{2+} incorporation are the main issues that need to be addressed in the near future to enable PVK solar cells to enter the PV market [5]. Notwithstanding the strict interconnection between these challenging problems [5], the herein Section 2.4 focuses specific attention on the problem of the degradation of PSCs.

2.4.1. Degradation

Degradation is a major problem in PSCs. It can start to take place in the form of decomposition of the PVK photoactive layer. It is known that PVK absorber material is extremely sensitive to water (H_2O) molecules. Actually, water is not the only triggering factor, as also oxygen (O_2) and UV radiation are necessary to initiate the degradation process. [5, 80–82]. These three factors can act in synergy at RT and without any mechanical stress or strain acting on the solar cell [80]. Thus, they will be described in more depth in this Section 2.4.1, along with thermal degradation [50, 83]. Furthermore, mechanical stresses and strains can take part in accelerating the degradation process. As a consequence, the chemical, physical and optoelectronic properties of the PVK and the other layers in the solar cell architecture deteriorate rapidly [5]. Moreover, degradation can initiate in other layers in the PSC architecture [5]. Another factor reducing the PSCs stability is the ions migration through the PVK crystal structure and the other layers of the solar cells. For instance, this phenomenon is at the origin of PSCs self-degradation [84]. All these factors, that often act in combination with each other, reduce the PV performance and the stability of the PVK solar cell as well as its lifetime [5]. This field of research is still intensively investigated by the scientific community, as the exact role of the different environmental and non-environmental factors and the reactions leading to degradation and are not fully clear. Hence, several hypothetical degradation mechanisms have been proposed [5].

Finally, it is worth mentioning that the instability of the PSC is not only related to the PVK layer, but also to the ETL, the HTL, the electrodes and, if present, also the other intermediate layer. This expresses the interrelated nature of degradation phenomena resulting in reduced environmental stability of the PSCs [5, 85].

Moisture (H_2O and O_2)

Moisture, i.e. water molecules present in the air, is the most aggressive agent causing degradation of PVK and in turn of the whole PSC due to the strong interaction of PVK with H_2O and O_2 molecules. The decomposition is initiated and even accelerated when the PSC is exposed to light [5].

One of the possible degradation pathways is based on the idea that in a moist environment PVK interacts with the water molecules present in the moisture and it is involved into an hydrolysis reaction that leads to its decomposition. It has been suggested that a simple acid-base reaction takes place, where a single water molecule, which acts as Lewis base, mingles with PVK. Then, the extraction of a proton triggers a series of reactions leading PVK to decompose into an aqueous solution [80, 86]. Solid PbI_2 is also formed in the presence of H_2O [80, 86]. This is proven by the visible alteration of the PVK color from dark brown to yellow due to the decomposition into PbI_2 [5]. Then, the decomposition of PVK goes further and HI is also formed in the aqueous solution [80, 86]. Furthermore, HI can follow a redox reaction with O_2 in the moist air, which leads to the formation of solid I_2 and water. The PVK decomposition mechanism can be observed in Eq. (16):

$$4HI(aq) + O_2(g) \leftrightarrow 2I_2(s) + 2H_2O(l) \tag{16}$$

According to Le Chatelier's principle, this reaction associated with the consumption of HI easily drive the whole degradation process forward, so it is extremely important [80, 86].

To conclude, an individual water molecule is sufficient to trigger PVK degradation, but an excess of water is needed to dissolve the HI and the PVK decomposition products [80]. As a consequence of the detrimental effect of moisture on PVK, the change of composition and colour is accompanied by a considerable drop in the absorption and a new absorption onset at E_{ph}~2.3 eV corresponding to the bandgap of PbI_2, providing evidence for PVK decomposition [18].

Finally, the moisture-induced decomposition of the PVK absorber often triggers simultaneous degradation of the other layers of the PSC. Gaseous and non-gaseous decomposition products can diffuse into the other layers and, in combination with the migration of mobile species, induce their degradation. Moreover, the gaseous products create voids in the PVK, which may lead to its detachment from the adjacent ETL and HTL [5, 85, 87].

Light

Light, in particular in the UV wavelength range of $\lambda \sim$ 100-400 nm, is another preeminent cause of instability in PSCs.

With regards to moisture- and oxygen-induced degradation, as explained earlier, the decomposition of PVK after contact with water molecules leads also to the formation of HI as one of the reaction products. A second route for HI degradation involves UV radiation. This causes a photochemical reaction in which HI decomposes into H_2 and I_2 (Eq. (17)):

$$2HI(aq) \overset{h\nu}{\longleftrightarrow} H_2(g) + I_2(s) \tag{17}$$

As already stated before, this is another relevant reaction as it involves consumption of HI and it can thus easily move the whole degradation process forward [80, 86]. This explains, as already stated, why the decomposition of PVK due to moisture is even faster when exposed to light than in the dark [5].

Furthermore, by exposing the PVK solar cell to light and dry air without any encapsulation, the electrons generated in the PVK layer can react with O_2, creating photogenerated reactive superoxide ions (O^{2-}). This oxygen species remove protons from the organic molecules in the A sites of the PVK, i.e. FA^+ in the case of the PVK on which this MSc Thesis Project focuses, initiating then its decomposition. As a result, PVK rapidly degrades in minutes to few hours due to the combined action of light and oxygen [88].

Additionally, Br-containing mixed-halides PVKs characterised by a Br^- content >30% typically show light-induced halide phase segregation (I-rich and Br-rich domains) and even photochemical degradation resulting in the formation of non-photoactive δ-$FAPbI_3$ phase, PbI_2 and metallic Pb^0 are as decomposition products. As mentioned before, I_2 is developed too [82].

On top of that, UV illumination can affect in a negative way also other layers of the PSC [5].

Lastly, it is important to underline that the direct exposure to the sunlight determines also an increase in temperature of the PSC under operative conditions, which reduces the PCE and stability of the device [5].

Temperature

The processing, annealing and operative temperatures are strongly affecting the PSC stability, as thermal degradation may occur. It is noteworthy that thermal degradation may lead to the decomposition not only of PVK, but also of the ETL/HTL. Moreover, it can take place in an inert atmosphere, e.g. in an argon (Ar) or nitrogen gas (N_2) environment, so it does not necessarily need the presence of moisture or oxygen [5].

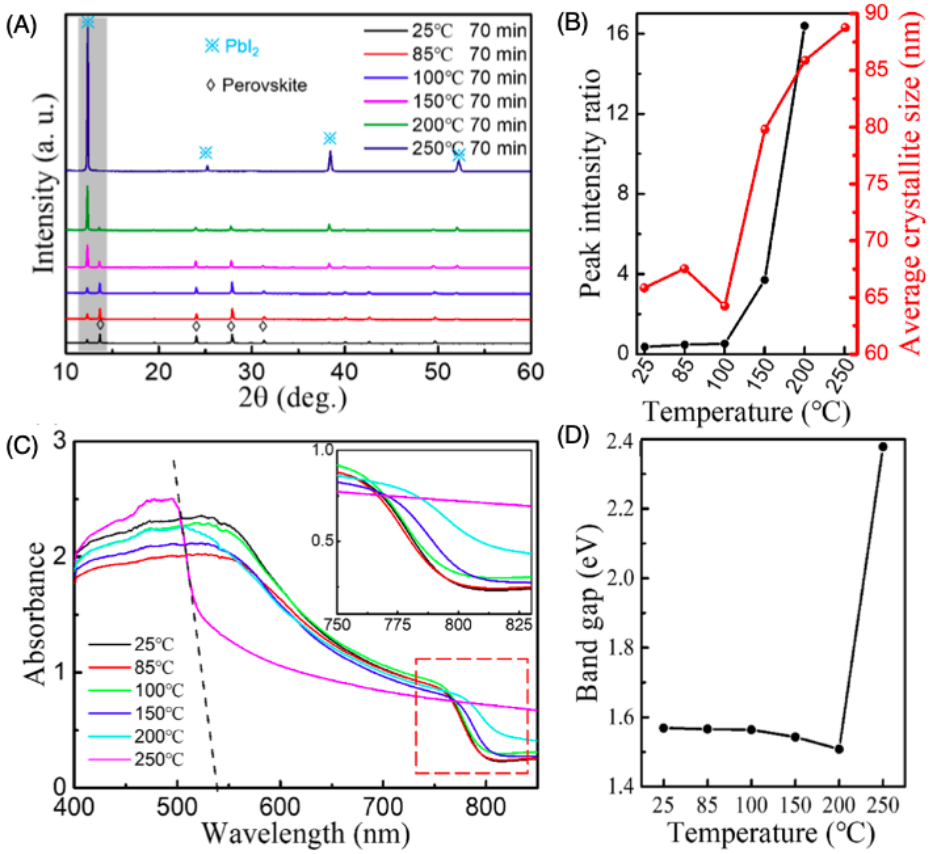

Figure 2.16: Effect of increasing annealing temperature on multications mixed-halides PVK thin-films. (A) XRD diffractograms, showing the increase in the main PbI_2 peak intensity as the annealing temperature increases. (B) PbI_2 (001)/PVK (110) peak intensity ratio and average crystallite size as a function of temperature. (C) UV–Vis absorption spectra, showing the red-shift of the absorption onset for increasing temperatures. (D) Variation of the bandgap as a function of temperature [83].

During both the PVK and PSC fabrication process it is important to pay attention to the fact that certain deposition techniques and thermal treatments associated with PVK or other specific layers of the PSC requires elevated temperatures that can degrade some pre-deposited materials sensitive to heat, including the PVK itself. In addition, thermal treatments may also affect the interface between the PVK and the ETL/HTL [5].

In addition to this, thermal degradation can occur after inappropriate thermal treatments on the PVK crystal structure. Annealing is typically performed to make the precursors fully react with each other to form PVK and increase the crystallinity and grain size of the system [5]. However, during the annealing the volatilization of gaseous FAI and the consequent formation of solid PbI_2 (Fig. 2.16(A)) take place too. Nonetheless, controlled heat treatments may lead to the formation of an small excess of PbI_2, more precisely a 5% excess [89], to passivate GBs and reduce the charge carriers recombination [83]. On top of that, defect density increases, facilitating charge carriers recombination [83].

The annealing also affects the morphology, microstructure (Fig. 2.16(B)) and optoelectronic properties of PVK and in turn the PSC performance. Hence, it is important to determine the most suitable annealing parameters, in light of the fact that excessively high annealing temperatures (typically when T>150 °C [83]) or too long annealing times may lead to detrimental alterations of the PVK structure and even the complete decomposition into PbI_2. More precisely, as the annealing temperature increases continuously above T=150 °C, the absorption edge moves towards longer wavelengths (Fig. 2.16(C)), namely the bandgap of the PVK decreases. Then, when the temperature reaches T=250 °C, the absorption edge decreases dramatically and the

bandgap reaches the value of E_g~2.38 eV proving the complete conversion of PVK into PbI_2 (Fig. 2.16(D)). On top of that, defect density increases, facilitating charge carriers recombination [83].

Furthermore, when reaching excessively high temperatures during PSC operation as it is exposed directly to sunlight, PVKs may show structural and chemical instabilities which may lead to thermal degradation, as well as phase transformation from the photoactive cubic α phase [5]. This thermal instability may be a consequence of the fact that heat is not effectively dissipated into the material due to the poor thermal conductivity at RT of PVKs. Hence, when the PSC is exposed to the sunlight, heat cannot rapidly spread in the material, leading to the creation of thermal stresses which reduces the device lifetime [90].

2.4.2. Stabilisation Methods

Several methods have been applied to improve the PVK solar cells stability against degradation. This research field is very active and new potential solutions are continuously being developed. Some of these involve composition and morphology modifications of PVK by PVK engineering, incorporation of additives, synthesis conditions and fabrication techniques control, selection of stable materials for the HTL and ETL, modifications of the PVK/HTL or PVK/ETL interfaces, deposition of hydrophobic, self-cleaning, non-reactive and inhibition layers, alterations of the electrodes and, finally, encapsulation of the PSC by glass or polymers to seal it from the outdoor environmental agents [5].

Among all the various methods to prevent PVK from degradation, this MSc Graduation Project report mostly focuses on the PVK compositional engineering and control of morphology and microstructure through synthesis techniques and thermal annealing.

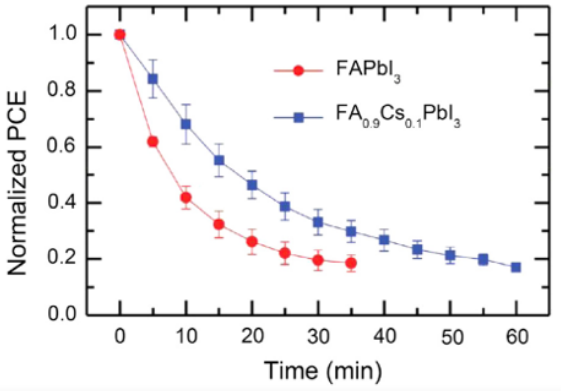

Figure 2.17: Variation of normalized η of $FAPbI_3$- and $FA_{0.9}Cs_{0.1}PbI_3$-based PSCs with time. The measurements have been carried out under continuous white light illumination (100 mW/cm^2) in ambient condition (RH<40%). It can be seen that the incorporation of Cs^+ helps in retaining higher efficiency for a longer time [49].

Compositional engineering is not only useful for intervening on the chemical, physical and optoelectronic properties of PSCs, but it is also extremely advantageous for selecting the constituents of the PVK crystal structure that lead to better long-term resistance of the device to degradation and instability due to the ambient air environment (H_2O and O_2), temperature and mechanical stresses and/or strains. As already explained in Section 2.2, it must be emphasised that by adding a small fraction of elements such as Cs^+ in the A sites of the PVK it is possible to produce PSCs with enhanced stability against degradation, while keeping an high conversion efficiency. Cs^+ stabilises the black α phase at RT and impedes the halide phase segregation. With respect to pure FA-based PVKs, Cs^+ induces a stronger interaction between FA^+ cations in FA-based PVKs and the inorganic octahedra made of I^- anions due to the possibility to obtain an optimum effective Goldschmidt tolerance factor (see Section 2.2.1). The consequent greater contraction of the lattice constant and lower defect density with respect to FA-based PVKs makes the multications PVKs more stable [35, 49, 81, 82]. The stabilising effect of Cs^+ incorporation on degradation of PV performance of PSCs is shown in Fig. 2.17(A) [49]. Moreover, an improved chemical and thermal stability have been observed in the case of mixed-halides PVKs, when I^- is substituted by Br^- [50, 91]. This is probably due to a smaller lattice constant and to the stronger interaction with A cations and the greater stability to oxidation of the latter compared to I^-. These successful techniques suggest that alternative PVK precursors and ion doping might be an effective solution to enhance PVK inherent stability [5, 85, 92].

Moreover, PSCs resistance against degradation can be improved by opting for synthesis techniques lead-

ing to large, homogeneous and dense crystals in PVK polycrystalline thin films to make the contact with moisture more difficult. In addition to that, suitable annealing temperature and time are very important not only for increasing the crystallinity and grain size of the PVK thin-film and thus its stability against degradation as stated before, but also for the whole PSC architecture fabrication and keeping the device working in operative conditions, given that the temperature it reaches under sunlight is far from RT [5].

Finally, considering the contribution of some HTL and ETL materials to the PSC instability, the materials of each layer of the PSC should be carefully selected and the fabrication of both the PVK and the whole PSC must be conducted in low-humidity and low-oxygen conditions to avoid premature degradation of the device due to contact with the H_2O and O_2 in the manufacturing phase [5].

3

Synthesis Techniques, Experimental Methods and Characterisation Techniques

The chemico-physical, optoelectronic and charge-carrier transport properties as well as the structural stability of PVK are essentially defined by its process and conditions of synthesis [5].

There are two principal categories of synthesis techniques for the deposition of polycrystalline PVK thin-films, i.e. solution-based and vapour-based (or vacuum-based) techniques. A distinction can also be made between single-step deposition and multi-step deposition processes. The former includes all those techniques that are based only on a one-step process, while the latter routinely involve the application of a sequence of different steps, which may be related to various techniques to synthesise PVK thin-films (all solution-based, all vapour-based or a combination of them, i.e. hybrid techniques) [5, 93, 94].

PVK thin-films can be produced via a wide variety of synthesis techniques. The herein Chapter 3 will be focused on multisource layer-by-layer thermal evaporation (vapour-based), two-step spin coating (solution-based) and thermal evaporation/spin coating hybrid synthesis techniques, which are shown in Fig. 3.1.

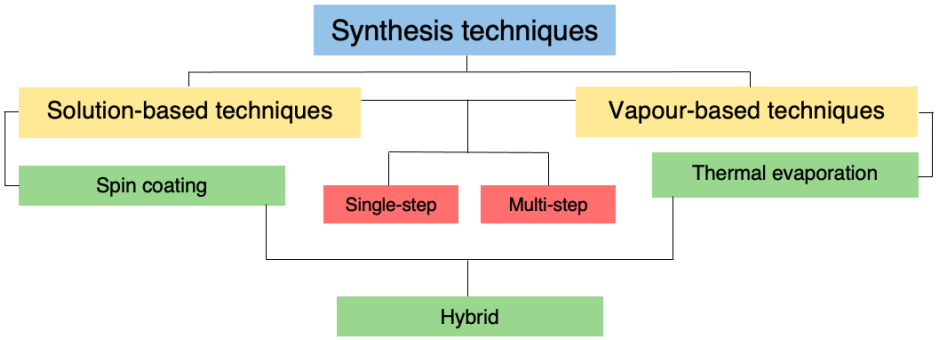

Figure 3.1: Diagram showing the synthesis techniques for the production of PVK thin-films described in the herein **??**. Adapted from [5, 93, 94].

3.1. Vapour-based (or Vacuum-based) Synthesis Techniques

Vapour-based (or vacuum-based) techniques are based on the deposition of the PVK thin-films in vapour phase starting from the PVK precursors, which are ordinary present in the form of solid materials (e.g powders) as sources inside a vacuum chamber. Vapour-based techniques can be carried out by either depositing a single layer in a one-step process or depositing alternating multilayers in different vapour-based steps to produce a PVK thin-film, as seen in Fig. 3.2 [5, 93].

Thermal evaporation belongs to the vapour-based (or vacuum-based) synthesis techniques category [5].

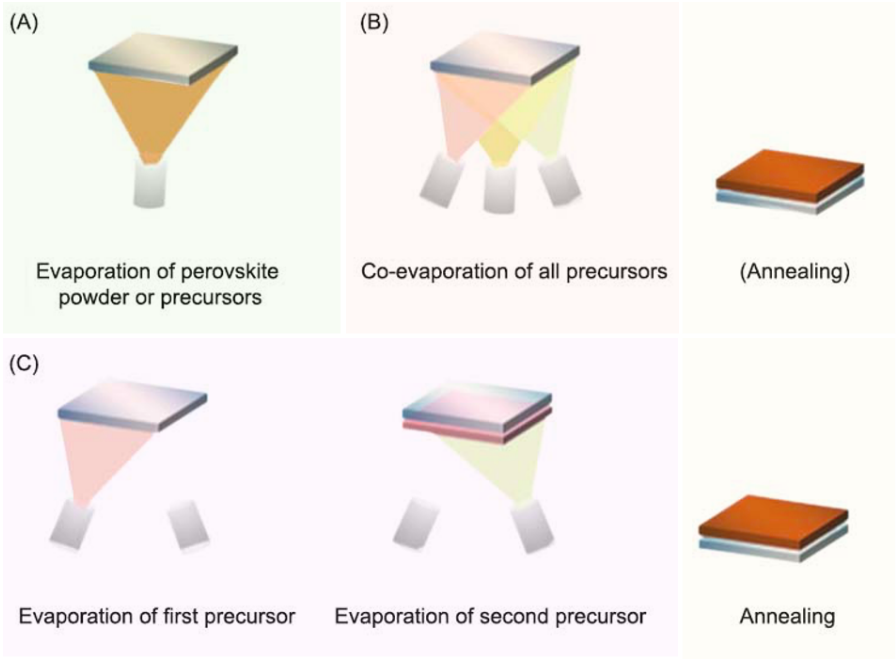

Figure 3.2: Schematic illustration of single layer and multilayers deposition via vapour-based techniques. In this case, the thermal evaporation technique most common modes are shown, i.e. (A) single source, (B) multiple-source co-evaporation and (C) multiple source sequential layer-by-layer evaporation for the synthesis of PVK thin-films [96].

3.1.1. Thermal Evaporation

In thermal evaporation, the desired compounds are directly deposited from PVK precursors in vapour phase for the production of PVK thin-films. It is possible to distinguish between single source (Fig. 3.2(A)) [95, 96] and multiple-source thermal evaporation [96]. The latter can be performed either in co-evaporation mode (Fig. 3.2(B)), when simultaneous evaporation of the different source materials is carried out [19, 48, 89, 97, 98], or in sequential layer-by-layer mode (Fig. 3.2(C)), when stacks of individually deposited alternating layers of the source materials are formed [99–101].

Thermal evaporation enables depositions on wide surfaces to obtain large-area high-quality PSCs. In fact, it ensures complete surface coverage and conformal growth, that helps to level off the lattice mismatch between the PVK layer and the substrate and it is possible to have a certain control over the stoichiometry and thickness of the PVK thin-film, although, as mentioned before, some limitations may be present. Additionally, it benefits from the intrinsic high purity of the evaporated compounds. As a result, PVK thin-films with high crystallinity, homogeneity, uniform thickness and a pinhole-free smooth surface can be obtained by thermal evaporation. However, thermal evaporation depositions typically results in PVK thin-films characterised by smaller grains than those of the PVK thin-films produced by solution-based methods. Besides, no residual molecules of solvents remain in the so-obtained PVK thin films. Lastly, this technique is also completely compatible with conventional semiconductor manufacturing methods [5, 104]. On the other hand, the production process is slow, the materials arrangement is elaborate, time- and energy-consuming HV conditions are required, multi-component materials are quite complicated to synthesise and a careful periodical calibrations to monitor the deposition rate and precursors ratio is needed [5, 104, 105].

Multisource Layer-By-Layer Thermal Evaporation

This MSc Thesis Project analyses multisource layer-by-layer thermal evaporation as synthesis technique compatible for depositions on non-flat substrates. Thus, the herein Fig. 3.2 is focused on this specific method.

In multiple-source thermal evaporation the PVK precursors to be evaporated (typically powders of organic and inorganic salts) are placed separately in crucibles (sources) inside a vacuum chamber [5]. A substrate to be coated is placed on the opposite side with respect to the position of the PVK precursors, facing the sources. The substrate ordinarily rotates during the whole evaporation process to favour the formation of a homogeneous PVK thin film with a uniform thickness. High vacuum (HV) conditions are created inside the thermal evaporation chamber. Then, a large current is applied to the crucibles to increase the temperature and ensure the evaporation of the PVK precursors. In detail, the temperature applied to the source material

has to enable the evaporation of the inorganic component without thermally decomposing the organic part [5]. While the temperature of the source is kept high enough to evaporate the PVK source materials [5], the substrate is maintained at RT as it is optimal for PVK deposition [102]. Essentially, during evaporation the atoms and the molecules of the PVK precursors are thermally released from the source material surface and they travel towards the substrate forming a cone-shaped flow of evaporating material, without any interaction with residual gas atoms thanks to the HV conditions of the chamber. The source materials are sequentially (layer-by-layer mode) evaporated from these individual sources. To be more precise, the multilayer evaporation mode consists in the sequential evaporation of the inorganic and organic compounds that compose the PVK, depositing a MX_2 layer (e.g. PbI_2) and an AX layer (e.g. FAI or CsBr) alternately. In this manner, the PVK precursors are deposited on the substrate forming a PVK thin-film. A quartz crystal microbalance (QCM) placed close to the substrate monitors the deposition rates and the thicknesses of the deposited layers during the process [5].

Although the PVK thin-film is already formed during deposition, after a layer-by-layer evaporation the so-obtained PVK thin-film needs to be annealed. The annealing treatment is carried out afterwards to improve the crystallinity, i.e. to facilitate the complete reaction between the PVK precursors, of the PVK thin-film. Moreover, it has a direct effect on the grain evolution and morphology, thus it helps both in favouring the full cristallisation of the PVK thin-film and relieving the residual internal stresses created within the material after the deposition [5].

Multiple-source thermal evaporation needs a rigorous control of the precursors molar ratio. By monitoring the deposition rates and and the thicknesses of each single source material which is evaporating during the process, it is possible to control the PVK precursors composition, the crystal structure and the morphology of the PVK thin-film. The possibility of a certain degree of control on the processing parameters implies a good level of reproducibility of the PVK thin-films. However, controlling the deposition rates can be difficult due to the difficulty to control the temperatures of the sources and of the substrate and to the fact that the vapour pressure of the organic component is usually higher than that of the inorganic one. Hence, vapour-based techniques often leads to non-stoichiometric PVK thin-films, due to re-evaporation, dissociation or decomposition of the organic component in the vacuum chamber [5].

3.2. Solution-based Synthesis Techniques

Solution-based techniques consist in the synthesis of PVK thin-films in the liquid phase, involving the formation of the crystals in a solvent containing the PVK precursors, which are substances that often show good solubility. A schematic of the main steps of solution-based techniques for the synthesis of PVK thin-films is shown in Fig. 3.3 [5]. Solution-based techniques do not only consist in the deposition of a single layer (one-step process). In fact, it is also possible to perform a sequence of different solution-based steps (multi-step process) to form the PVK thin film [5]. For instance, sequential spin coating can be defined as multi-step techniques [93].

The most commonly used solution-based synthesis technique is spin coating [5, 93, 94].

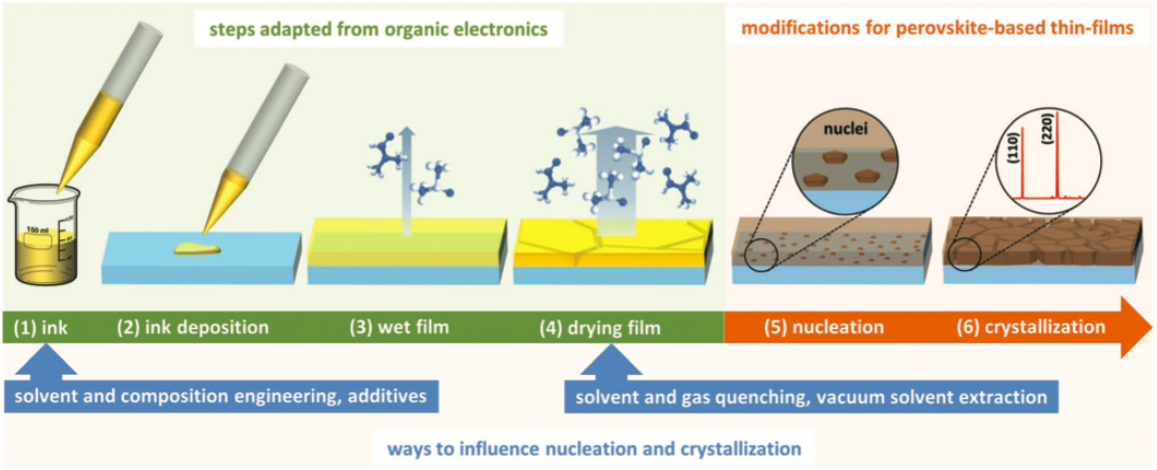

Figure 3.3: Schematic of the solution-based techniques main steps for PVK polycrystalline thin-films synthesis. In blue, some methods to optimise the quality of the PVK thin films are suggested [94].

3.2.1. Spin Coating

Spin coating is one of the most common, well-known and fast solution-based process for PVK thin-films synthesis and, more generally, for depositing also other layers in the architecture of PSCs.

As a solution-based process, the PVK precursors (solutes) for the formation of the PVK thin-film are deposited in the liquid phase (one or more solvents). Different PVK precursor compounds in different ratios can be used. The typical compounds used as precursors are one or more inorganic halides BX_2 (e.g. B = Pb; X = I, Br) and one or more organic halides AX (e.g. A = FA, Cs). These have to be dissolved in an appropriate ratio in a suitable solvent [5]. Certain precursors offer the possibility to be dissolved in the same solvent in appropriate proportions. In this case, the solution-based processing must be carefully controlled considering the rapid intercalation reaction and the potentially conflicting wetting characteristics of the substrate in relation to the different compounds that are being deposited [5]. On the other hand, it can also happen that the solvent for the organic precursor may not be suitable for the dissolution of the inorganic one, thus the PVK components may be dissolved separately in different solvents. The incompatibility of one of the precursors with the solvent of the other may lead to unsatisfactory film quality. This is one of the main disadvantages of solution-based methods. Two of the most commonly employed solvents are N,N dimethylformamide(DMF) and dimethylsulfoxide (DMSO). It is possible to use them either individually or by creating a mixture of them, depending on the solubility and compatibility of the selected PVK precursors. The choice of the solvents alters the morphology of the PVK crystallites [5].

The spin coating synthesis technique is based on either the dripping of a single solution containing all the PVK precursors in an appropriate ratio (one-step) or the alternating deposition on a substrate of the inorganic solution, followed by the organic solution (two-step). The solution is then spread over the substrate surface by spinning it at constant rotation and high speed. Then the substrate is dried, typically via annealing, to remove the excess solvents, promote the formation of a thin-film of PVK crystals and improve the PVK crystallinity, microstructure and morphology. The annealing temperature should be sufficiently high to allow the crystallisation of the PVK films, but it should not be above a certain value to ensure good coverage of the substrate [5].

The main factors affecting the crystallinity, phase purity, uniformity, surface morphology and interface features of the spin-coated PVK thin-films are the precursor solution composition, the substrate surface morphology, the processing parameters of the deposition (rotational speed of the substrate, reaction temperature and deposition time) and the annealing steps (temperature, time and ramping rate) and, lastly, the external environmental conditions, e.g. oxygen and humidity levels. Besides, the layer thickness is controlled by the spinning velocity, temperature and solution viscosity [5].

Very high-quality PVK thin-films can be synthesised by spin coating technique by a careful solvent selection taking the nature of the PVK precursors into account and an accurate control of the processing parameters. Moreover, it also allows the thickness of the layer to be adjusted according to preference, although it cannot be fully controlled. In addition to that, large substrate areas can be coated with small amounts of solutions and the deposition of multilayered materials is possible. Finally, it is a very fast and low cost technique. However, spin coating is also characterised by some disadvantages like material losses (>90%), non-uniform layer thickness and issues of compatibility of the spin-coated PVK thin-films with the substrate. In fact, spin coating typically leads to the synthesis of PVK thin-films characterised by dendritic grains, which creates a certain discontinuity in the material in the form of many gaps and pinholes, that in turn leads to the formation of defects. As a result, spin coating does not enable uniform surface coverage and conformal growth. Furthermore, the lack of solvents that are simultaneously able to dissolve all the PVK precursors, leading consequently to their separate dissolution in two different solvents, and the fast reaction rate of the PVK precursors may lead to low-quality thin-films too. Lastly, another drawback associated with spin coating is its sensitivity to environmental and human factor [5], which reduces the reproducibility of spin-coated PVK thin-films.

Two-Step Spin Coating

This MSc Thesis Project analyses two-step spin coating as preliminary study for the development of the thermal evaporation/spin coating hybrid synthesis technique, as spin coating is not compatible for depositions on non-flat substrates. Thus, the herein Section 3.2.1 is focused on this specific method.

The two-step spin-coating synthesis technique consists in spin coating a solution of inorganic PVK precursors (e.g. CsBr and Pb_2) on a substrate, followed by the subsequent spin coating of an solution of organic PVK precursors (e.g. FAI) on top of the aforementioned inorganic thin-film [5].

The multi-step solution processes overcome the issues of poor surface coverage and highly porous morphologies of the PVK thin-films produced by single-step solution deposition method. In addition, they also make possible to produce more dense, uniform and conformal PVK thin-films. However, they usually show a rather rough surface too. In this respect, it is important to carefully balance the trade-off between the grain size and the surface roughness of the PVK thin-film. A PVK characterised by large grains exhibits superior charge carrier transport properties, but also a considerable surface roughness, which causes higher surface recombination and leakage current. On the contrary, a PVK film with small grains presents a smoother surface, but it can also show lower carrier lifetimes and shorter diffusion lengths. The higher the organic solution concentration, the smaller the grains, the smoother the surface, but the worse the electron and hole transport properties may be [5]. The multi-step solution processes suffer from some disadvantages too. The thin films produced with these techniques may peel off (delamination) from the substrate [5]. In addition to this, the PVKs synthesised by these methods usually present only a partial conversion of the inorganic thin-film. The unreacted inorganic PVK precursors reduce the light absorption and hamper the charge carriers transport [5, 105].

3.3. Hybrid (Thermal Evaporation/Spin Coating) Synthesis Techniques

Hybrid techniques are based on the combination of vapour-based and solution-based processing steps.They are particularly interesting because of the controlled deposition of PVKs due to the decoupling of the inorganic and organic depositions. Various synthesis techniques can be typically combined in a multi-step process. Thus, they consist of sequential deposition steps and are based on interdiffusion processes. Firstly, inorganic PVK precursors (e.g. CsBr and PbI_2) are usually deposited by physical vapor deposition (PVD) or chemical vapor deposition (CVD) technique. Subsequently, the integration of organic PVK precursors (e.g. FAI) takes place by powder, vapour or solution [93].

Hybrid synthesis techniques have been developed to improve the quality of PVK thin-films, as the advantages on both technique are put together. In fact, it allows a partial control on molar ratio and thickness, thickness uniformity, homogeneous and uniform surface coverage, conformal growth and a high level of reproducibility. On the other hand, the main drawbacks are related to the fact that the processing is generally slow and infiltration and interdiffusion reaction failures can take place in certain conditions [5, 93, 108].

The hybrid synthesis technique analysed in this MSc Thesis Project consists in in the deposition of a bilayer made of the PVK inorganic precursors (e.g. CsBr and PbI_2) by thermal evaporation, on top of which a solution of the organic PVK precursors (e.g. FAI in IPA) is spin coated. Finally, an annealing treatment is performed to remove the residual solvents, activate the interdiffusion reaction between the PVK precursors and the crystallisation of the PVK and improve the PVK crystallinity, microstructure and morphology.

The conversion of the PVK precursors to PVK takes place through a heterogeneous phase reaction between the thermally evaporated bilayer of $CsBr/PbI_2$ and FAI. The organic PVK precursor must intercalate into the predeposited inorganic layer by a dissolution–crystallization process.

The efficacy of this reaction and the final PVK thin-film morphology depend significantly on the initial features and properties of the inorganic bilayer. It has been observed a coexistence of crystallites aggregates of PVK and unreacted $CsBr+PbI_2$. This seems to derive from the rapid crystallisation of the surface of the inorganic bilayer as soon as the organic solution is spun on it. This crystallised surface would act as capping layer, hindering the effective infiltration and diffusion of the organic solution into the inorganic bilayer. Consequently, the PVK conversion does not take place completely.

As a conclusion, a table describing the main advantages and disadvantages of the three synthesis techniques for PVK thin-films deposition analysed in this MSc Thesis Project is shown in Table 3.1 [5, 93, 94].

Table 3.1: Comparison between the main advantages and disadvantages of thermal evaporation, spin coating and hybrid synthesis techniques for PVK thin-films deposition analysed in this MSc Thesis Project [5, 93, 94].

Category	**Technique**	**Advantages**	**Disadvantages**
Solution-based	Spin coating	Low cost Simple Fast processes Low-temperature processes Easily adjustable layer thickness Multilayer deposition Low lab cost investment regarding infrastructure Potential scalability	Dependence on the solubility of elements Use of hazardous solvents Strong dependence of uniformity, morphology, and conformality on solubility of elements Process parameters and crystal growth difficult to control Necessity of substrate wettability Pinholes formation and halide segregation Coating material loss
Vapour-based	Thermal evaporation	Film stioichiometry, thickness, morphology, and uniformity control Conformal and directional crystal growth Good surface coverage Easy monitoring of the process Solvent-free Enhanced reproducibility Potential scalability	Slow process Complex equipment Necessity of HV Limited deposition rate control of the organic components Precursors susceptible to thermal/high energy decomposition Multicomponent materials difficult to synthesise
Hybrid	Thermal evaporation + spin coating	Uniform layer thickness Conformal growth of coatings Good surface coverage Enhanced reproducibility Potential reduction of process temperature and pressure Potential scalability	Slow process Interdiffusion failure for micro-scale thicknesses

3.4. Experimental Methods

All the PVK thin-films handling and storage has been carried out in gloveboxes, one of which shown in Fig. 3.4, inside which there is an atmosphere of N_2 with very low concentrations of O_2 and H_20. These concentrations are constantly analysed and keep under control to protect the PVK thin-films.

It is important to specify that spin coating is carried out inside the glovebox to protect the PVK thin-films from the atmospheric moisture and oxygen during their synthesis. For the same reason, all the annealing treatments have been performed in the glovebox too.

3.4.1. Substrate Preparation

Two different types of substrates, i.e. glass and quartz, have been used for the PVK thin-film deposition. The substrate preparation is carried out by firstly cleaned with acetone and then performing an UV-ozone cleaning of the surface in a vacuum atmosphere of pressure P~10^{-1} for t=2 min for the thermal evaporation and thermal evaporation/spin coating hybrid synthesis and t=5 min for the spin coating synthesis. The UV-ozone cleaning is carried out to remove a variety of contaminants from the substrates surface, in particular dust and salts which cannot be turn into volatile products thanks to the oxidizing action of UV/ozone [**?**]. A photograph of the UV-ozone cleaner used in this MSc Thesis Project is shown in Fig. 3.5.

Figure 3.4: Photograph of one of the glovebox for PVK thin-films handling and storage.

Figure 3.5: Photograph of the UV-ozone cleaner.

3.4.2. Perovskite Thin-films Synthesis

Thermally Evaporated Perovskite Thin-films

The multisource layer-by-layer thermal evaporation synthesis technique analysed in this MSc Thesis Project is based on the evaporation of three source PVK precursors in the form of powders, i.e. CsBr, PbI_2 and FAI, inside a chamber where HV conditions are created (P=$10^{-6/7}$ mbar), which can be seen in Fig. 3.7(A). The source materials are placed inside three crucibles, that are heated up by an electrical power applied to the heating elements. The opening of the crucibles, which can be opened and closed independently by shutters, as shown in Fig. 3.7(B), is directed towards the sample holder containing the substrates on which PVK is intended to be deposited, which is located above them facing the source materials. The sample holder and consequently the substrates are shielded from the thermally evaporated materials by a large shutter. After heating up the three

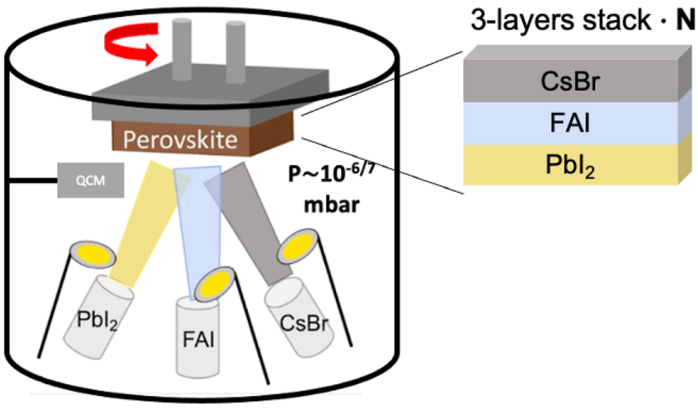

Figure 3.6: Schematic representation of a three-source thermal evaporation instrument operating inside a chamber in HV conditions. The three source materials powders are heated up in the crucibles and thermally evaporated individually. The QCM-based sensor close to the substrate measuring the deposition rates and relative thicknesses is also visible. The rotation of the substrate that takes place during the deposition process to ensure the PVK thin-film homogeneity and thickness uniformity is indicated with an arrow. The illustration shows CsBr, PbI_2 and FAI as inorganic and organic PVK precursors in a layer-by-layer deposition. The three-layers stack, consisting of single layers of PVK precursors in the order CsBr/PbI_2/FAI, is repeated N times until the desired final thickness of the PVK thin-films obtained. Adapted from [89].

sources to different temperatures corresponding to the desired deposition rates, the layers of PVK precursors are individually deposited by opening the shutters. The deposition of each source material is performed for a time sufficient to deposit the set thickness. For each source material, a QCM-based sensor place midway between the sources and the substrates monitors the deposition rate and calculates the thickness of the deposited layer from the source material density. This process leads to the formation of three-layers stacks (layer-by-layer deposition process), which are repeated a number (N) of times to achieve the final thickness of the PVK thin-film. Finally, an annealing treatment is performed.

A schematic illustration of the multisource (three-source) layer-by-layer thermal evaporation synthesis technique on which this MSc Thesis Project focuses is shown in Fig. 3.6.

The processing parameters of the multisource (three-source) layer-by-layer thermal evaporation applied in this MSc Thesis Project are indicated in Table 3.2.

Table 3.2: Processing parameters of multisource (three-source) layer-by-layer thermal evaporation.

Processing parameter	**CsBr**	**FAI**	**PbI_2**
Precursor molar ratio	0.25	0.85	1.1
Single layer thickness (nm)	1.1	6.3	8.2
Deposition rate (Å/s)	0.07	0.3	0.3
Source materials temperature	≥210 °C	≥93 °C	~369 °C

The annealing temperature and time applied to the resulting thermally evaporated PVK thin-films are not indicated, as the parameters are extensively varied during the optimisation process in Section 4.2.

Spin-coated Perovskite Thin-films

Spin coating synthesis is entirely carried out inside the glovebox. After stirring the PVK precursors solution for one night on a magnetic plate, the solution are filtered by a PTFE membrane with pore size 0.22 μm. Afterwards, after cleaning preparation, the solution is dripped evenly over the substrate by the aid of a pipette and then the substrate spinning is immediately activated to spread it. Finally, the sample is annealed if required by the experiment.

In a nutshell, the two-step the spin coating synthesis technique developed in this MSc Thesis Project and described in the herein Section 5.1 is divided in two+one steps:

1. **Step 1**
   Deposition on a spinning substrate with the aid of a pipette an inorganic solution of CsBr and PbI_2 in a mixture of N,N-dimethylformamide (DMF) and dimethyl sulfoxide (DMSO), forming an inorganic layer as a result;

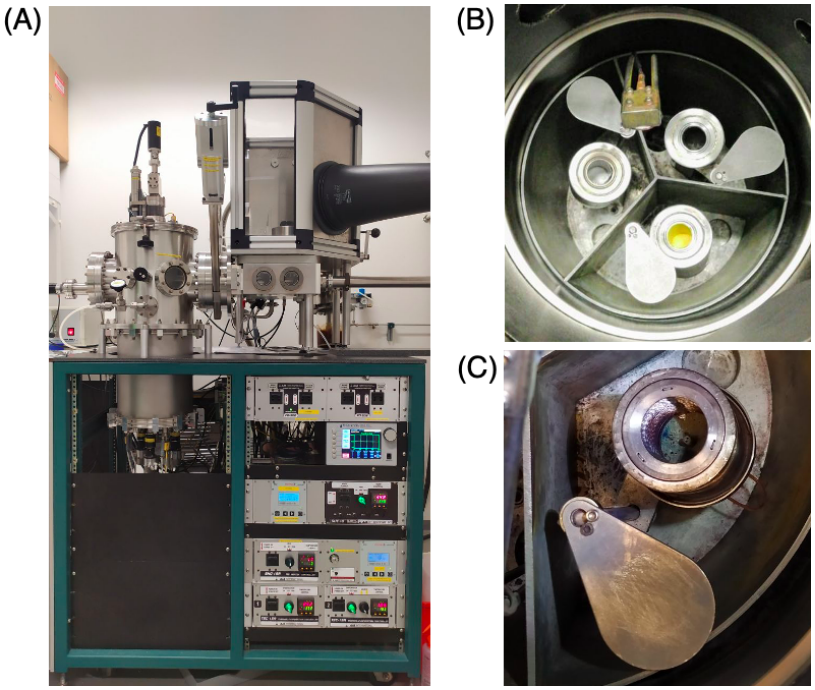

Figure 3.7: Photographs showing (A) the thermal evaporator instrument setup, where the vacuum chamber, the two load locks and the movable/rotating shafts for the substrate positioning and the chambers pressure, substrate rotation and thermal controllers are visible, (B) the configuration of the three crucibles containing the powders of the PVk precursors, shutters and the QCM-based sensor and (C) one of the small shutters which allow to open and close the crucible.

2. **Step 2**
   Deposition on the previously spin-coated inorganic layer, following the same procedure, of an organic solution of FAI dissolved in isopropanol (IPA).
3. **Annealing**
   Annealing treatment to foster the reaction between the PVK precursors, evaporate the residual solvent and improve the crystallinity and microstructure of the PVK thin-film.

A schematic illustration of the two-step spin coating hybrid synthesis technique studied in this MSc Thesis Project is shown in Fig. 3.8.

The processing parameters related to step 1, namely related to the spin coating of the inorganic layer, used in this MSc Thesis Project are indicated in Table 3.3.

Table 3.3: Processing parameters of the inorganic solution of CsBr and PbI_2 PVK precursors dissolved in a mixture of DMSO/DMF.

V_{DMF} (mL)	V_{DMSO} (mL)	$V_{CsBr+PbI_2}$ (μL)	M_{CsBr} (mol/L)	M_{PbI_2} (mol/L)	ω_{cyc} (rpm)	t_{spin} (s)
1	$0.09863 \cdot 10^{-3}$	80-100	$0.204 \cdot 10^{-3}$	$1.2 \cdot 10^{-3}$	3000	30

Where $V_{CsBr+PbI_2}$ is the spun volume of the inorganic solution, M_{CsBr} the concentration of CsBr in solution, M_{PbI_2} the concentration of PbI_2 in solution, ω_{cyc} is the spinning rotational speed and t_{spin} is the spinning time.

By looking at Table 3.3, it can be noted that the amount of inorganic solution varies, as volumes of 80 μL and 100 μL are spun. depending on the experiment (see Section 5.1). Moreover, the DMF:DMSO solvents ratio is instead close to 10:1. Finally, considering the concentrations in solution of CsBr and PbI_2, it can be observed that the molar ratio of the inorganic precursors CsBr:PbI_2 is equal to 0.204:1.2, thus the molar fraction of CsBr compared to PbI_2 is is 17 mol%.

The processing parameters related to step 2, namely related to the spin coating of the organic layer, used in this MSc Thesis Project are indicated in Table 3.4.

It can be seen from Table 3.4 that the amount of organic solution changes. Two spun volumes are tested, i.e. 80 μL and 120 μL. In addition to that, the FAI concentration takes on three values, i.e. 0389, 0.469 and

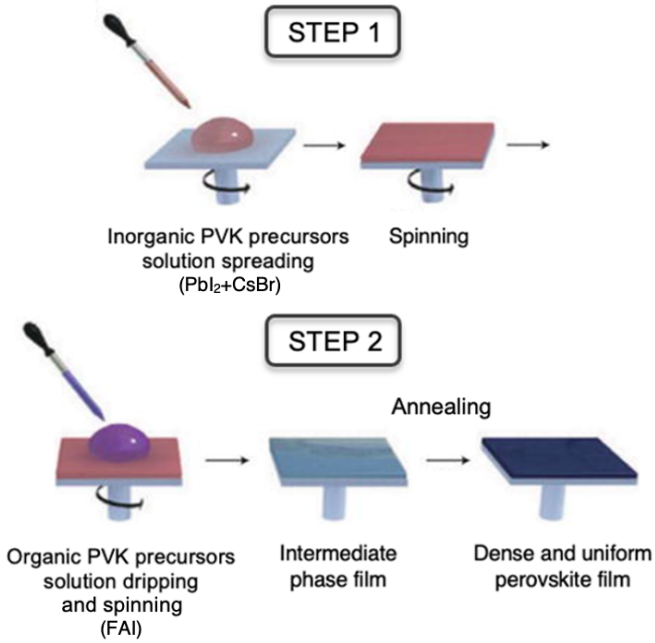

Figure 3.8: Schematic representation of the main steps of the two-step spin coating technique. Adapted from [107].

0.548 mmol/L. Lastly, it can be observed that the spin coating rotational speed and time of step 2 are the same of those of step 1.

The annealing temperature and time applied to the resulting spin-coating PVK thin-films are not shown as they are investigated in the optimisation process presented in Section 5.1.3.

Table 3.4: Processing parameters of the organic solution of FAI PVK precursor dissolved in IPA.

V_{IPA} (mL)	V_{FAI} (μL)	M_{FAI} (mol/L)	ω_{cyc} (rpm)	t_{spin} (s)
1	80-120	0389-0.469-0.548 $\cdot 10^{-3}$	3000	30

Hybrid Perovskite Thin-films

In few words, the hybrid synthesis technique developed in this MSc Thesis Project and described in the herein Section 5.2 consists in three steps:

1. **Thermal evaporation of the inorganic layer**
   Deposition via layer-by-layer multisource thermal evaporation of a thick layer of PbI_2 over a thin one of CsBr, resulting in an inorganic bilayer;
2. **Spin coating of the organic solution**
   Subsequent deposition via spin coating on the previously thermally evaporated inorganic layer of an organic solution of FAI dissolved in isopropanol (IPA);

Table 3.5: Processing parameters of the inorganic layer deposited via thermal evaporation in the multisource (three-source) layer-by-layer thermal evaporation.

Processing parameter	CsBr	PbI_2
Precursor molar ratio	<0.1	1
Single layer thickness (nm)	18	360
Deposition rate (Å/s)	0.2	0.7
Source materials temperature	≥380 °C	≥242 °C

Table 3.6: Processing parameters of the organic solution of FAI PVK precursor dissolved in IPA.

V_{IPA} (mL)	V_{FAI} (μL)	M_{FAI} (mol/L)	ω_{cyc} (rpm)	t_{spin} (s)
1	120	$0.469 \cdot 10^{-3}$	3000	30

3. **Annealing**
   Annealing treatment to foster the reaction between the PVK precursors, evaporate the residual solvent and improve the crystallinity and microstructure of the PVK thin-film.

A schematic representation of the thermal evaporation/spin coating hybrid synthesis technique on which this MSc Thesis Project focuses is shown in Fig. 3.9.

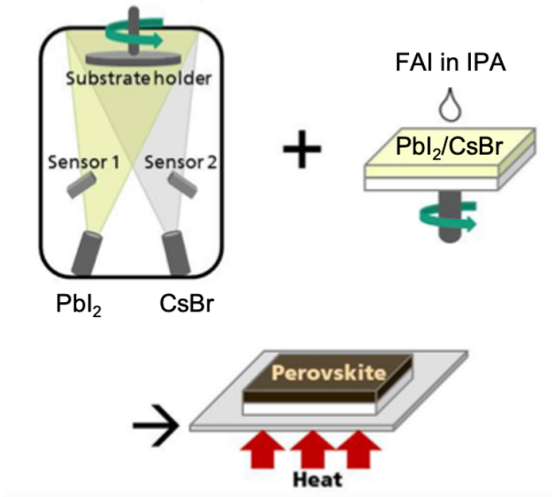

Figure 3.9: Schematic illustration the thermal evaporation/spin coating hybrid synthesis technique. The inorganic PVK precursors (CsBr and PbI_2) are deposited via thermal evaporation to form a CsBr/PbI_2 bilayer. Subsequently, the organic PVK precursor in solution (FAI in IPA) is spun on it via spin coating. As a result an intermediate PVK phase is formed. Finally, an annealing treatment is performed to complete the interdiffusion reaction between the PVK precursors and convert the intermediate PVK phase in a compact and uniform PVK thin-films. Adapted from [108].

The processing parameters related to the deposition via thermal evaporation of the inorganic layer in the hybrid synthesis process, which are used in this MSc Thesis Project, are presented in Table 3.5.

Then, the processing parameters related to the spin coating of the the organic layer which are used in this MSc Thesis Project are presented in Table 3.6.

Finally, the resulting hybrid PVK thin-films are annealed at T=135 °C for t=15 min.

3.5. Characterisation Techniques

3.5.1. Profilometry

Profilometry is a characterization technique that allows to measure the profile of the surface of sample. One of its main functions is to measure the step heights and thereby the thickness of films, so it is widely applied in the case of PVK thin-films analysis. In addition to this, it can be used to analyse the smoothness/roughness, waviness, texture and morphology of the sample surface [109].

The instrument used in case of this MSc Thesis Project is a Veeco/Bruker Dektak 8 Stylus Profilometer. This profilometer is based on the direct mechanical contact between a sharp stylus probe and the sample surface. A system controller connected to a PC is used to locate the stylus, adjust the stylus load and the line scanning speed and length, to take the measurement and to analyse the obtained data (Fig. 3.10(A)). Moreover, other components of the profilometer are the substrate holder, the base plate with a line scanning system and the vibration isolation frame [109].

After creating two parallel scratches on the PVK thin-film and revealing the underlying substrate, the stylus of the profilometer scans the surface along a variable line path perpendicular to the scratch. The stylus

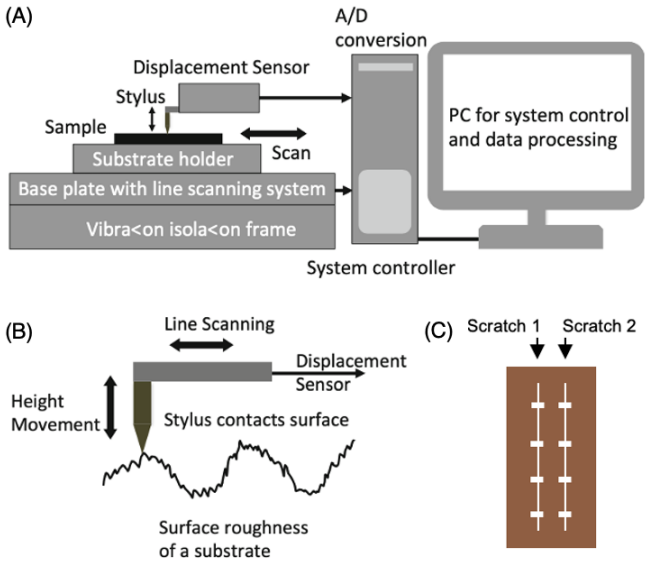

Figure 3.10: (A) Schematic of a profilometer stylus and its relative movements with respect to the sample surface. (B) Schematic of the surface profilometer main components [109].

force (load) has been set as 5 mg (~50 μN). The vertical displacement of the tip due to the sample surface variation of thickness and roughness during the stylus linear motion is detected by a displacement sensor unit (Fig. 3.10(B)) [109]. In this manner, the surface profile is determined. To be more precise, the displacement sensor connected to the stylus is a linear variable differential transformer able to detect displacements with resolution of 0.334 μm/sample determined by the stylus tip diameter of 12.5 μm. The data processing carried out on the PC unit typically allows to measure an arithmetical mean deviation of roughness profile (Ra) and the height difference between two cursors (R and M). The cursors can be located at desired positions of the surface profile to measure the height difference, i.e. the thickness of the thin-film. After measuring the thickness in several spots along each one of the two scratches (Fig. 3.10(C)), an average thickness value is calculated.

3.5.2. UV-Vis-NIR Spectroscopy (UV-Vis-NIR)

Ultraviolet-visible-near-infrared spectroscopy (UV-Vis-NIR) is an important characterization technique for the analysis of the optical properties of PVK in the ultraviolet, visible and near-infrared region of the spectrum. Not only absorption, but also transmission and reflection can be investigated (Fig. 3.11(A)). From the UV-Vis-NIR measurements, it is possible to evaluate the bandgap and the amount of absorbed light in the PVK thin-film. This allows to detetermine the theoretical limit of the PCE and other photovoltaic parameters of the related PSC. In addition to this, other sample properties can be retrieved from the optical spectra, such as the thickness. Moreover, it is non-destructive and nonintrusive [110].

As can be observed in Fig. 3.11(B), when a material absorbs energy in the form of a photon, an electronic transition from an initial state to an excited energy state takes place inside the atom or the molecule. The smaller the energy required for an electron to be excited from one state to the other or, in case of semiconductors such as PVK, to overcome the E_g between VB and CB, the longer the wavelength of light the material can absorb. Conversely, if the energy gap between the initial and final states is remarkably large, the material will absorb short-wavelengths photons [110].

The measurements present in this MSc Thesis report have been carried out via a PerkinElmer LAMBDA 1050+ UV/Vis/NIR Spectrophotometer with a 150 mm integrating sphere. The integrating sphere is a cavity whose inner walls are made of a highly reflective material. The use of the integrating sphere is particularly important in the case of PVK polycrystalline thin films. In fact, the presence of many crystallites is at the origin of considerable reflection, scattering and interference optical effects, which would lead to errors in determining the absorption properties in standard UV-Vis-NIR measurements [110].

A schematic illustration of the instrument can be seen in Fig. 3.11(C). During an UV-Vis-NIR measurement, light of different wavelengths is passed through the PVK thin-film. Two different light sources are employed: a tungsten lamp emitting wavelenghts in the visible-NIR range and a deuterium (D2) lamp generating

UV light. Then, the light is filtered by a monochromator which selects the wavelengths to be directed onto the thin-film. The output electromagnetic radiation is splitted so that to strike both a reference spot inside the integrating sphere and the PVK thin-film under investigation.

The PVK thin-film under examination is placed in different positions in the spectrometer according to the optical property to be measured. The absorbance spectrum is obtained by locating the thin-film inside an integrating sphere. This component of the instrument allows the contribution of the total scattering and reflection components to be taken into account, thus providing a more accurate measurement. The transmittance and reflectance spectra are measured by placing the thin-film outside of it, on the front side and on the rear side of the integrating sphere, respectively [110] (Fig. 3.11(D)).

Different photodetectors collect the signals. The spectrophotometer used during this MSc Thesis Project is characterised by Peltier-cooled PbS and InGaAs detectors, which are located at the bottom of the integrating sphere. The signals are then processed to be analysed [111]. All the optical parameters are measured for each given wavelength of light and by scanning through all the wavelengths from UV to visible to near-IR spectral range, the complete absorbance spectrum (and the complementary transmittance spectrum) of the material is obtained. Transmittance and reflectance are measured in the same way [110].

The optical properties of plain glass and quartz substrates have been measured too, so that it has been possible to subtract their contribution from the final UV-Vis-NIR measurements of the PVK thin-films.

The absorption is quantified by the Beer-Lambert law, shown in Eq. (18):

$$A = -\log_{10}\left(\frac{I_T}{I_0}\right) = -\log_{10}(T) \tag{18}$$

Where A is the absorbance, I_T is the intensity of the transmitted light and I_0 is the intensity of the incident light. I_0 is measured by carrying out a measurement inside the integrating sphere without placing any sample inside [110]. The ratio I_T/I_0 is equal to the transmittance (T), expressed in percentage.

Thus, as mentioned earlier, by measuring the absorbance spectrum it is also possible to extract the transmittance one directly and vice versa [110].

The reflectance (R), expressed in percentage, is defined by the ratio shown in Eq. (19):

$$R = \frac{I_R}{I_0} \tag{19}$$

Where I_R is in this case the intensity of the light reflected by the PVK thin-film under investigation, which is measured in relation to the reflection of the reference measurement of I_0 [110].

To conclude, the absorbance can also be expressed and calculate as in Eq. (20):

$$A = \frac{I_A}{I_0} = 1 - T - R = \frac{I_0 - I_T - I_R}{I_0} \tag{20}$$

The UV-Vis-NIR absorption measurements can be used to estimate the optical bandgap of the PVK under investigation. Several methods can be applied for its calculation. The bandgap can be roughly calculated in a simple way considering the wavelength corresponding the onset of the absorption in the absorbance spectrum and Eq. (21):

$$E_g = \frac{hc}{\lambda} \tag{21}$$

where h = 6.626 x 10^{-34} Js is the Planck constant, c = 3 x 10^8 m/s is the speed of light and λ is the wavelength of light [110].

Another more accurate method is based on the creation of a Tauc plot [110]. This requires the calculation of the absorption coefficient (α) from the transmittance and reflectance data (Eq. (22)) [113]:

$$\alpha = -\frac{1}{d} \cdot ln\left(\frac{T}{(1-R)^2}\right) \tag{22}$$

In all the previous equations, d is the thickness of the thin-film [113].

The relationship between α and the absorbance is given in Eq. (23) [110]:

$$(\alpha h\nu)^{\frac{1}{n}} = A^{\frac{1}{n}} h\nu - A^{\frac{1}{n}} E_g \tag{23}$$

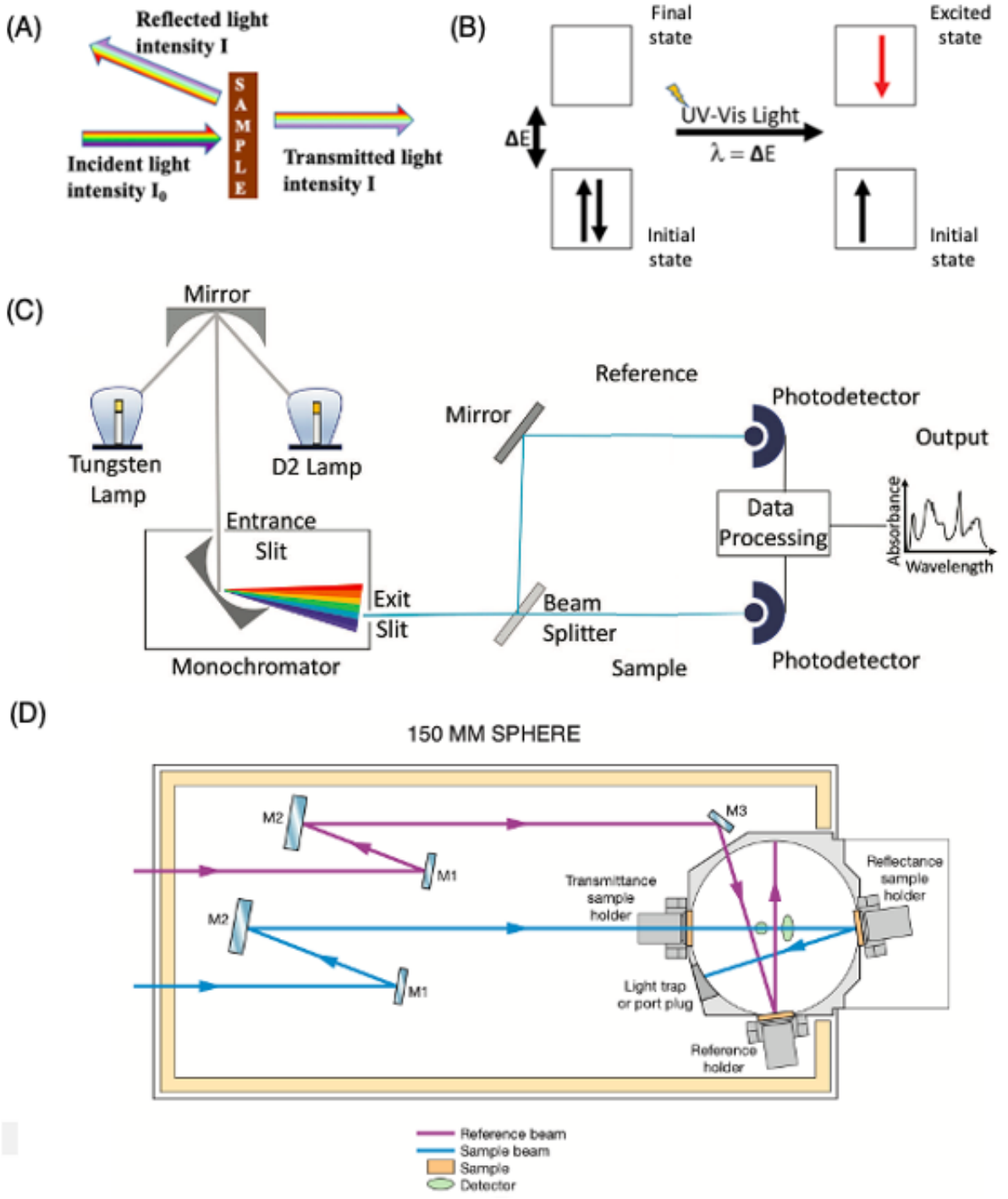

Figure 3.11: (A) Representation of the optical components of reflected light and transmitted light upon absorption and generated when the incident light I_0 hits the PVK thin-film during an UV-Vis-NIR measurement [110]. (B) Schematic of the effect of light absorption to stimulate an electron transition between an initial and a final (excited) level. The energy gap between them is indicated as ΔE [111]. (C) Schematic illustration of the different components of the UV-Vis-NIR spectrophotometer [111]. (D) Schematic representation of the optical design of the UV-Vis-NIR spectrometer, showing the 150 mm integrating sphere and the positions where the test PVK thin-film has to be placed to measure either the transmittance or reflectance spectrum [112].

Where n is a parameter related to the nature of the bandgap of the semiconductor [110]. As explained in Section 2.1.3, PVKs are characterised by a direct bandgap ($n = \frac{1}{2}$), which allows the absorption of a remarkable amount of light in just 200-400 nm thick PVK absorber layer.

In addition to that, the photon energy E_{ph}=hν can also be expressed in eV units by Eq. (24):

$$E_{\text{ph}}(eV) = \frac{1240}{\lambda(nm)} \tag{24}$$

The Tauc plot is build by plotting $(\alpha h\nu)^{\frac{1}{n}}$ against $h\nu$. Then, the linear fit (slope) of the linear section of the plot is drawn to determine its intercept with the hν axis ($(\alpha h\nu)^{\frac{1}{n}} = 0$). This corresponds to the value of the bandgap E_g of PVK. Although it is approximation, this method is widely applied in the solar cells research field to obtain information about the E_g of the PVK under examination [110].

3.5.3. X-Ray Diffraction (XRD)

X-ray diffraction (XRD) is a characterization technique which allows to obtain information about a wide variety of chemical, microstructural and morphological properties of materials, e.g. the crystal structure, symmetries, displacements, defects, micro-crystallinity, orientations, stresses, strains, phase transitions and thermal expansion. These features can be analysed from the sub-Å molecular scale of the PVK to the PSC scale, so XRD measurements can help to investigate strategies to obtain chemically and structurally stable PVKs to extend the PSCs lifetime. In conclusion, XRD is an extremely powerful characterisation technique for PVK thin-films analysis [110].

The working principle of XRD is based on the X-rays diffraction from crystals. Considering the use of monochromatic X-rays that are elastically scattered and diffracted from the electron clouds around the nuclei of the atoms, the Laue condition, shown in Eq. (25), allows to understand when it is possible to observe a constructive interference for reflection by an arrangement points. These points correspond to hypothetical atoms lying on the crystal lattice planes. This condition must be fulfilled to have diffraction:

$$\mathbf{R} \cdot (\mathbf{k} - \mathbf{k'}) = 2\pi\mathbf{m} \tag{25}$$

Where **k** and **k'** are the wavevectors of the incoming (incident) and outgoing (diffracted) beam, respectively, **R** is the Bravais lattice vector of the crystal and **m** the Miller indeces of the family of crystal lattice atomic planes giving diffraction [110]. An equivalent form for this equation is given in Eq. (26):

$$e^{i(\mathbf{k}-\mathbf{k'})\cdot\mathbf{R}} = 1 \tag{26}$$

Where the difference **k**-**k'** = Δ**k** can also be defined as scattering vector [110].

An analogous equation, which can be seen in Eq. (27), has been developed to describe the same situation under a geometrical viewpoint. This is defined as Bragg's law and it expresses the condition for constructive interference for specular reflection by planes. Similarly, this must be fulfilled to have diffraction in the crystal:

$$2d_{\text{hkl}} \sin\theta = n\lambda \tag{27}$$

Where d_{hkl} is the interplanar distance between the diffraction crystal lattice family of planes identified by a specific set of Miller indeces (h k l), θ is the incident angle, i.e. the angle correspondent to diffraction intensity maxima (peaks) that are created in the diffraction pattern as consequence of constructive interference, n is a positive integer related to the diffraction order and thus to the Bragg peaks and λ is the wavelength of the incoming X-rays [110].

Two instruments have been used for this MSc Thesis Project, namely a Bruker-D8-Advance X-ray Diffractometer with Co-Kα X-rays source, i.e. based on cobalt (Co radiation wavelength Kα_1 = 1.7889 Å) and, after an XRD instrument replacement in the laboratory, a Bruker-D8-Advance-ECO X-ray Diffractometer with a Cu-Kα X-rays source, i.e. based on copper (Cu radiation wavelength of Kα_1 = 1.5406 Å). In both cases, the experimental setup consists of a X-rays source, whose X-rays are first collimated, then sent to a polarizing grating and finally to a diffraction slit to ensure a parallel and unidirectional field of X-rays striking the PVK thin-film surface [109]. A motorised varied-divergence slit enables to increase the size of the beam hitting the thin-film in order to reduce the typical loss of signal intensity at higher diffraction angles, which is a consequence of scattering. These XRD diffractometers present a Bragg-Brentano geometry configuration (Fig. 3.12), where the optical pathway of X-rays in the crystal $d_{hkl}\sin\theta$, generated by elastic scattering from the atomic plane underneath the surface of the thin-film, is doubled. This is the reason why in Eq. (27) $2d_{hkl}\sin\theta$ appears

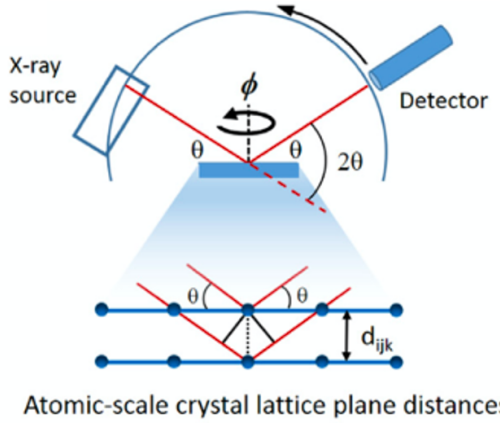

Figure 3.12: Illustration of the Bragg-Brentano geometry for XRD experiments and schematic representation of the Bragg diffraction that takes place as a consequence of the interaction between the X-rays and the crystal lattice atomic planes [110].

[110]. This setup offers the possibility of varying the diffraction measurement for different directions and thus angles by using a position sensitive detector (Lynxeye-XE-T), changing the position of the detector for a range of θ angles. As a result, the diffractometer produces diffractograms characterised by peaks with certain intensities, positions 2θ and features, which can be associated with Miller indices triplets and analysed to individuate the crystal structure properties of the PVK under investigation [110]. The measurements have been carried out with fixed sample illumination for a range of angles 2θ=5°-60°, step size of 0.01° and a measuring time of 0.01 s/step. Data evaluation has been performed via Bruker DiffracSuite.EVA V5.1 and V6.0 softwares.

The positions of the peaks at the various angles 2θ allow to identify the set of Miller indices associated with the interplanar distances in the crystal lattice and thus they can be used to understand the characteristic of the PVK under investigation looking at its internal crystal structure and symmetry. Moreover, by carefully analysing the diffraction intensities, positions and features of the peaks in the XRD diffractogram, it is possible to identify the different crystalline phases of a specific PVK and obtain information about PVK phase transformations, which can be induced by changes of composition, temperature or light. On top of that, the peaks intensity, but mostly their shift and shape, contain also information about the local disorder, distorsions due to stresses and strains and crystallite size. Lastly, in the case of polycrystalline textured PVK thin-films, it is also possible to observe the preferential crystallite orientations [110].

3.5.4. Scanning Electron Microscopy (SEM)

Scanning electron microscopy (SEM) is a characterization technique based on the use of a focused electron beam for imaging and analysing materials. It allows to obtain information about the surface topography, phase differences, crystallography and, in case of advanced SEM techniques, the atomic composition of the PVK thin-film under investigation [109, 116].

The SEM used for this MSc Thesis report measurement is a Jeol-JSM 6010LA SEM. Generally, a SEM instrument consists of several parts, as it can be seen schematically in Fig. 3.13 [109].

The electron source and the electron optical system, consisting in the condenser lens, objective lens and deflector for focusing electrons, generate a focused electron beam which act as the probe for scanning [109].

The electron source is made of tungsten [117]. The condenser and objective lenses allow to focus the primary electron beam made of high energy electrons (E~5-20 kV for this MSc Thesis Project measurements) to obtain a small probe with high luminance. The deflector modifies the electron probe position to scan the PVK thin-film, which is placed inside a chamber on a stage that can be moved along the x- and y-axes, rotated or tilted. An evacuation system maintains the column containing the electron optical system and the chamber in low vacuum. It has to be taken into account that some PVK thin-films may degrade under electron bombardment [109, 116].

When the beam strikes the thin-film surface, the interaction between the incident electrons and the atoms in the PVK generates various signals, which originate at different depths with respect to the material surface in the so-called interaction volume (Fig. 3.14) as a result of the emission of different electrons and X-rays characterised by distinctive energies (Fig. 3.15). With regards to the SEM used for the measurements of this MSc Thesis report, it is possible to distinguish secondary electrons (SEs), backscattered electrons (BSEs),

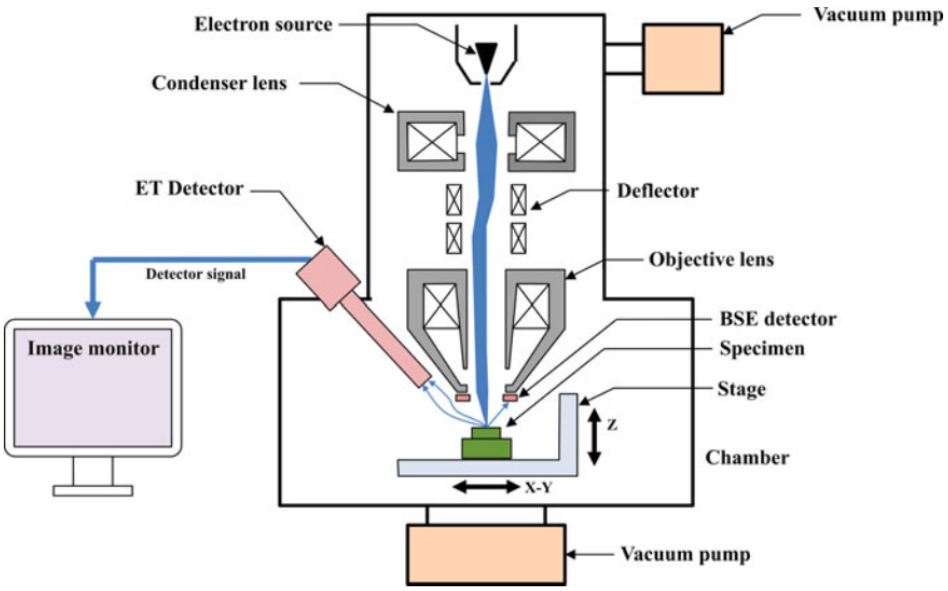

Figure 3.13: Schematic of the scanning electron microscope showing its main components [109].

characteristic X-ray (EDX), continuum (or Bremsstrahlung) X-rays and cathodoluminescence (CL) signals [109, 118].

Therefore, several detectors are used for detecting the different signals generated by the material surface. SEs are detected by an Everhart–Thornley detector (E–T detector). This instrument make the SEs accelerate and collide with a scintillator at high-voltage, which converts them into light. The latter is amplified by a photomultiplier tube, which transfer the signal to the image control system. On the other side, BSEs are directly detected by a semiconductor (P–N junction type) detector (BSE detector) thanks to the generation of electron-hole pairs. These are then separated and collected as an image signal [109].

These detectors are connected to an image control system. Finally, the signals, which are synchronised with the scanning frequency of the electron probe, are processed to form a real time magnified image on the image monitor [109, 116].

The magnification of the SEM can be adjusted by keeping constant the size of the image, while increasing or decreasing the size of the specimen surface area which is being scanned by the probe. Thus, multiple sets of focusing optics for the various magnifications are not necessary, unlike conventional optical microscopy. In this MSc Thesis Project, SEM magnifications from 30x to 20000x and a spatial resolution of 5 nm at E=20 kV [117], which corresponds to an high surface sensitivity. It is also characterised by a very large depth of field, ranging from 1 mm at high magnifications up to several mm at low magnifications. In conclusion, the resulting image has a much higher magnification and a 300 times greater depth of field than in traditional optical microscopy for equivalent magnifications [116].

The different signals provide complementary information about the PVK thin-films. In detail, the ones resulting from the emission of SEs and BSEs allow to obtain information about the surface topography and the composition (material contrast) of the PVK thin-film under examination, respectively [109]. The SEs are detected by the detector as electrons with low energy ($E \leq 50$ eV), which originate at shallow depth underneath the material surface (~100 nm). As the SE yield is strongly dependent on the electron beam incident angle on the material surface, the amount of the generated SEs increases at the edge of the material surface features and the signal results brighter. This provides topographical information of the PVK thin-film [109]. On the other hand, BSEs are characterised by high energy ($E \geq 50$ eV) and their signal is created more in depth (~500 nm). The intensity of the BSE signal is a function of the atomic number of the elements present in the material, thus the resulting signal gives a contrast difference between the different materials. In this way, information about the composition and the phase differences of the PVK can be obtained [109]. Additionally, BSEs can penetrate deeper into the material than SEs and can therefore be used for analysing buried atoms beneath the PVK thin-film surface [116].

Furthermore, the quantitative analysis of the element distribution and concentration through the thin-film thickness and the study of the crystallography of the PVK can also be performed, as the SEM used in this

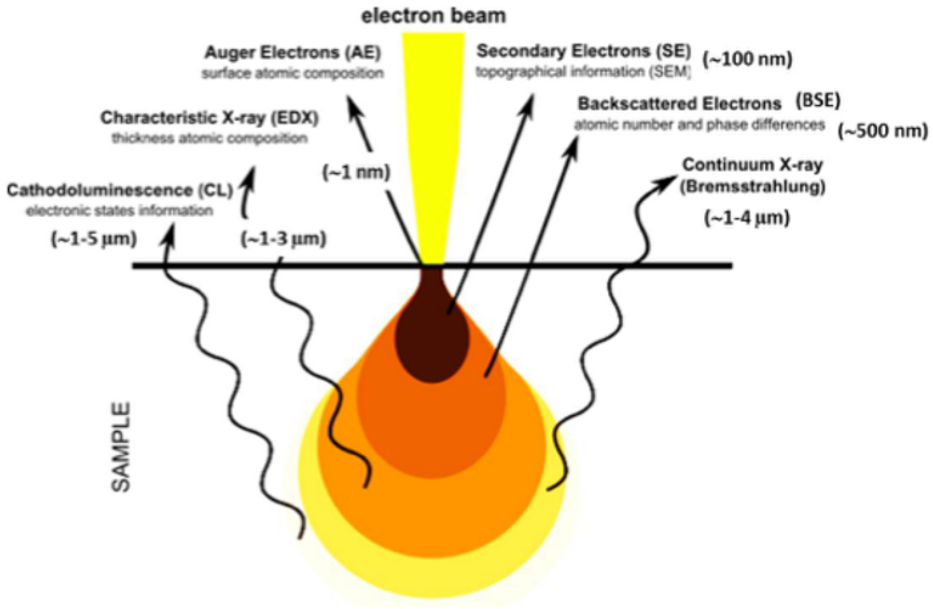

Figure 3.14: Representation of the interaction volume underneath the material surface showing the signals emitted at different depths, namely secondary electrons (SEs), backscattered electrons (BSEs), characteristic X-ray (EDX), continuum (or Bremsstrahlung) X-rays and cathodoluminescence (CL) [118].

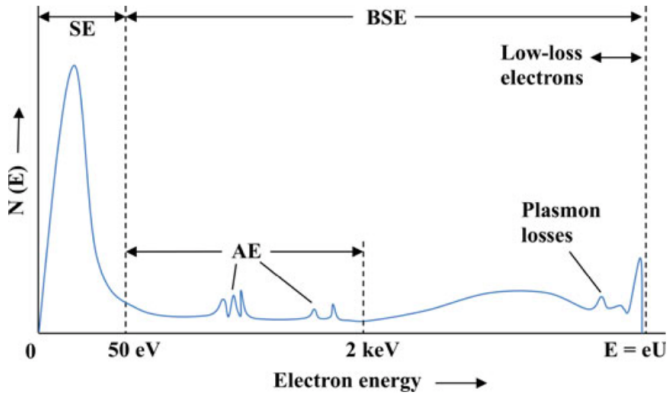

Figure 3.15: Schematic energy spectrum of emitted electrons during SEM analysis, showing secondary electrons (SEs) and backscattered electrons (BSEs). Plasmon losses are also observable. U is the energy of the electrons of the beam (primary electron energy) [109].

MSc Thesis Project is equipped with a fully-integrated energy-dispersive X-ray spectrometry (EDS or EDX) [117]. Regarding the EDS, it is a bulk characterization method which allows to analyse the composition of the PVK thin-film down to a depth of several μm from the surface. It takes into account the characteristic X-rays which are generated at ~1-3 μm of depth in the interaction volume. These X-rays have specific energies which depend on the atomic number. A SEM/EDS system analyses their signal to identify with high resolution the different elements present in the PVK thin-film [109].

As a final remark, it should be noted that the depth resolution, the elemental sensitivity and the accuracy depend on the energy of the primary electron beam, the analysis mode and the elemental composition of the PVK [116]. The depth resolution can range from tens of Å for the SEs signal to hundreds of nm for the BSEs signal to few μm for the EDS analysis [116]. The EDS technique is characterised by good elemental sensitivity and accuracy of 0.1% and 1-3%, respectively, but it has some limits in detecting low atomic number elements. With regards to the latter aspect, it is not sensitive to elements with an atomic number lower than that of carbon (C) and it has a limited sensitivity to elements lighter than sodium (Na) [116].

4

Thermally Evaporated $Cs_xFA_{1-x}PbI_{3-x}Br_x$ Thin-films Engineering

4.1. Processing Parameters - Current State

At the time of this MSc Thesis Project began, the current state of research in the laboratory was already featuring the initial optimisation of composition and bandgap of $Cs_xFA_{1-x}PbI_{3-x}Br_x$ thin-films. Considering the use of CsBr, FAI and PbI_2 as multications mixed-halide PVK precursors, the initial settings in terms of the main layer-by-layer multisource thermal evaporation processing parameters of this MSc Thesis Project are shown in Table 4.1 (see Section 3.1.1 for further details):

Table 4.1: Preliminary optimisation of layer-by-layer multisource thermal evaporation processing parameters.

Processing parameter	**CsBr**	**FAI**	**PbI_2**
Precursor molar ratio	0.25	0.85	1.1
Single layer thickness (nm)	1.1	6.3	8.2
Deposition rate (Å/s)	0.07	0.3	0.3
Source materials temperature	≥210 °C	≥93 °C	~369 °C

Starting from Eq. (28), the relation between the precursors molar ratio and the single layer thicknesses is expressed by Eq. (29):

$$m = \rho \cdot V \tag{28}$$

$$\frac{n_A}{n_B} = \frac{\rho_A M_B t_A}{\rho_B M_A t_B} \tag{29}$$

Where m is the mass, ρ the density, V the volume, n the moles, M the molar mass and t the thickness. The indices A and B refer to two different PVK precursors.

The layer-by-layer multisource thermal evaporation is conducted in manual mode. Eq. (29) shows the manner in which it is possible to apply control to a certain extent on the PVK composition during the layer-by-layer deposition. Nevertheless, the nominal precursors molar ratio 0.25:0.85:1.1 of CsBr, FAI and PbI_2 leads to a slightly different effective precursors molar ratio of the PVK thin-films, as not all the atoms and molecules of compounds fully react with each other during the deposition of the thin-film on the substrates inside the vacuum chamber. In particular, the resulting lower CsBr content in the real PVK thin-films with respect to the nominal molar ratio is the most important effect to which pay attention as it can widely influence the final PVK thin-films properties.

Furthermore, depending on the compound, the control on the source materials deposition rates though temperature is not trivial. The deposition rate of CsBr tends to stabilise easily after applying a specific temperature, while it is necessary to progressively increase the temperature of FAI and PbI_2 to maintain the set deposition rates during the deposition process.

As a final remark, it should be noted that in this initial stage of optimisation both the individual layers thicknesses and the deposition rates are kept small to ensure the reaction between the PVK precursors, envisioning a further optimisation in a later stage.

4.1.1. Targeted Perovskite Composition and Bandgap

This MSc Project thesis is based on multications mixed-halides PVKs of composition $Cs_xFA_{1-x}PbI_{3-x}Br_x$. The reasons behind the specific choice of the A, B and X constituents in the PVK ABX_3 crystal structure has been widely explained in Section 2.2 and Section 2.4.2.

The preliminary optimised PVK composition set as $Cs_{0.25}FA_{0.75}PbI_{2.75}Br_{0.25}$ results in an effective PVK thin-films composition of approximately $Cs_{0.19}FA_{0.71}PbI_{2.71}Br_{0.19}$. The resulting thin-films present a highly crystalline cubic α-PVK and a slight excess of PbI_2. In fact, it has been demonstrated that a 5% excess PbI_2 increases the performance of PSCs thanks to its GBs passivation ability, which reduces the the charge carriers recombination and improves the PVK stability against ambient air degradation [83, 89]. The Cs^+ content is within the range 0.10<x<0.30 [35], which gives PVKs characterised by a moisture-, oxygen- [50, 81] and thermally stable [119] α phase, high crystallinity, long charge-carrier lifetimes and high charge-carrier mobilities [35, 120], especially when x~0.17 [35, 119, 121]. The mixture of Cs^+ and FA^+ in order to respect such 1:4-1:5 molar ratio of Cs^+:FA^+ allows to obtain an optimum Goldschmidt tolerance factor ($t \rightarrow 1$) of the PVK crystal structure, determining a strong interaction between the A cations and the BX_6 inorganic octahedra network and thus high-quality crystallinity. This results in enhanced stability against PVK decomposition, alternative crystal phases transitions and photo-induced halide segregation [35, 81]. In addition to this, the fraction of Br^-, which is mixed with I^- in the X sites of the PVK to modify its bandgap (see Section 2.2.2), is really small. This Br^- content avoids the disruption of long-range crystalline order in spite of the difference in the ionic radii of the anions. Consequently, it prevents the formation of I^-- and Br^--rich phases and large trap state densities typical of Br^--rich films. In turn, the latter aspect favours a large charge carriers mobility, long lifetime and hinder recombination [35].

Concerning the bandgap tuning, as described in Section 2.2.2, if Cs^+ only marginally increases the bandgap, the main effect is given by the incorporation of Br^-, given that it is the main contributor of the VBM and CBM (Section 2.1.2). The addition of a fraction of Br^- equal to x~0.19 results in a slight blue-shift of the bandgap, which varies from a value of about E_g~1.52 eV (in case of $Cs_{0.17}FA_{0.83}PbI_3$) [35] to E_g~1.61 eV. Although this value is not comprised in the optimal range of values E_g~1.65-1.73 eV for the application of the related PSC as top cell in a 2-T PVK/Si tandem device, as explained in Section 2.3.2, the inclusion of just a modest amount of Br^- increases the bandgap as desired. This suggests the straightforwardness in modifying the optoelectronic properties of PVK and paving the way for the most diverse applications, including different types of multi-junction solar cells.

4.2. Process Optimisation

4.2.1. Annealing Temperature and Time

The optimisation of the temperature and annealing time is conducted by depositing several batches of PVK thin-films via thermal evaporation as described in Section 3.4.2, setting as processing parameters the ones derived from the optimisation described in Section 4.1.

The annealing optimisation procedure is divided in four main steps:

1. Test of different post-deposition annealing temperatures for a constant time (t_1) and comparison to the reference PVK thin-film without annealing;
2. For the maximum acceptable temperature before PVK degradation occurs (T_{deg}) found in (1), test for different annealing temperatures $T<T_{deg}$ for a constant annealing time (t_2), chosen such as $t_2>t_1$;
3. For the optimal annealing temperature (T_{opt}) found in (2), test for T_{opt} for different annealing times to individuate the optimal one (t_{opt});
4. Based on (1),(2) and (3), final test of best annealing temperature (T_{opt}) and time (t_{opt}).

For each deposition batch, the PVK thin-films properties are assessed, namely crystallinity and homogeneity, optical properties and bandgap, thickness and uniformity are assessed for each deposition batch. The charge transport properties are also briefly considered in the analysis in parallel to the characteristics of PVK thin-films.

1. Different Annealing Temperatures for a Constant Annealing Time

The first step is focused on testing different potential annealing temperatures, i.e. T=90, 120, 150 and 180 °C, applied for a short annealing time of t=8 min. Moreover, a PVK thin-film is left without annealing as a comparison.

The XRD diffractograms of the samples belonging to this first optimisation step are shown in Fig. 4.1.

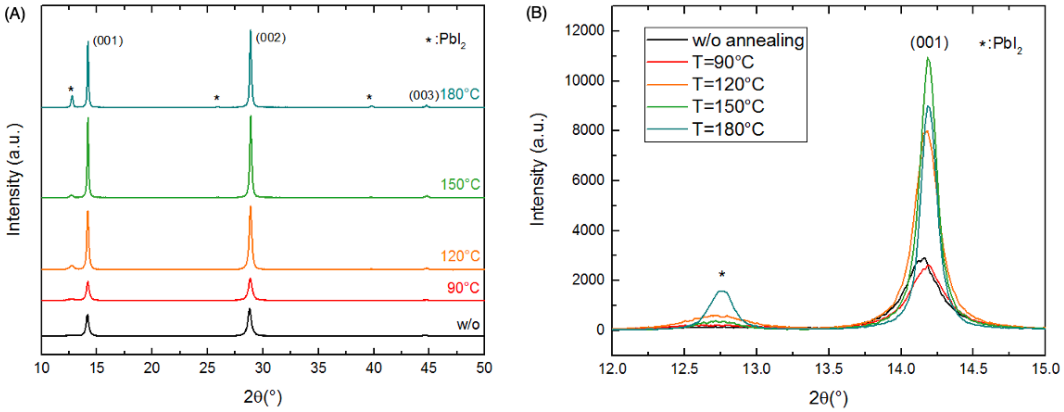

Figure 4.1: (A) XRD diffractograms and (B) zoom of the XRD (001) reflections for PbI_2 and α-PVK for $Cs_xFA_{1-x}PbI_{3-x}Br_x$ thin-films without annealing (w/o) and annealed at different temperatures between T=90 °C and T=180 °C for t=8 min.

All the samples present two main peaks and another less intense peak typical of the cubic α-PVK. The first XRD PVK peak is produced by the (001) family of lattice planes and it is usually located around 2θ=14.1°, while the second (002) peak is placed at about 2θ=28.3° and the third (003) peak is located at about 2θ=44.6° [19, 119, 122]. Furthermore, it is possible to observe the main (001) peak of PbI_2 at 2θ=12.7° and other less intense peaks [89, 123, 124].

In addition to the previous XRD patterns, the (001) PVK peak analysis is shown in Fig. 4.3. Comparing the PVK thin-film without annealing with the annealed ones, it is possible to notice a slight shift of the PVK peaks to larger angles, as shown by Fig. 4.3(A) for the (001) reflection. This is a consequence of the incorporation of Cs^+ and Br^- in the cubic α-PVK [48]. In fact, the presence of ions with smaller ionic radius, as in the case of Cs^+ and Br^- with respect to FA^+ and I^- (see Section 2.2.2) results in an enhanced close-packing of the atoms in the PVK crystal structure, which in turn leads to a smaller lattice constant and d_{hkl} spacing between the atomic planes. Recalling the Bragg's law introduced in Section 3.5.3, this produces a shift of the XRD peak towards higher 2θ angles.

The model shown in Fig. 4.2 relates the variation of the (001) XRD peak position of the cubic α-PVK to the Cs^+ content. It is helpful for roughly estimating the final composition of thermally evaporated PVK thin-films from the XRD diffractograms, so that the Cs^+ content (equal to the Br^- content due to thermal evaporation of CsBr during the synthesis process) can be put in relation with the observed structural and optical properties [89].

On top of that, the (001) PVK peak intensity and FWMH are shown in Fig. 4.3(B). Overall, an increase in crystallinity (XRD peaks intensity) can be noticed with increasing temperature, with the exception of the PVK thin-film annealed at T=180 °C whose XRD peaks are slightly lower than for the sample annealed at T=150 °C. The reason behind this trend will be explained in the herein Section 4.2.1.

The FWMH of the (001) reflection of PVK can be used to reveal indication on the average grain size according to the Scherrer equation, shown in Eq. (30) [125]:

$$D = \frac{k\lambda}{\beta cos\theta} \tag{30}$$

Where D is the average crystallite size λ is the wavelength of the radiation of Cu-Kα X-rays (Section 3.5.3), k is a shape factor equal to 0.94, β is the FWMH and θ the peak position [125]. The Scherrer equation shows that broadening of the widhts of the XRD peaks is inversely proportional to the level of disorder in the crystal structure (defects and lattice microstresses/microstrains) and mean crystallite size in the PVK thin-films [35, 83, 126]. This is a very useful information as the aim is to obtain large grains, since they are generally considered as beneficial for the charge transport properties and the resistance to degradation of PVKs, even though the precise role of GBs is still debated as explained in Section 2.1.3.

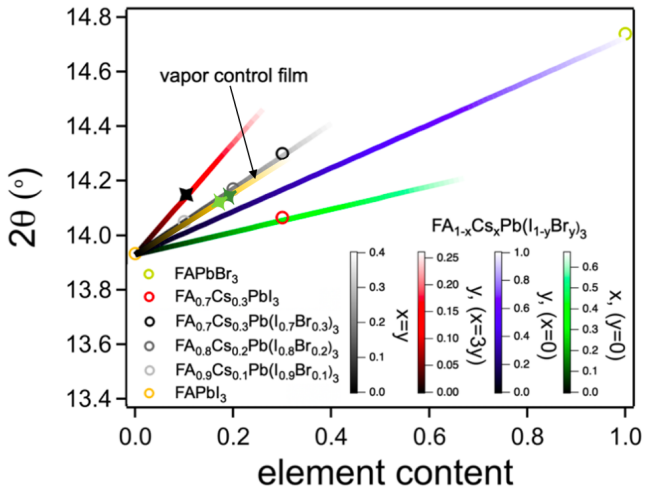

Figure 4.2: Model showing the variation in the position of the (001) XRD peak for cubic α-PVK as a function of the Cs^+ content to evaluate the final $FA_{1-x}Cs_xPb(I_{1-y}Br_y)_3$ composition of PVK thin-films. The yellow line shows this relationship in the case x=3y for thermally evaporated PVKs of this MSc Thesis Project, by assuming that the Cs:Br ratio is kept to 1:1, which is in line with the use of CsBr as source material. The light green and dark green star points lying on this line marks a PVK with final composition $FA_{0.83}Cs_{0.17}Pb(I_{0.83}Br_{0.17})_3$ and $FA_{0.81}Cs_{0.19}Pb(I_{0.81}Br_{0.19})_3$, respectively. Adapted from [89].

As it can be seen in Fig. 4.3(C), the average crystallite size increases increases with increasing annealing temperature. Furthermore, it is noteworthy that the as-deposited thin-film (without annealing) presents an average grain size D<100nm (more precisely ~25 nm), which shows the small grains which typically form in PVK thin-films synthesised by thermal evaporation. Interestingly, the average grain size is approximately doubled upon annealing (~50 nm). The same trend has been found in literature for thermally evaporated PVKs of similar FAI-poor (which implies a small amount of residual PbI_2, as for the PVK thin-films shown in this MSc Thesis Project) and stoichiometric composition [48].

In light of the optimisation, the sample without annealing is discarded due to the low level of crystallinity and small-scale grains. Additionally, the slight asymmetry of the peak visible in Fig. 4.1(B) as a pronounced shoulder at lower 2θ for the black XRD diffractogram, can be attributed to $FAPbI_3$-rich domains [89], which suggests the uncomplete reaction between the PVK precursors in as-deposited thin-films without annealing. On the other side, an excessively high annealing temperature (T≥180 °C) translates into more intense PbI_2 peaks and smaller PVK peaks, which is a symptom of PVK thermal degradation initiation. This is also confirmed by the formation of pinholes on the surface of the PVK thin-films annealed at T=180 °C for t= 8 min. The degradation phenomena affecting the thermally evaporated PVK thin-films of this MSc Thesis Project will be further explained in Section 4.3.

The best-performing PVK thin-films show high and narrow peaks of the cubic α phase PVK, corresponding to high-quality crystallinity and homogeneity (as no other crystal phases have been detected). Moreover, a low intensity peak of PbI_2 is expected as a consequence of composition. Lastly, bigger grains are preferred. As a conclusion, the best PVK thin-film is the one annealed at T=150 °C for t=8 min.

The optical properties and the bandgap values of the PVK thin-films are shown in Fig. 4.4.

The PVK thin-film without annealing show a lower absorptance for all the wavelengths, whereas all the other PVK thin-films present a good absorptance profile (Fig. 4.4(A)), showing higher absorption (A~70-80%) for $\lambda \lesssim$520 nm (blue light) and lower absorption for $\lambda \gtrsim$520 nm (from green to red light) which is desirable for a 2-T PVK/Si tandem application. In fact, in this way the PVK-based top cell harvests the more energetic photons of the blue light portion of the solar spectrum, while being transparent to the rest of the less energetic photons the that can be absorbed by the c-Si-based bottom cell. Moreover, the highly crystalline PVK thin-film are also presenting the highest reflectance. Its value is always below the 40% and it gets lower for the wavelength range 520 nm$\lesssim \lambda \lesssim$750 nm associated with the c-Si-based solar cell absorption (Fig. 4.4(B)).

By looking at the variation of the bandgap as a function of the annealing temperature of the samples in Fig. 4.4(C), the PVK-thin film showing the best crystallinity and homogeneity features (Fig. 4.1) annealed at T=150 °C presents a bandgap of E_g~1.61 eV, expected for a PVK of composition $Cs_{0.19}FA_{0.81}PbI_{2.81}Br_{0.19}$ (Fig. 4.2), like the one of this MSc Thesis Project. The sample without annealing not only shows smaller absorption, but also a dull absorption onset and a smaller bandgap due to, respectively, the lower crystallinity,

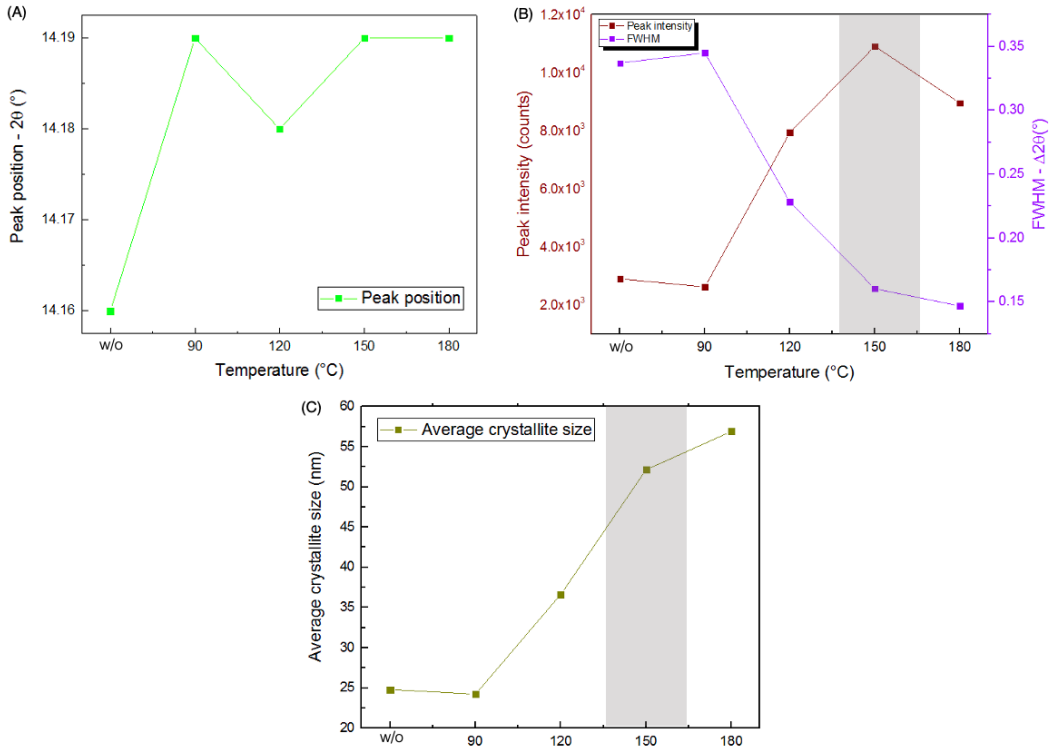

Figure 4.3: (A) Position, (B) intensity and FWMH of the (001) peak of cubic α phase PVK and (C) average crystallite size calculated in relation to the (001) peak for cubic α phase PVK as a function of the annealing treatment temperature for $Cs_xFA_{1-x}PbI_{3-x}Br_x$ thin-films without annealing (w/o) and annealed at different temperatures between T=90 °C and T=180 °C for t=8 min. The gray shaded region mark the optimum range of values to obtain high-quality PVK thin-films.

leading to the presence of less α-PVK which is the photoactive material, and to the incomplete incorporation of Cs^+ and Br^- in the PVK crystal structure. On the other hand, the thermally degraded sample annealed at T=180 °C presents a high absorption but a smaller bandgap (E_g~1.59 eV) compared to the others which may be a consequence of the start of the PVK decomposition into PbI_2 [83] (see Section 2.4.1).

On top of that, the expected thickness of the samples can be calculated taking into account that the determining factor is the thickness of the PbI_2 layer, the number of layers and the tooling factor associated with the specific thermally evaporated PVK of this MSc Thesis Project. The CsBr and FAI much thinner layers primarily react by interdiffusion with the PbI_2 layer already during the deposition itself [127, 128], thus they do not have a big influence on the final thickness of the PVK thin-film. The equation for the estimation of the thickness is shown in Eq. (31):

$$t_{PVK} = t_{PbI_2} \cdot N \cdot TF + 5 \qquad (nm) \tag{31}$$

Where t_{PVK} is the final thickness of the PVK thin-film, t_{PbI_2} is the thickness of the individually evaporated layer of PbI_2, N is the total number of deposited PbI_2 layers (number of stacks) and TF is the tooling factor of the so-obtained PVK thin fims. The final 5 nm of PbI_2 evaporated at the end of the deposition act as capping layer to protect the underneath layers of PVK precursors that may not have fully reacted. Considering the thermal evaporation parameters a TF~0.653 of the resulting PVK, the estimated thickness of a PVK thin-film is around t_{PVK}~112 nm.

The average thicknesses of the PVK thin-films is shown in Table 4.2. These fluctuating values around t_{PVK}100-120 nm are close to what is predicted by theoretical calculations. Acceptable variations of thickness can be observed both in the single samples (±2-12% thickness variation) and demonstrate the typical surface uniformity of thermally evaporated PVK thin-films and the samples belonging to the same deposition batch ((±2-26% thickness variation). The thickness shows bigger changes from one deposition batch to the other, as it can be seen from the PVK thin-film annealed at T=180 °C coming from a subsequent deposition. This may be due to chemico-physical modifications of the source materials after subsequent thermal evaporations which are affecting the deposition behaviour, but the level of reproducibility of thermally evaporated PVK

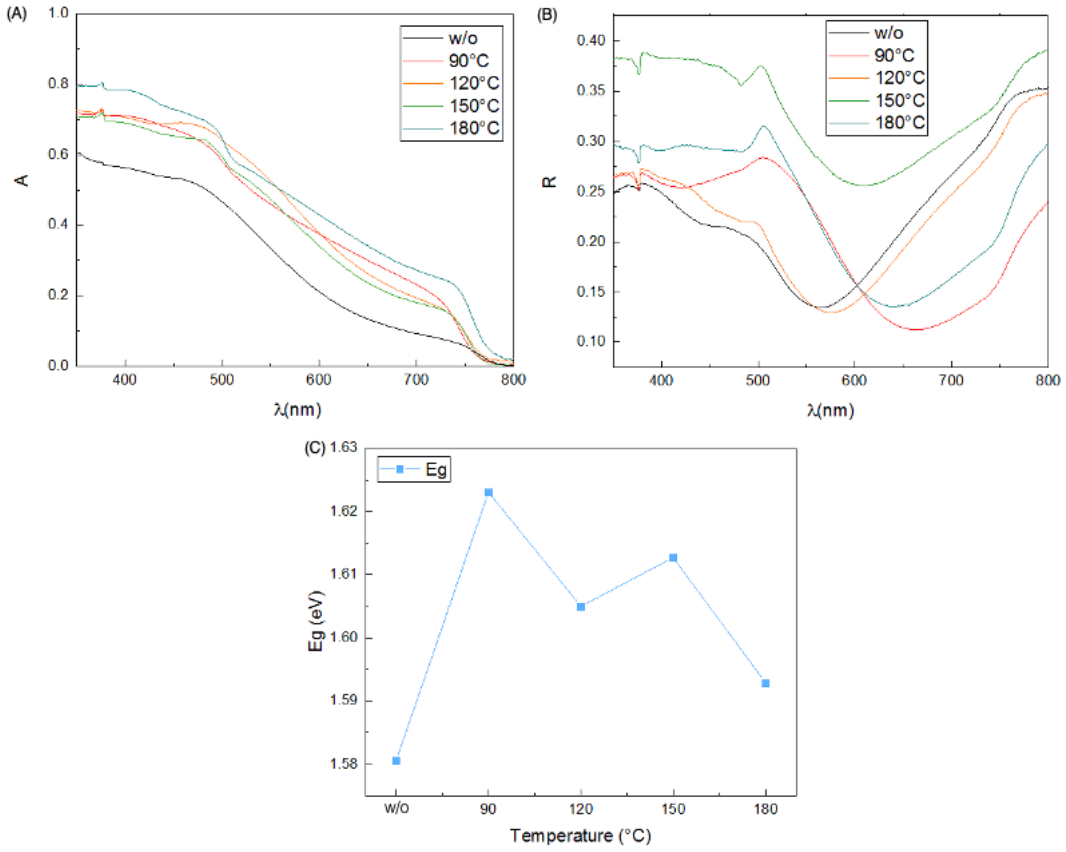

Figure 4.4: UV-Vis-NIR spectra showing (A) the absorptance and (B) the reflectance and (C) bandgap as a function of temperature, calculated from the absorptance spectra, for $Cs_xFA_{1-x}PbI_{3-x}Br_x$ thin-films without annealing (w/o) and annealed at different temperatures between T=90 °C and T=180 °C for t=8 min.

thin-films is overall still good.

Lastly, the PVK thin-films absorption spectra can be related to their thicknesses, presented in Table 4.2. It is worth mentioning that, taking into account the small thickness of the samples, the absorption can be considered more than modest. It may be state that a further increase of the thickness would probably lead to even better results in terms of optical properties. Apart from that, it should be underlined that the higher absorptance of the PVK thin-film annealed at T=180 °C that was observed in Fig. 4.4(A) is probably due to the fact that the sample is thicker than the others. This further supports the finding that the best PVK thin-film is the one annealed at T=150 °C for t=8 min, as it is characterised by one of the highest absorption despite being the thinnest layer.

Table 4.2: Thickness measurements for $Cs_xFA_{1-x}PbI_{3-x}Br_x$ thin-films without annealing (w/o) and annealed at different temperatures between T=90 °C and T=180 °C for t=8 min. The columns "Average thickness 1" and "Average thickness 2" refer to the measurements performed across the scratch 1 and scratch 2 engraved on the thin-film, respectively.

Sample	**Average thickness 1 (nm)**	**Average thickness 2 (nm)**	**Average thickness (nm)**
w/o	103.22	97.60	100.41
90 °C	121.35	112.78	117.07
120 °C	106.02	94.53	100.28
150 °C	96.01	97.84	93.93
180 °C	123.68	128.06	125.87

In conclusion, PVK thin-films without annealing do not show good properties and thermal degradation initiates for T≥180 °C. Thus, annealing temperatures T<150 °C for a short annealing time will be analysed in the next optimisation step.

2. Annealing Temperatures averting Thermal Degradation for a Constant Annealing Time

The second optimisation step pays attention to investigate different low annealing temperatures T<150 °C, i.e. T=100, 110 and 120 °C for a long annealing time of t= 30 min. The so-obtained PVK thin-films are then compared to the sample annealed at T=150 °C for t= 8 min from the previous optimisation step.

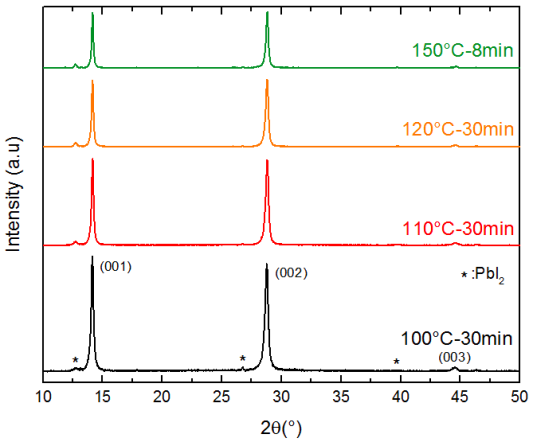

Figure 4.5: XRD diffractograms for $Cs_xFA_{1-x}PbI_{3-x}Br_x$ PVK thin-films annealed at temperatures T<150 °C and long times, i.e. T=100 °C, 110 °C and 120 °C for t=30 min, compared with a PVK thin-film annealed at T=150 °C for t=8 min.

The XRD diffractograms of the samples belonging to this second optimisation step are shown in Fig. 4.5. By observing it, it is possible to notice again the typical XRD peaks of the cubic α-PVK and the ones of PbI_2 due to its excess content in the PVK composition. In contrast to the previous case, it is noteworthy the decrease in crystallinity with increasing temperature given by the decrease in the XRD peaks intensity. The change in the response of the material as a function of temperature might be a consequence of the longer annealing times applied in this second optimisation step.

The (001) PVK peak analysis of the different PVK thin-films is presented in Fig. 4.6. In spite of the almost constant (001) PVK peak location, suggesting PVK thin-films of the same composition coming from the same deposition batch, a small variation of the (001) PVK peak position with respect to the first optimisation step samples can be observed (Fig. 4.6(A)), which might indicate the presence of less Cs^+ and Br^- in the PVK thin-films. Furthermore, as it can be seen from Fig. 4.6(B), the decrease in the intensity of the (001) reflection of PVK shows the decrease in crystallinity with increasing temperature. In contrast to the previous optimisation step, the increase in crystallinity related to the absolute intensity of the peak is not parallel to the peak sharpening and narrowing. In fact, the FWHM of the (001) PVK peak follows the same trend of its intensity as a function of temperature. Thus, as shown by Fig. 4.6(C), the smallest average crystallite size corresponds to the PVK thin-film annealed at T=120 °C for t=30 min, but the grains are even smaller for the sample annealed at T=150 °C for t=8 min.

It is important to highlight the difference between the absolute intensity (Fig. 4.6(B) in dark red) and integral intensity, i.e. the area, of an XRD peak. The area of the XRD peak generated by a particular crystal structure is associated with the fraction of the crystal phase itself [126]. The difference in both the absolute and integrated intensity (see Fig. 4.5 and Fig. 4.6(B)) among the PVK thin-films, thus in the fraction of photoactive PVK cystal phase, is more remarkable than the variation in the FWHM (Fig. 4.6(B)), crystal defects and crystallite size (ΔD ~13 nm or less, as shown in Fig. 4.6(C)). Hence, the amount of reflections from the PVK crystal phase (absolute intensity) and crystalline phase (integrated intensity) are chosen as discriminating factors for the optimisation. Consequently, the optimum is set for the PVK thin-film annealed at T=100 °C for t=30 min among all the PVK thin-films under investigation. This shows the highest (001) PVK peak intensity and larger area, thus the biggest fraction of PVK crystal phase harvesting solar energy and generating charge carriers, although being characterised by the highest FWHW and smallest average grain size. In addition to this argument, the fact that the average grain size is not the only parameter affecting the charge transport properties and the role of GBs is still debated (see Section 2.1.3) is also taken into account.

On the other side, the PVK thin-film annealed at T=150 °C for t=8 min shows the largest average crystallite size. However, the lower intensity PVK peaks in combination with the surface irregularities which have emerged after the thermal treatment leads to its exclusion (see Section 4.3).

Interestingly, in comparison with the behaviour shown by the PVK thin-films of the first optimisation step,

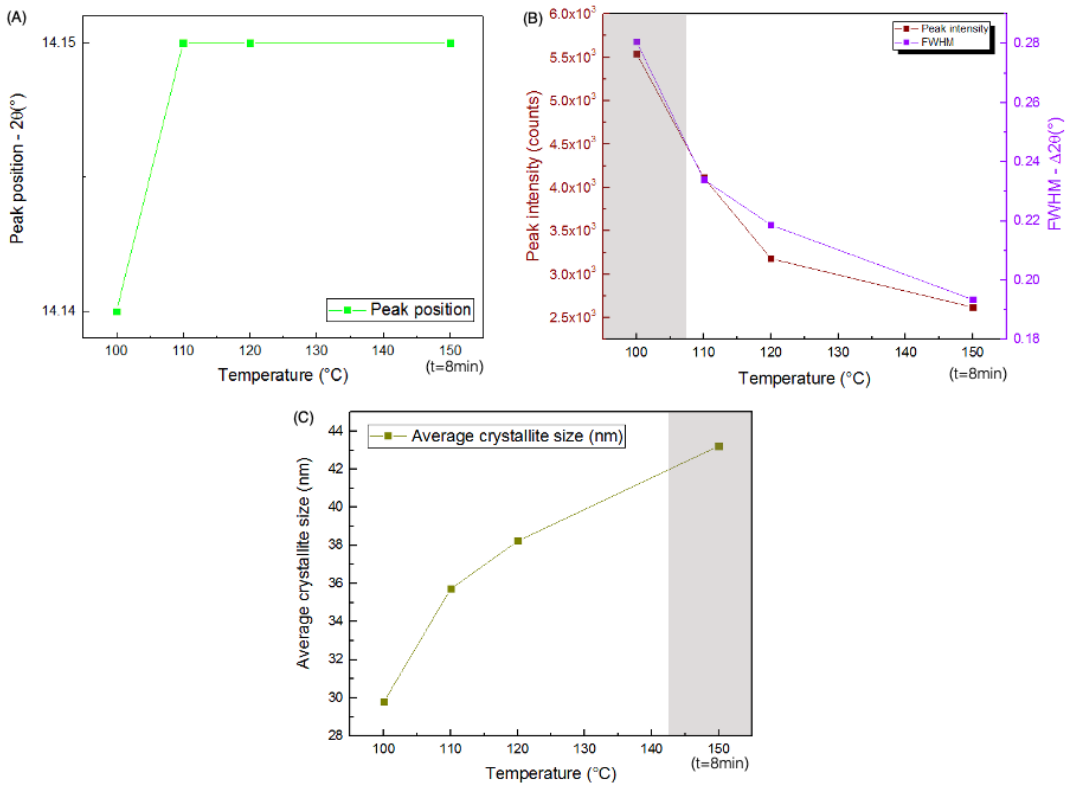

Figure 4.6: (A) Position, (B) intensity and FWMH of the (001) peak of cubic α phase PVK and (C) average crystallite size calculated in relation to the (001) peak for cubic α phase PVK as a function of the annealing temperature for $Cs_xFA_{1-x}PbI_{3-x}Br_x$ PVK thin-films annealed at different temperatures between T=100 °C and T=120 °C for t=30 min, compared with a PVK thin-film annealed at T=150 °C for t=8 min. The gray shaded region are marking the optimum range of values for obtaining high-quality PVK thin-films.

it may be noted that the growth of the grains looks more influenced by applying a certain temperature to the sample rather than prolonging the annealing time. In fact, in the first case the average grain size of D~25 nm approximately doubles upon annealing reaching D>50 nm, while in the second case the grain size seems to increase less than before. This may be due to composition variations affecting the response of the PVK thin-films to the annealing treatment [48]. It has also to be taken into account that the grain growth is a thermally activated diffusion process.

The average grain size depends on the temperature and time as expressed by Eq. (32) [129]:

$$D = kt^{n} \tag{32}$$

Where D is the average grain size at a certain time, k is a temperature dependent constant, t is the time and n is the grain growth exponent, whose ideal value is 0.5. The temperature dependent constant k is shown in Eq. (33):

$$k = k_0 exp\left(\frac{-E_A}{RT}\right) \tag{33}$$

Where k_0 is the rate constant, E_A is the activation energy for grain boundary mobility, R is the universal gas constant and T is the absolute temperature [129].

Since the grain growth rate varies directly with temperature, it follows that the crystallisation of PVK thin-films improves with increasing temperature and the grain growth exponent increases accordingly. Therefore, it can be speculated that a higher annealing temperature more effectively promotes grain growth, approaching n=0.5, than extending the annealing time. However, further experiments and measurements are needed to support this conjecture [129].

Then, the optical properties measurements and the bandgap values of the PVK thin-films annealed at low temperatures for a long time can be observed in Fig. 4.7. It can be noticed in Fig. 4.7(A) a less sharp absorption onset and a lower absorption (A≤60%) for the whole wavelength range under investigation than in the case

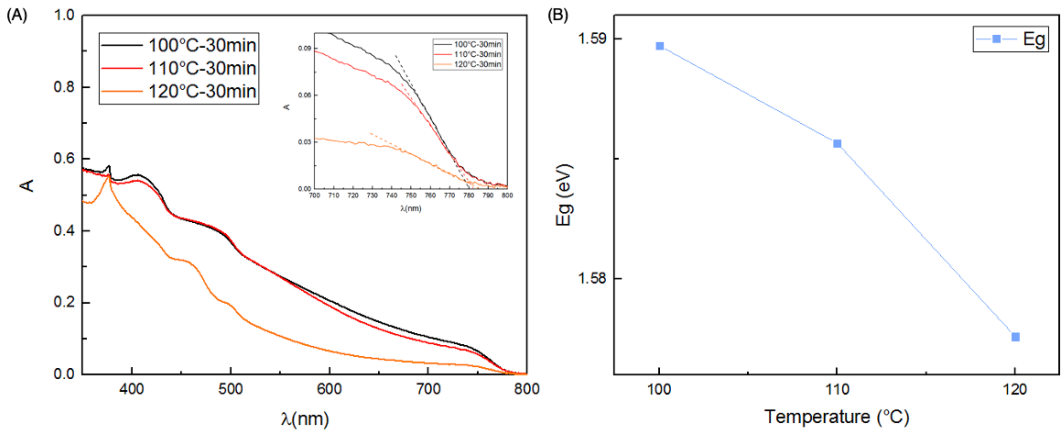

Figure 4.7: (A) UV-Vis-NIR absorptance spectra and (B) bandgap as a function of temperature for PVK, calculated from the absorptance spectra, for $Cs_xFA_{1-x}PbI_{3-x}Br_x$ thin-films annealed at different temperatures between T=100 °C and T=120 °C for t=30 min. The inset in (A) offers a close look on the absorption onsets. It is possible to observe the linear portion of the absorptance spectra and its intercept with the x-axis, related to the bandgap.

of the PVK thin-films of the previous optimisation step. Moreover, as illustrated in Fig. 4.7(B), the bandgap is even smaller than the one of the previous samples and it decreases with increasing temperature. For instance, the bandgap of the best sample selected after the crystallinity and homogeneity analysis annealed at T=100 °C for t=30 min is E_g~1.59 eV. By taking into account that this bandgap should correspond to a PVK of approximately composition $Cs_{0.15}FA_{0.75}PbI_{2.85}Br_{0.15}$ (Fig. 4.2), the shift towards lower 2θ angles of the (001) reflection of PVK more precisely around 2θ=14.15° (Fig. 4.6(A)) and the overall lower absorption, it seems that CsBr is not fully incorporated in the PVK crystal structure during thermal evaporation despite the application of the same processing parameters. This hypothesis is corroborated by the degradation of the PVK thin-film annealed at T=120 °C for t=30 min taking place in ambient air, which is confirmed by the decline of the absorptance and smoothing of the absorption onset visible in Fig. 4.7(A). In fact, the lack of Cs^+ might be the major cause of the instability of the PVK crystal structure in presence of the moisture and oxygen in ambient air and its decomposition in PbI_2. As a proof, the sample turns yellow when brought out of the glove box for less than 5 min. The degradation phenomena and their causes will be explained in more details in Section 4.3.

Lastly, the thickness measurements can be seen in Table 4.3). They show that the PVK thin-films are characterised by acceptable thickness deviation from the expected values and tolerable variation in the same sample and from one sample to the other. As these results are similar to those of the first optimisation step, this further supports the idea that the low absorption of the PVK thin-films of the second optimisation step seems to derive from problems in the CsBr incorporation reaction during the thermal evaporation process itself and and not a consequence of a difference in thickness.

Table 4.3: Thickness measurements for $Cs_xFA_{1-x}PbI_{3-x}Br_x$ thin-films annealed at different temperatures between T=100 °C and T=120 °C for t=30 min. The columns "Average thickness 1" and "Average thickness 2" refer to the measurements performed across the scratch 1 and scratch 2 engraved on the thin-film, respectively.

Sample	Average thickness 1 (nm)	Average thickness 2 (nm)	Average thickness (nm)
100 °C	121.05	116.54	118.79
110 °C	109.64	106.12	107.88
120 °C	97.98	105.58	101.78

To conclude, the best-performing PVK thin film is the one annealed at T=100 °C for t=30 min and thereby the temperature T=100 °C is chosen as best temperature for the annealing thermal treatment. In the next optimisation step, T=100 °C and different annealing times will be investigated as annealing parameters.

3. Best Annealing Temperature and Different Annealing Times

The third optimisation step studies T=100 °C as annealing temperature for different annealing times. Two deposition batches of PVK thin-films are produced to find the best annealing time, namely:

i. For the first deposition batch the annealing temperature is fixed at T=100 °C while the annealing time varies between t=10 min and t=40 min.

ii. After individuating the optimal annealing time from (ii), i.e. t=30 min, another deposition batch of PVK thin-films is produced to investigate a range of annealing times close to t=30 min. Thus, for the second deposition batch the annealing temperature is still fixed at T=100 °C while the annealing time varies between t=25 min and t=35 min.

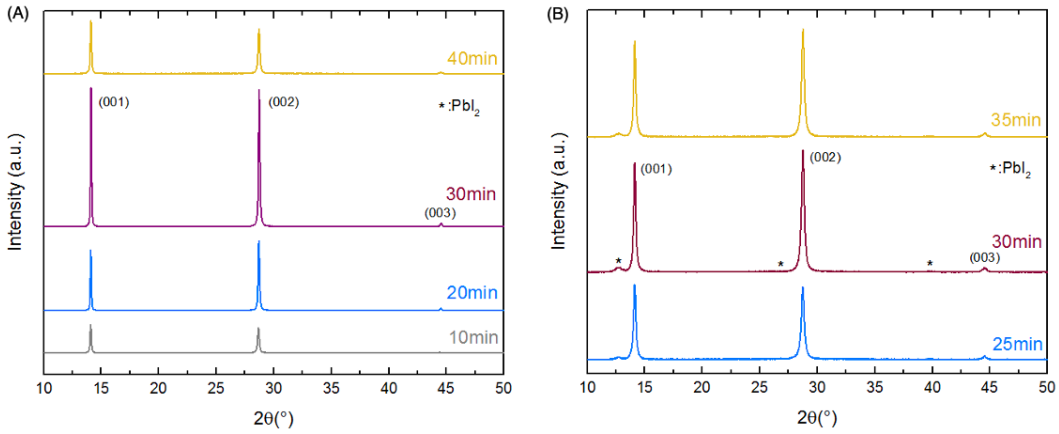

Figure 4.8: XRD diffractograms for $Cs_xFA_{1-x}PbI_{3-x}Br_x$ thin-films annealed at temperature T=100 °C for (A) t=10,20,30 and 40 min and (B) t=25,30 and 35 min.

The corresponding XRD diffractograms are shown in Fig. 4.8(A) and Fig. 4.8(B), respectively. In the deposition batch (i) (Fig. 4.8(A)) testing annealing times between t=10 and t=40 min, the cubic α-PVK XRD peaks can be observed, while the peaks originated by the excess of PbI_2 are not present anymore. The expected XRD PbI_2 peaks can instead be seen in the deposition batch (ii) for testing the annealing times between t=25 min and t=35 min (Fig. 4.8(B)). The absence of the peaks of PbI_2 is a phenomenon similar to the compositional variations that have been already mentioned in the herein Section 4.2.1 as an intrinsic limitation in the molar ratio control allowed by the layer-by-layer thermal evaporation process.

Nonetheless, the PVK thin-films of stoichiometric composition still present good crystallinity and homogeneity properties. More precisely, it is clearly visible from the XRD diffractograms of both deposition batches (i) and (ii) that the PVK thin-films showing the highest XRD peaks of PVK is the one annealed at T=100 °C for t=30 min.

The (001) PVK peak analysis is shown in Fig. 4.9. Focusing on the (001) PVK peak position analysis, an evident shift towards lower 2θ angles of the peak with respect to the previously described PVK thin-films can be noticed Fig. 4.9(A). This aspect, the absence of the PbI_2 peaks and the slightly darker colour of the related PVK thin-films suggests an excess of FAI. In fact, FA^+ is an organic cation with a big ionic radius (see Section 2.2.2) that induces a shift to the left of the XRD peaks of PVK. Thus, some deposition process problems in terms of composition control, maybe caused by the thermal deterioration of the PbI_2 powder used as thermally evaporated source material, probably has taken place during the first deposition (i). This aspect will be further developed in Section 4.3. Additionally, a left-shift, even though smaller with regards to the previous case, can also be seen for the PVK thin-films of the second deposition batch (ii) Fig. 4.9(C).

The PVK thin-films annealed at T=100 °C for t=30 min not only present a high level of crystallinity, but also the optimal combination of high absolute intensity and small FWHM of the (001) PVK reflection in both annealing time ranges considered, as indicated by the gray shaded areas in Fig. 4.9(C) and (D). Finally, this PVK thin-film also exhibits the largest (D~83 nm in Fig. 4.9(E)) or one of the largest (D~33 nm in Fig. 4.9(F)) average crystallite size among all the samples undergoing different annealing times of both deposition batches (i) and (ii). It is noteworthy that the PVK thin-films coming from the deposition batch (i) are characterised by a significantly large grain size with respect to all the previously analysed samples. This is a consequence of their composition, as it has been shown that FAI-rich PVK thin-films tend to even triple in grain size after annealing [48]. Conversely, the other FAI-poor (abundance of PbI_2) PVK thin-films of deposition batch (ii) with annealing parameters T=100 °C and t=25, 30 and 35 min show a fairly limited grain growth, as mentioned before in Section 4.2.1.

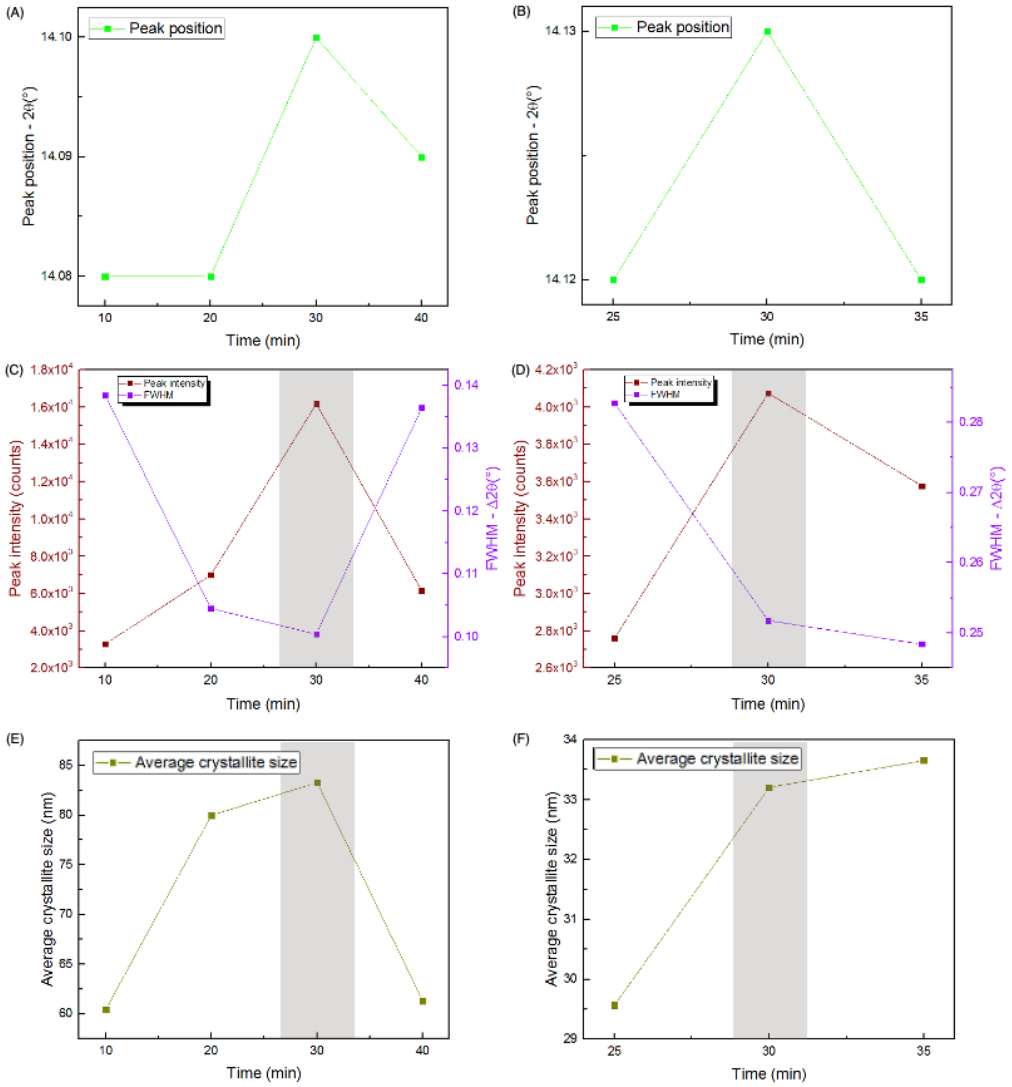

Figure 4.9: Position, intensity and FWMH of the peak of cubic α phase PVK and average crystallite size calculated in relation to the (001) peak for cubic α phase PVK as a function of the annealing time for $Cs_xFA_{1-x}PbI_{3-x}Br_x$ thin-films annealed at temperature T=100 °C for (A)-(C)-(E) t=10,20,30 and 40 min and (B)-(D)-(F) t=25,30 and 35 min, respectively. The gray shaded region are marking the optimum range of values for obtaining high-quality PVK thin-films.

The optical properties and bandgap values of the PVK thin-films are shown in Fig. 4.10. All the PVK thin-films of deposition (i) and (ii) show similar absorption to those of the second optimisation step shown in Section 4.2.1 (A≤60%). The main difference is that the samples of the deposition batch (i) present a sharper absorption onset (Fig. 4.10(A)) and a clearer between the high absorption region (A~60%) for $\lambda \lesssim 500$ nm and the low absorption one for $\lambda \gtrsim 500$ nm than those of the deposition batch (ii) (Fig. 4.10(B)). Therefore, it seems that, in spite of the FAI excess, a high-quality photoactive PVK crystal phase has formed during the thermal evaporation process. Additionally, CsBr has been properly incorporated into it, as confirmed by the bandgap of the PVK thin-film annealed at T=100 °C for t=30 min of E_g~1.61-1.62 eV visible in Fig. 4.10(C). This value is almost within the optimal range of bandgap values for 2-T PVK/Si tandem applications (see Section 2.3.2. This bandgap value is compatible with a PVK of composition $Cs_{0.19}FA_{0.81}PbI_{2.81}Br_{0.19}$ with a FAI excess. Moreover, this sample is also characterised by a good absorbance spectrum for a monolithic PVK/Si tandem application, featuring high absorption for short wavelengths and low absorption for long ones. However, the absorption onset is the least clear-cut of the related deposition batch.

On the other hand, the PVK thin-films of the deposition batch (ii) show a quite dull absorption onset, which may derive from a low-quality photoactive PVK crystal phase. This is evidenced by the lower absolute and integrated intensities and bigger FWHM of the (001) XRD peak of PVK which can be seen in Fig. 4.9(D),

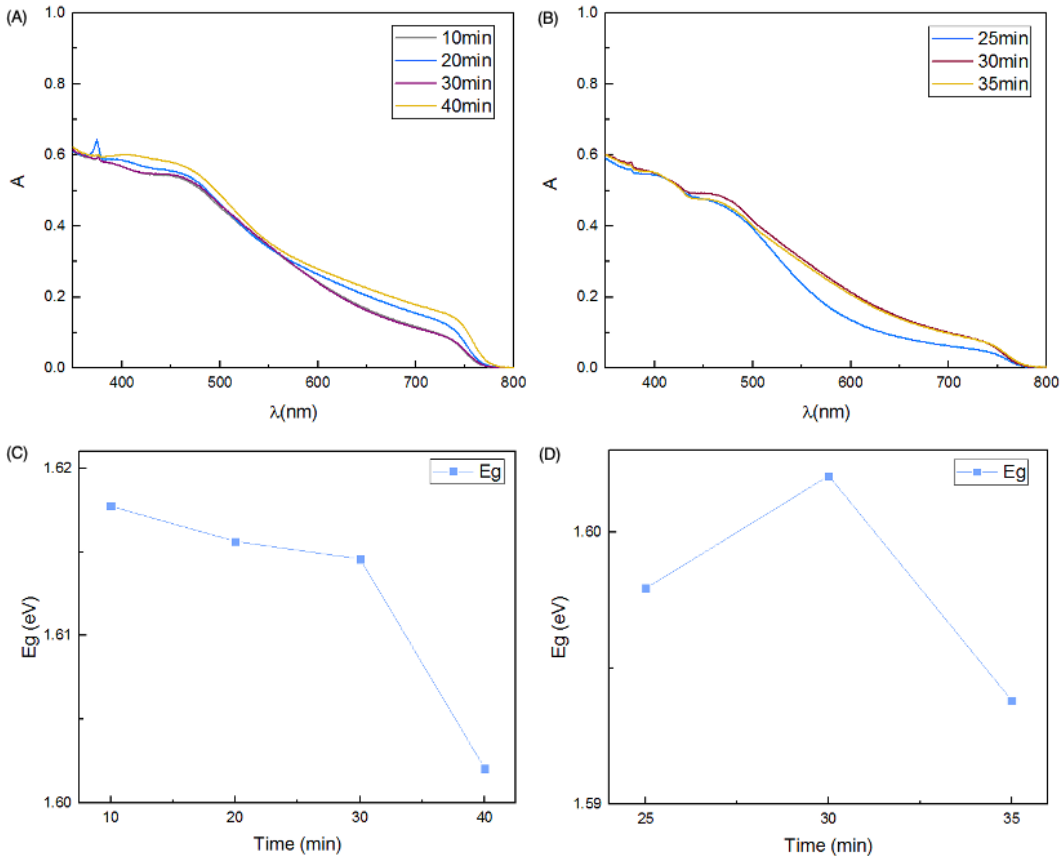

Figure 4.10: UV-Vis-NIR absorptance spectra and bandgap as a function of temperature for PVK, calculated from the absorptance spectra, for $Cs_xFA_{1-x}PbI_{3-x}Br_x$ thin-films annealed at temperature T=100 °C for (A)-(C) t=10,20,30 and 40 min and (B)-(D) t=25,30 and 35 min, respectively.

compared to the same values for the PVK thin-films coming from the deposition batch (i), visible in Fig. 4.9(C). Moreover, the PVK thin-film annealed at T=100 °C and t=25 min presents a lower absorption with respect to the other samples of the same deposition batch (ii), especially for $\lambda \gtrsim$500 nm. The poor absorption profiles of the PVK thin-films of the deposition batch (ii) can also be explained in light of the degradation that has affected them after exposure to ambient air for about 10-15 min. This seems a consequence of the failed incorporation of Cs^+ due to difficulties in depositing CsBr during the thermal evaporation process (see Section 4.3). Apart from that, it has to be highlighted that among the samples of the deposition (ii), the PVK thin-film annealed at T=100 °C for t=30 min is the most stable against degradation. In comparison with the analogue of deposition (i), this sample is characterised by a lower bandgap of E_g~1.60 eV, by considering also the (001) PVK peak position, an expected PVK composition $Cs_{0.15}FA_{0.85}PbI_{2.85}Br_{0.15}$.

Table 4.4: Thickness measurements for $Cs_xFA_{1-x}PbI_{3-x}Br_x$ thin-films annealed at temperature T=100 °C for t=10,20,30 and 40 min and t=25,30 and 35 min. The columns "Average thickness 1" and "Average thickness 2" refer to the measurements performed across the scratch 1 and scratch 2 engraved on the thin-film, respectively.

Sample	Average thickness 1 (nm)	Average thickness 2 (nm)	Average thickness (nm)
10 min	111.85	108.55	110.20
20 min	112.70	110.32	111.51
30 min	110.32	107.00	108.66
40 min	114.34	113.29	113.81
25 min	77.84	72.06	74.95
30 min	104.15	127.09	115.62
35 min	90.62	99.40	95.01

Last but not least, the thickness of the PVK thin-films of both deposition bateches (i) and (ii) are shown

in Table 4.4. These thickness values are within the expected range and show reasonable differences, with the exception of the thinner PVK thin-film annealed at T=100 °C and t=25 min of deposition batch (ii). This seems again the result of an apparently non-uniform evaporation that has caused a deficiency of Cs^+ and Br^- and thickness discrepancies between samples from the same deposition batch (ii), i.e. the one testing annealing treatments at T=100 °C for t=25, 30 and 35 min.

In conclusion, the PVK thin-film showing the best properties in terms of crystallinity, homogeneity, absorption and uniformity is that subjected to an annealing treatment at T=100 °C for t=30 min in both deposition batches (i) and (ii). The characteristics of the resulting PVK thin-films will be analysed more specifically in the last step of the optimisation process.

4. Best Annealing Temperature and Time

The fourth step of the optimisation process is based on a final deposition of PVK thin-films to confirm the finding regarding the best annealing parameters.

The XRD diffractogram of the optimised PVK thin-film annealed at T=100 °C and t=30 min can be seen in Fig. 4.11. The typical peaks of both the cubic α-PVK and PbI_2 are indicated. The sample is characterised by good phase homogeneity, as intense and narrow PVK peaks dominate the XRD pattern and no other crystal phases are present. Moreover, as mentioned in Section 4.1.1, the slight excess PbI_2 content induces the passivation of GBs helping to prevent charge-carrier recombination and degradation phenomena.

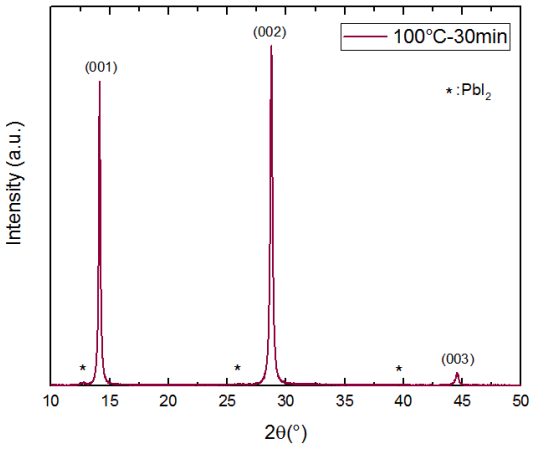

Figure 4.11: XRD diffractograms of $Cs_{0.15}FA_{0.85}PbI_{2.85}Br_{0.15}$ thin-films annealed at temperature T=100 °C for t=30 min.

Table 4.5: Position, intensity and FWMH of the peak of cubic α phase PVK and average crystallite size calculated in relation to the (001) peak for cubic α phase PVK of $Cs_{0.15}FA_{0.85}PbI_{2.85}Br_{0.15}$ thin-film annealed at temperature T=100 °C for t=30 min.

Property	
Peak position-2θ (°)	14.12
Peak intensity (counts)	8845
FWHM-$\Delta 2\theta$ (°)	0.19691
Average crystallite size (nm)	42.5

The properties deriving from the analysis of the (001) reflection of PVK are shown in Table 4.5. The left-shift of the peak with respect to that of the PVK thin-films of the first optimisation step (see Section 4.2.1) can still be noted. Thus, it can be assumed that a minor CsBr content is present in the PVK thin-film under research, although the analysis of the optical property is necessary to support this hypothesis. After studying the intensity and FWHM of the peak, the average crystallite size is calculated to be D~42.5 nm. This is in line with the moderate grain growth associated with FAI-poor PVK thin-films.

The optical properties of the optimised PVK thin-film are shown in Fig. 4.12. In this case the contribution to the absorption and reflection of the glass substrate has been taken into account. As the absorption of glass is close to A=0%, the absorptance spectrum of the PVK thin-film does not require any correction. The reflectance spectrum is instead corrected by subtracting the reflection of R~9-10% of the glass substrate (R_{corr}). The UV-Vis-NIR measurements of the glass substrates used in this MSc Thesis Project are shown in

Appendix A. The bandgap value of the optimised PVK thin-film, evaluated by three different methods, is presented in Table 4.6.

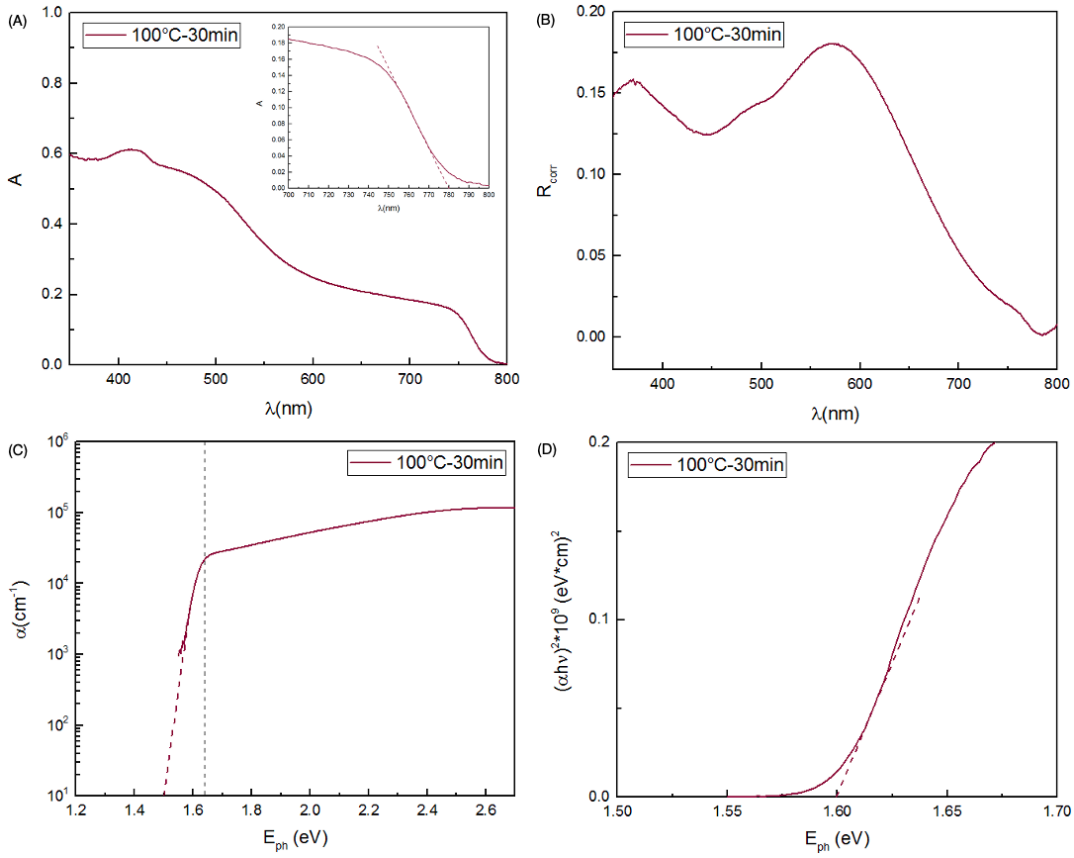

Figure 4.12: UV-Vis-NIR (A) absorptance, (B) reflectance spectra after glass substrate correction, (C) absorption coefficient as a function of the photon energy E_{ph} and (D) Tauc plot of $Cs_{0.15}FA_{0.85}PbI_{2.85}Br_{0.15}$ thin-film annealed at T=100 °C for t=30 min. The inset in (A) offers a close look on the absorption onsets. It is possible to observe the linear portion of the absorptance spectrum and its intercept with the x-axis, related to the bandgap. The absorptance spectrum has not been corrected by subtracting the absorption of the glass substrate as it is close to A=0%. The reflectance spectrum has been corrected considering the reflection of the glass substrate around R~9-10%. The purple dashed line in the absorption coefficient is a guide to the eye towards lower E_{ph}, while the thinner black dashed line underlines the division between the high and constant α and the beginning of its drop.

The modest absorptance of A≤60% for $\lambda \lesssim$500 nm, followed by a decrease to A~20% for $\lambda \gtrsim$600 nm shown in the absorptance spectrum in Fig. 4.12(A) shows similar absorption properties to those of the majority of the previous PVK thin-films analysed in the herein Section 4.2.1. On the other side, the reflectance spectrum in Fig. 4.12(B) shows a shift of the region of low reflection towards longer wavelengths $\lambda \gtrsim$600 nm (orange a red light) with regards to the PVK thin-films of the first optimisation step (see Section 4.2.1). This red-shift of the reflectance spectrum may derive from an increase in the PVK thin-film thickness, which will be confirmed later in the herein Section 4.2.1.

It is worth noting the presence in Fig. 4.12(A) of a rather sharp absorption onset, suggesting a high-quality photoactive cubic α-PVK phase. Such absorptance spectrum reveals a bandgap of E_g~1.59 eV as shown in Table 4.6, which may be related to a an PVK of composition $Cs_{0.15}FA_{0.85}PbI_{2.85}Br_{0.15}$. Then, the absorption coefficient as a function of the photon energy E_{ph} has been calculated (Fig. 4.12(C)). The optimised PVK thin-film annealed at T=100 °C for t=30 min presents a high and rather constant absorption coefficient in the order of $\alpha \sim 10^4$-10^5 cm^{-1} until E_{ph}~1.63 eV. Then, above this value, α starts to drop. The direct evaluation of the bandgap from the plot showing the absorption coefficient as a function of E_{ph} can lead to misleading results as the absorption onset is not clearly visible. However, a rough estimation of the bandgap can be carried out by conventionally looking at the energy value corresponding to $\alpha \sim 10^4$ cm^{-1}, which in this case is E_g~1.61 eV. The bandgap has been eventually determined by the Tauc plot. This is in fact considered one of the most commonly used and reliable method for evaluating the bandgap of PVKs. The Tauc plot in Fig. 4.12(D) allows to individuate a bandgap of E_g~1.60 eV (Table 4.6). By taking into account both the 2θ angle position of the (001)

PVK peak in the XRD diffractogram and the slight increase in the value of the bandgap with respect to the previously used evaluation methods suggest a PVK composition of $Cs_{0.16\text{-}0.17}FA_{0.83\text{-}0.84}PbI_{2.83\text{-}2.84}Br_{0.16\text{-}0.17}$. This is very close to the optimal composition for multications mixed-halides PVK as described in Section 4.1.1, but on the other hand it should be pointed out that the bandgap of E_g~1.60 eV should be further optimised, i.e. increased, for a monolithic PVK/Si tandem solar cell application (see Section 2.3.2).

Table 4.6: Bandgap of $Cs_{0.15}FA_{0.85}PbI_{2.85}Br_{0.15}$ thin-film annealed at temperature T=100 °C for t=30 min, calculated by using different methods, i.e. by looking at the absorption onset in the absorptance spectrum, the absorption coefficient as a function of E_{ph} and the Tauc plot.

Bandgap evaluation method	**E_g (eV)**
Absorptance spectrum	1.59
Absorption coefficient spectrum	1.61
Tauc plot	1.60

Finally, the thickness of the optmised PVK thin-film annealed at T=100 °C for t=30 min is equal to t~158.01 nm, as shown in Table 4.7. This is a consequence of the thermal evaporation process itself, as the other samples from the same deposition batch are also thicker than the expected thickness. This may be cause by a lack of control in the deposited thicknesses of the individual PVK precursors layers due to instrument limitations or reduced QCM sensor lifetime. Nevertheless, the typical uniformity of the thermally evaporated PVK thin-film is guaranteed by the acceptable thickness variations in the same sample and from one sample to the other. Lastly, the formation of a compact and uniform PVK thin-film and the absence of significant surface flaws can be verified by the BEs SEM images in Fig. 4.13 which are demonstrating, in spite of minor imperfections, the high-quality in terms of homogeneity, uniformity, smoothness and compactness of the PVK thin-films synthesised by thermal evaporation.

Table 4.7: Thickness measurements of $Cs_{0.15}FA_{0.85}PbI_{2.85}Br_{0.15}$ PVK thin-film annealed at temperature T=100 °C for t=30 min. The columns "Average thickness 1" and "Average thickness 2" refer to the measurements performed across the scratch 1 and scratch 2 engraved on the thin-film, respectively.

Sample	**Average thickness 1 (nm)**	**Average thickness 2 (nm)**	**Average thickness (nm)**
30 min	158.76	157.26	158.01

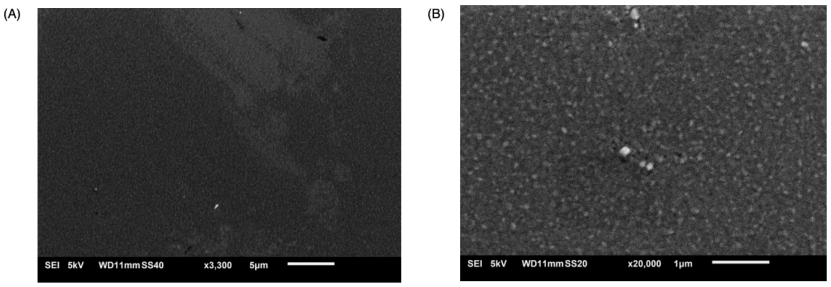

Figure 4.13: SEs SEM images with magnifications (A) x3300 and (B) x20000 at E=5 kV showing the topography of the $Cs_{0.15}FA_{0.85}PbI_{2.85}Br_{0.15}$ thin-film annealed at T=100 °C for t=30 min.

In closing, this optimisation process leads to individuate T=100 °C and t=30 min as the best annealing parameters to obtain high-quality thermally evaporated PVK thin-films showing valuable properties in terms of crystallinity, homogeneity, absorption, reflection, bandgap tuning and uniformity.

4.3. Thermal, Ambient Air and Synthesis Failures Degradation

Several thermally evaporated PVK thin-films synthesised during the optimisation process exhibit signs of degradation. Three main degradation phenomena can be recognised:

- Thermal degradation;
- Degradation in ambient air (H_2O and O_2);
- Degradation due to synthesis faults.

4.3.1. Thermal Degradation

Thermal degradation has been described more extensively in Section 2.4.1. In this MSc Thesis Project, thermal degradation is observed in PVK thin-films annealed at excessively high temperature. On the other hand, the long annealing times that cause thermal degradation are not explored.

Focusing on the PVK thin-film annealed at T=180 °C for t=8 min analysed in Section 4.2.1 and shown in Fig. 4.14, it can be said that thermal degradation causes the partial or total decomposition of PVK into PbI_2, as it is confirmed by the XRD diffractograms showing a significant increase in the characteristic PbI_2 peaks intensity. In fact, the easiest way to recognise this degradation phenomenon is to look at the rise in intensity of the (001) PbI_2 peak located at 2θ=12.7°. In addition to that, in the initial stages of the degradation, the bandgap tends to red-shift. Finally, pinholes develop in the PVK thin-film and they are visible as holes on its surface, as shown in Fig. 4.14.

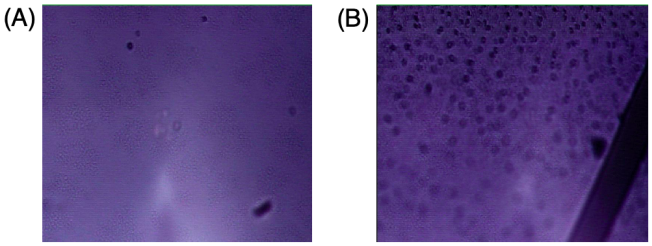

Figure 4.14: Photographs showing (A) the uniform surface of a PVK thin-film annealed at T=90 °C for t= 8 min and (B) pinholes formation as a result of thermal degradation in the PVK thin-film annealed at T=180 °C for t= 8 min.

Moreover, when the annealing temperature is too high some surface irregularities, like the ones present in Fig. 4.15 for the PVK thin-film annealed at T=150 °C for t=8 min studied in Section 4.2.1, may start to appear. Indeed, temperature facilitates the migration and rearrangement of the atoms on the surface of the PVK thin-film and within it [129]. This can be useful to improve the level of order in the PVK crystal structure, along with its crystallinity, phase homogeneity, grain size and morphology. However, the number of defects also increases as the temperature rises [83]. Thus, surface irregularities on the PVK thin-film may be a sign of the volatilization of I^- in the form of gaseous FAI, the creation of surface defects or formation of pinholes throughout the thickness of the sample.

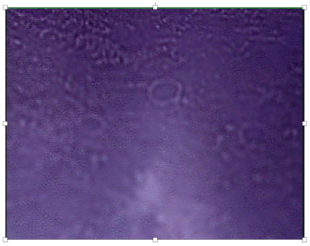

Figure 4.15: Photograph showing the surface irregularities developed upon annealing the PVK thin-film at T=150 °C for t= 8 min.

Therefore, the results show that for T≥150 °C the PVK thin-films start to exhibit the first evidence of thermal degradation, while for T=180 °C a partial decomposition of PVK and conversion to PbI_2 is already occurring, as it is confirmed by the literature on thermal stability of multications mixed-halides PVKs [83].

4.3.2. Degradation in Ambient Air

Some PVK thin-films exhibit instability in ambient air, i.e. moisture- and oxygen-induced degradation, as it can be seen in Fig. 4.16. The mechanism behind this phenomenon has been explained more precisely in Section 2.4.1.

In detail, the PVK thin-film annealed at T=120 °C for t=30 min in the second optimisation step (Section 4.2.1) presents a variation of colour developing a large and diffuse yellow area, visible in Fig. 4.16(A). This is supposed to be due to the action of the H_2O and O_2 molecules in the atmosphere, leading to the decomposition of PVK through hydrolysis and redox reactions. This degradation mechanism leads to the volatilisation of FAI and the conversion into PbI_2. This hypothesis is reinforced by the absorption decay and the red-shift of the absorption onset of this sample (Fig. 4.7(A)). On the other hand, the PVK thin-films annealed at T=100 °C

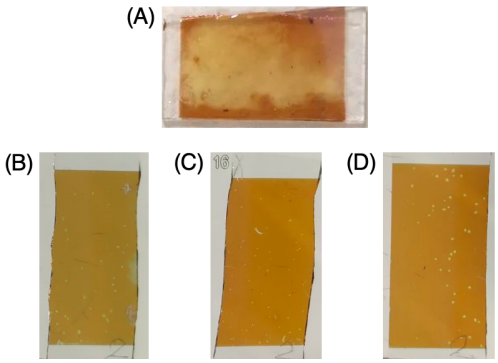

Figure 4.16: Photographs showing the degradation in ambient air of PVK thin-films (A) annealed at T=120 °C for t= 30 min, in which the decomposition of PVK in PbI_2 is clearly visible from the yellow colour taken on by the sample, and (B), (C) and (D) annealed at T=100 °C for t=25, 30 and 35 min, respectively, where it is possible to notice some randomly distributed yellow spots.

for t=25, 30 and 35 min analysed in the third optimisation step as deposition batch (ii) (Section 4.2.1) are all characterised by the presence of small and unevenly distributed yellow spots (Fig. 4.16(B), (C) and (D)), which are assumed to be PbI_2 domains, even though further analysis is necessary to verify it. Furthermore, all the PVK thin-films of deposition (ii) in Section 4.2.1 show a fairly blunt absorption onset and, more in detail, the PVK thin-film annealed at T=120 °C for t=30 min also exhibits a drop in absorption (Fig. 4.10(B)). All these considerations lead to the idea that in this case degradation in ambient air has also occurred.

It is hypothesised that the degradation in ambient air derives from a lack of Cs^+ causing instability and decomposition of the cubic α-PVK crystal structure. This is in line with the low Cs^+ content that can be inferred from the small bandgap of the PVK thin-film annealed at T=120 °C for t=30 min, which reveals the non-incorporation of CsBr during the thermal evaporation process. A Cs^+ deficiency may also explain the randomly distributed spots of instability in the PVK thin-films annealed at T=100 °C for t=25, 30 and 35 min. In these PVK thin-films, the stabilising ability of Cs^+ on the PVK crystal structure is no longer present and low-quality crystallinity, dull absoption onset and a smaller bandgap are indeed observed. This also justifies the formation of the small yellow spots, as the development of nucleation sites through defects, migration and accumulation of ions near grain boundaries and creation of new phases are aided in materials of low crystalline quality, i.e. with a short-range crystalline order [35].

The non-effective CsBr deposition may be a consequence of either intrinsic limitations or inappropriate choice of processing parameters (too thin CsBr layers) of the thermal evaporator for ensuring precise control and the set PVK composition. As an alternative potential explanation, thermal degradation of the powders used as source materials in the thermal evaporator takes place upon being subjected to several thermal cycles.

4.3.3. Degradation due to Synthesis Faults

Since a relation has been noticed between the specific degradation phenomenon affecting PVK thin-films and their position in the thermal evaporator sample holder relative to its center, it is supposed that synthesis faults occur. These faults consist in a deficiency of Cs^+ and Br^- in the samples, thus they look connected to evaporation or deposition issues of the CsBr source material. A schematic representation of the thermal evaporator sample holder and the PVK thin-films positioned on it, presenting signs of degradation can be seen in Fig. 4.17.

By observing the PVK thin-films resulting from an unsuccessful deposition batch in Fig. 4.18, some defects can be noticed.

These have been immediately visible right after the deposition, keeping the samples inside the glovebox. The sample without annealing shown in Fig. 4.18(A) features a large yellow area, corresponding probably to PbI_2, and a light orange-brown colour. This sample had been placed in the outermost position in the sample holder relative to its centre. Then, the sample annealed at T=100 °C for t= 30 min shown in Fig. 4.18(B) presents a small yellowish area potentially an excess of PbI_2, but the XRD measurements reveal the presence of an amorphous phase of PVK too. Again, the sample has an orange-brown colour. This sample had been located in the second outermost position in the sample holder relative to its centre. Finally, the PVK thin-film annealed at T=100 °C for t= 30 min shown in Fig. 4.18(C) is a perfectly synthesised PVK thin-film from the same deposition batch, shown as a comparison. It looks homogenoeus and uniform and it presents an intense brown colour. This sample had been positioned in the innermost part of the sample holder, namely

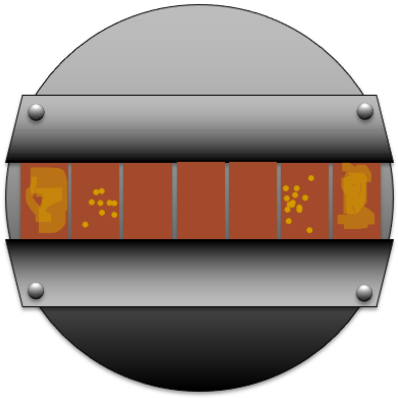

Figure 4.17: Illustration of the thermal evaporator sample holder showing how different degradation phenomena occur in PVK thin-films depending on their position relative to its center of the sample holder.

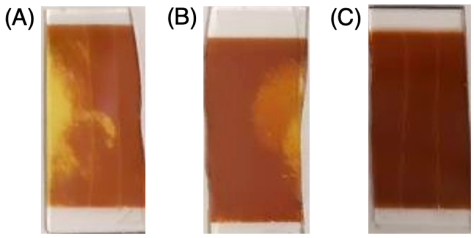

Figure 4.18: Photographs showing the synthesis faults and related degradation phenomena of PVK thin-films (A) without annealing and (B) and (C) annealed at T=100 °C for t= 30 min, resulting from an unsuccessful deposition with the thermal evaporator.

in its center.

It is deduced that the defects in the PVK thin-films of this imperfect deposition are caused by an ineffective reaction between the PVK precursors leading to an inhomogeneous deposition that produces different material phases. By analysing the PVK thin-films synthesis-related intrinsic degradation and their position on the sample holder to its center as shown before in Fig. 4.17, it can be assumed that the negative results of the failed reaction and the consequent lack of Cs^+ and Br^- in the samples is more significant in the samples occupying the outermost positions, whereas the central ones appear to be high-quality PVK thin-films.

Therefore, it is thought that the intrinsic degradation may derive from a remarkable deterioration of the source material powders located in the crucibles of the thermal evaporator upon being subjected to several thermal cycles. Therefore, these should be replaced more often to avoid this problem. However, it is important to emphasise that further analyses are required to fully understand the reasons behind the observed PVK degradation.

5

Hybrid $Cs_xFA_{1-x}PbI_{3-x}Br_x$ Thin-films Engineering

5.1. Preliminary Study - Two-step Spin-coated $Cs_xFA_{1-x}PbI_{3-x}Br_x$ Thin-films

The two-step spin coating synthesis technique is approached as preliminary study before starting to investigate the sequential thermal evaporation/spin-coating hybrid method. This is mainly carried out in order to understand the behaviour of a layer made of the inorganic PVK precursors in terms of wettability and reactivity when a solution of the organic PVK precursor comes into contact with it.

This preliminary studies aims to realise $Cs_xFA_{1-x}PbI_{3-x}Br_x$ PVK thin-films as close as possible to the composition of the ones deposited by thermal evaporation in Chapter 4 in order to create a comparison between the synthesis techniques. Thus, the processing parameters have been selected to try to synthesise PVKs with Cs:Br molar ratio equal to 1:1 and, by considering the information acknowledged in Section 4.1.1 and the good results previously obtained in Chapter 4, presenting a Cs^+ content of x~0.17. The main goals are obtaining the cubic α-phase PVK, phase homogeneity and uniform surface coverage. The bandgap tuning optimisation to achieve values of E_g~1.65-1.73 eV (Section 2.3.2) for a monolithic PVK/Si tandem application via Br^- incorporation and the charge transport properties is not prioritised at this stage of the hybrid synthesis method development.

5.1.1. Step 1 - Inorganic layer

Phase Analysis

Firstly, the structural properties of the layer synthesised in step 1 via spin coating of the PVK inorganic precursors solution, namely CsBr and PbI_2 dissolved in a mixture of DMSO and DMF, are analysed.

The details about the two-step spin coating processing parameters can be seen more in detail in Section 3.4.2, but some of the ones concerning the inorganic layer are shown in Table 5.1 as they will be recalled in the herein Section 5.1.1.

Table 5.1: Spun volume and molarities of the inorganic solution of CsBr and PbI_2 PVK precursors dissolved in a mixture of DMSO/DMF.

Spun volume (μL)	**M_{CsBr} (mol/L)**	**M_{PbI_2} (mol/L)**
100	$0.204 \cdot 10^{-3}$	$1.2 \cdot 10^{-3}$

The XRD diffractogram of the as-deposited inorganic layer is shown in Fig. 5.1. It is possible to recognise two main crystal phases, namely PbI_2 and the δ phase of the fully inorganic PVK resulting from the reaction between CsBr and Pb_2. The main (001) reflection of the hexagonal crystal structure of PbI_2 can be observed at 2θ=12.7° [89, 123, 124], along with two other XRD peaks corresponding to the (002) and (003) family of lattice planes. The other XRD peaks reveal the presence of the non-photoactive orthorhombic δ-PVK of composition $CsPbI_{3-x}Br_x$. This is reasonable, as this yellow phase is the thermodynamically stable phase of $CsPbI_{3-x}Br_x$ at RT and without the application of any annealing treatment [44, 130].

Considering the concentration of CsBr and PbI_2 in solution shown in Table 5.1, a PVK $CsPbI_{2.83}Br_{0.17}$ composition can be predicted, albeit it is difficult to ensure that the PVK precursors have fully reacted after

being deposited. Indeed, the absence of an annealing treatment not only implies that the solvents may still be present in the PVK thin-film, but also that not enough energy is provided to form the PVK crystal structure, leading to non-stoichiometric PVK or undesired materials. This idea is also supported by the presence of crystalline PbI_2, the generally low intensity of the XRD peaks in the diffractogram in relation to the background signal of the glass substrate (2θ=20-40°), which underlines low crystallinity, and the presence of a background signal for bigger 2θ angles. These observations lead to the assumption that the majority of the spin-coated material is present in the amorphous phase. Thus, it is presumed that the inorganic layer is characterised by an open morphology made of the amorphous phase of the PVK precursors, which has not fully reacted, in combination with crystallites of hexagonal PbI_2 and orthorhombic δ-$CsPbI_{3-x}Br_x$. However, further experiments and measurements are necessary to confirm it. Nevertheless, this type of morphology would allow the infiltration of the organic solution spun on it at a later stage and the development of an interdiffusion reaction (see Section 5.1.2) [131].

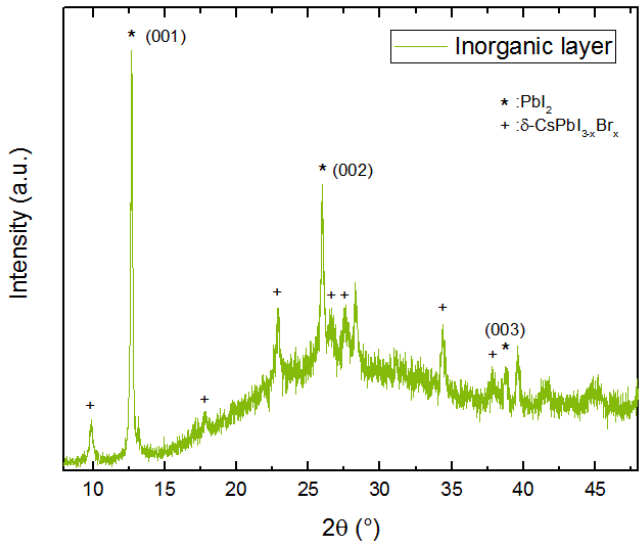

Figure 5.1: XRD diffractogram of the as-deposited spin-coated inorganic layer showing an orthorhombic δ phase of $CsPbI_{3-x}Br_x$. The peaks marked with (*), whose corresponding family of lattice planes is indicated, refer to PbI_2. The background signal measured in the range 2θ=20-40° is produced by the glass substrate.

Wettability and Reactivity

Subsequently, the wettability and reactivity properties of the inorganic layer with an open morphology are explored when the organic solution of FAI in IPA is spun on it. The most important processing parameters regarding the spin coating of the organic solution are shown in Table 5.2 as they will be mentioned again in the herein Section 5.1.1. More information can be found in Section 3.4.2.

Table 5.2: Spun volume and molarity of the organic solution of FAI PVK precursor dissolved in IPA.

Spun volume (μL)	**M_{FAI} (mol/L)**
100	$0.469 \cdot 10^{-3}$

The investigation of these aspects is carried out by changing the spin coating experimental procedure, in particular with regard to the transition from step 1 to step 2. The several experiments which are performed concern either the drying or annealing in the glovebox of the inorganic layer spin coated in step 1 and the dripping technique to deposit the organic solution in step 2. Table 5.3 lists the four process variants tested. The volumes of both the solutions of the inorganic and organic PVK precursors are kept constant for all the experiments, as well as their molarities (see Table 5.1 and Table 5.2).

Photographs of the samples resulting from the aforementioned experiments after annealing at T=100 °C for t=30 min are shown in Fig. 5.2.

First of all, a visual inspection allows to qualitatively observe the degree of surface spreading and infiltration of the organic solution on/in the inorganic layer and the interdiffusion reaction mechanism and

Table 5.3: Experiments to investigate the wettability and reactivity properties of the inorganic layer of CsBr and PbI_2 PVK precursors by change in the spin coating experimental method concerning the transition from step 1 to step 2. Each experiment corresponds to a sample, which is therefore identified by a number. The designation "CsBr+PbI_2" concerns variation on the inorganic layer treatment, while the designation "FAI" a refers to the dripping of the organic solution on it. The term "Step 2" means that the organic solution is spun in a separate step (step 2) after completion of step 1. The term "Continuous spinning" means that the inorganic layer is continuously spun for t=60 s and the organic solution is drop on it after the first 30 s without stopping the spinning.

Sample	**Drying (CsBr+PbI_2)**	**Annealing (CsBr+PbI_2)**	**Dripping (FAI)**
(1)	t=10 min	w/o	Step 2
(2)	t=0 min	w/o	Step 2
(3)	t=0 min	T=100 °C - t=1 min	Step 2
(4)	t=0 min	w/o	Continuous spinning

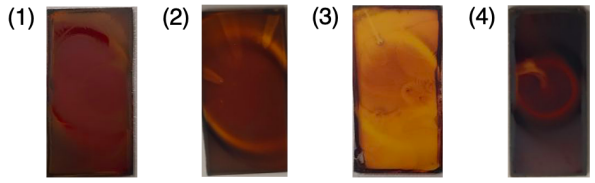

Figure 5.2: Photographs showing the PVK thin-films synthesised via two-step spin coating. The experimental methods are varied to study the wettability and reactivity properties of the inorganic layer when the organic solution is spin-coated on it. The numerical designation (1)(2)(3)(4) of the samples refers to the different experimental conditions applied for their synthesis and identified by the same number in Table 5.3. All samples are annealed at T=100 °C for t=30 min.

dynamic. During the experiments, it is observed that three out of four samples ((1),(2) and (4)) have an immediate reaction resulting to an intermediate phase thin-films as soon as the organic solution is spun on the inorganic layer. Then, annealing completes the reaction between the PVK precursors, which leads to the conversion of the thin-film to PVK and colour change. Sample ((3)) shows a failed reaction, even after annealing. After dripping the FAI in IPA solution, sample (3) does not convert in a PVK intermediate phase. The organic solution seems to infiltrate in the inorganic layer, but then it seems to not react in an appropriate manner. Consequently, the organic solution is lost, as it spreads out during the spinning stage, leaving behind a yellow inorganic layer with some imperfections due to the interaction with the organic solution, as seen in Fig. 5.2(3)). Therefore, sample (3) is discarded as it do not produce good results.

All the other samples (1),(2) and (4) show the conversion into an intermediate phase thin-film by turning from being yellow to a darker colour and do not show evident wettability problems to the naked eye, even after the annealing treatment. However, the typical oval halo that is created as an effect of the solution spinning in spin-coated thin-films is always visible. Upon annealing, the PVK precursors completely react and the residual solvents evaporate.

By taking into account their final colour, which gives an indication of potential variations in the chemico-physical and optical properties of PVK, sample (1) and (2) present some differences with respect to sample (4). Sample (1) and (2) show a caramel brown colour and a homogeneous and uniform appearance Fig. 5.2(1) and (2), while sample (4) presents a intense dark red colour and and it looks inhomogeneous due to the presence of an evident circular halo in the central zone where the organic solution droplets have been deposited Fig. 5.2(4). This inhomogeneity seems a systematic problem of PVK thin-film showing a red colour, as the same halos caused by the deposition of the organic solution droplets in step 2 appear in another deposition during this MSc Thesis project (not shown here, photographs of the relevant PVK thin-films are shown in Appendix B).

In order to appreciate the differences between these two types of PVK thin-films and try to better understand the mechanism of the interdiffusion reaction, sample (2) (similar to sample (1)) and sample (4) are chosen to be the focus of analysis in the herein Section 5.1.1. The XRD diffractograms of these PVK thin-films are shown in Fig. 5.3.

The XRD patterns clearly show several peaks reflecting the presence of a mixture of crystalline phases. The background signal measured in the range 2θ=15-35° is produced by the quartz substrate, whereas the one in the range 2θ=20-40° derives from the glass substrate. It is possible to see the typical XRD $PbI_{2-x}Br_x$ peaks and four different PVK phases, i.e. a cubic α-PVK, the orthorhombic photoactive (black) γ and the orthorhombic non-photoactive (yellow) δ phases of $CsPbI_{3-x}Br_x$ and the hexagonal non-photoactive (yellow)

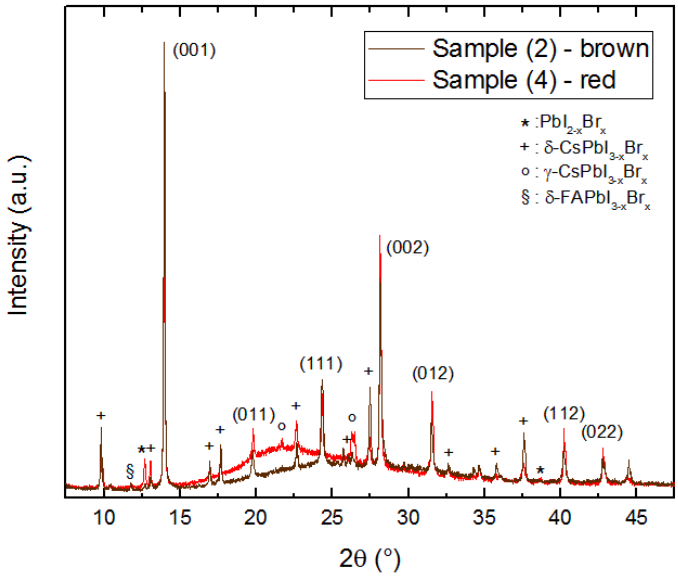

Figure 5.3: XRD diffractograms of sample (2) (brown) and sample (4) (red). Both samples are annealed at T=100 °C for t=30. The family of lattice planes that are indicated in the XRD pattern refer to the cubic α-phase of PVK. Other crystal phases can be observed. The background signal measured in the range 2θ=15-35° is produced by the quartz substrate, whereas the one in the range 2θ=20-40° derives from the glass substrate.

δ phase of $FAPbI_{3-x}Br_x$. It is worth mentioning that the γ-$CsPbI_{3-x}Br_x$ PVK easily converts to the δ–$CsPbI_{3-x}Br_x$ PVK at RT [131–135].

Although the XRD diffractograms are fairly similar, some phase differences can be observed between sample (2) and sample (4). When taking into account the effect of the background signal of the quartz and glass substrates, it can be noted that sample (2), i.e. the one brown in colour, presents somewhat higher intensity cubic α-PVK and yellow δ-$CsPbI_{3-x}Br_x$ peaks than sample (4), i.e. the one red in colour. Sample (2) shows also an XRD peak corresponding to the yellow δ-$FAPbI_{3-x}Br_x$ phase. On the other hand, sample (4) presents the same crystal phases, but the ratio between the intensity of the ideal cubic α-PVK peaks and those of the other unwanted phases is lower. Moreover, some XRD peaks of crystalline $PbI_{2-x}Br_x$, γ-$CsPbI_{3-x}Br_x$ and yellow δ-$CsPbI_{3-x}Br_x$ can also be identified.

The cubic α-PVK composition is supposed to be $Cs_yFA_{1-y}PbI_{3-x}Br_x$. The (001) reflection is located at 2θ=13.95° and the (002) reflection at 2θ=28.13°. As the XRD peaks present a very small right-shift towards higher 2θ angles with respect to the case of pure FA-based PVK [122, 131], it is thought that it contains only a really small amount of Cs^+ and Br^-. Therefore, the α-PVK lattice probably does not correctly incorporate Cs^+ and Br^- from the precursor solution and consequently is difficult to say if the molar ratio of Cs:Br is still 1:1 in the so-obtained cubic α-PVK. Indeed, Cs^+ forms the non-photoactive δ-$CsPbI_{3-x}Br_x$. Morover, as the difference in the XRD peaks position is tiny, some problems occur in Br^- integration too. This is the reason why the PVK of composition $Cs_yFA_{1-y}PbI_{3-x}Br_x$ shows y as Cs^+ content and x as Br^- content.

Therefore, it is evident that the interdiffusion reaction between the PVK precursors is unsuccessfull. During step 2 of the spin coating, the FA^+ ions can only partially interact with the original δ-$CsPbI_{3-x}Br_x$ inorganic layer, as the XRD peaks of the latter phase (inorganic layer) are still present. Consequently, although a cubic α-PVK is formed thanks to the partial substitution of the Cs^+ ions with the FA^+ ones, a deficiency in Cs^+ in this PVK is observed, as it is involved in the formation of the other γ-$CsPbI_{3-x}Br_x$ and δ-$CsPbI_{3-x}Br_x$ phases. On the other hand, Br^-, which was integrated as of step 1 of the spin coating, is instead probably incorporated in the various crystal phases shown in Fig. 5.3 forming mixed-halides compounds, but it is difficult to determine in exactly which molar ratio. Further experiments and measurements are necessary to investigate more precisely the infiltration and/or reactivity problems that seem to take place.

Sample (4) is analysed by means of SEM to have a deeper insight into the wettability and reactivity properties of the inorganic layer of step 1. The results of SEM analysis are shown in Fig. 5.4. It is possible to note in Fig. 5.4(A) an extremely non-uniform and rough surface. This is the result of the poor surface coverage that can be further noted in Fig. 5.4(B). Large holes visible on the film surface, revealing the underneath quartz substrate and round/oval particles. This demonstrates the existence of some wettability and reactivity prob-

lems. In the former case, the organic solution spun on the inorganic layer may not spread properly all over the surface of the inorganic layer or infiltrate it. This in turn negatively influences the interaction in the form of an interdiffusion reaction, which is ineffective. Then, once the residual solvent in the inorganic layer of step 1 and the IPA solvent used in step 2 fully evaporate after annealing, large holes and other phases are created as a result of the failed reaction between the inorganic layer and the organic solution spun on it. Among this other phases, the SEM images does not only show the large round/oval particles mentioned before, but also rod-like particles present both on the top (SEs SEM image in Fig. 5.4(C)) and inside (BEs SEM image in Fig. 5.4(D))the PVK thin-film. On the basis of the literature, it is assumed that the rod-like particles are hexagonal δ-$CsPbI_{3-x}Br_x$) crystals, as also evidenced by the XRD measurements [131].

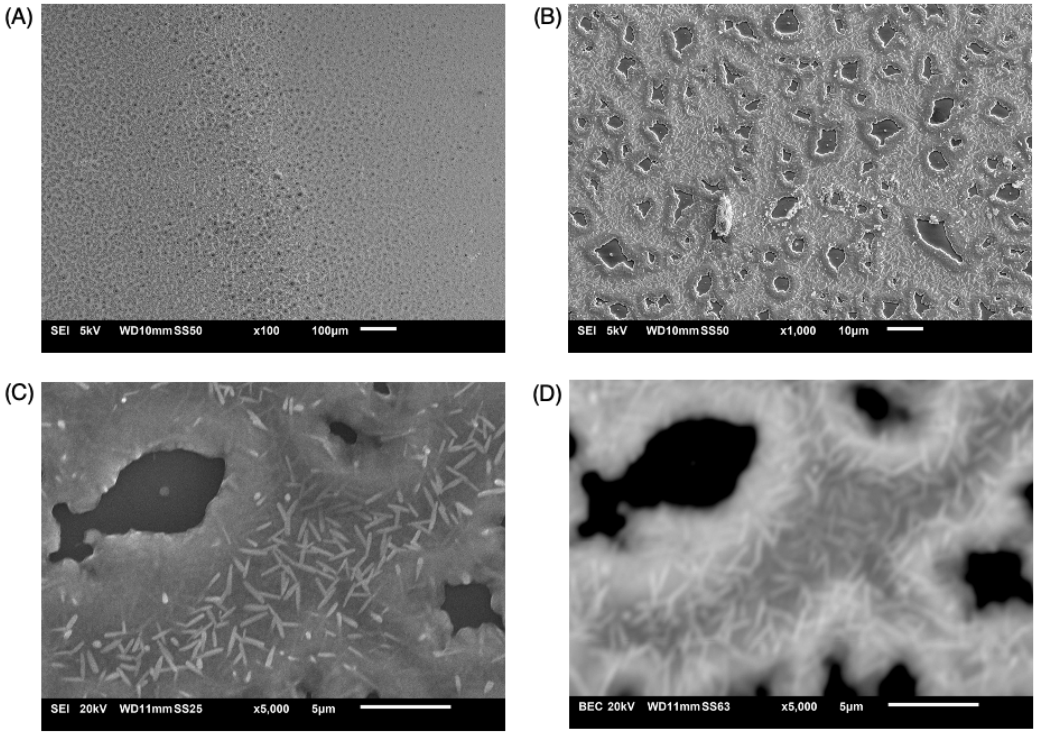

Figure 5.4: SEs and BEs SEM images of sample (4). The (A),(B) SEs SEM images show the non-uniform surface of the PVK thin-film, characterised by the presence of large holes revealing the underneath quartz substrate and round/oval particles on top of it. The (C) SEs and (D) BEs SEM images focus on the distribution of the rod-like particles both on top and inside the PVK thin-film. Sample (4) is annealed at T=100 °C for t=30.

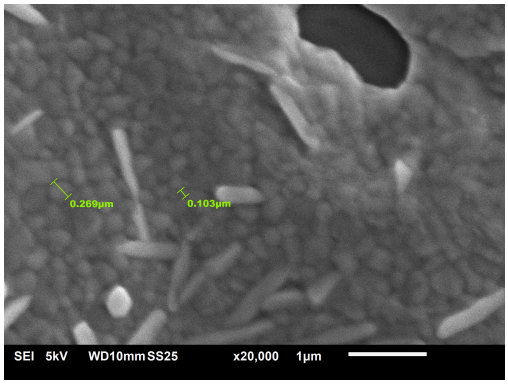

Figure 5.5: SEs SEM images of sample (4) presenting a dimensional analysis that shows the approximate value of the grain size on the surface of the PVK thin-film.

Lastly, a dimensional analysis of the grains on the surface of sample (4) is carried out via SEM to understand the features of the two-step spin-coated PVK thin-films (Fig. 5.5). The grain size varies from D~100 μm

and D~250 μm. Thus, the grains look larger than those of the thermally evaporated PVK thin-films shown in Chapter 4. This is expected, as spin coating usually produce PVK thin-films with larger grains than thermal evaporation (see Chapter 3), which generally results in superior charge carrier transport properties.

The optical properties and the bandgap values of PVK thin-films (2) and (4) can be seen in Fig. 5.6 and Table 5.4.

The absorptance spectra in Fig. 5.6(A) and the bandgap of E_g=1.53 eV shown in Table 5.4 demonstrate that both samples presents a photoactive cubic α-PVK phase, probably of composition $Cs_yFA_{1-y}PbI_{3-x}Br_x$ as mentioned before. It is worth noting that sample (4) shows a lower absorption and a less clear-cut absorption onset. This suggest the formation of other material phases with respect to sample (2), as the XRD peaks of $PbI_{2-x}Br_x$ and γ-$CsPbI_{3-x}Br_x$ confirm. Apart from that, with regards to the reflectance spectra shown in Fig. 5.6(B), it can be noted that sample (4) has a slightly higher reflectance than sample (2) (respectively R~15-17% and R~12-14%).

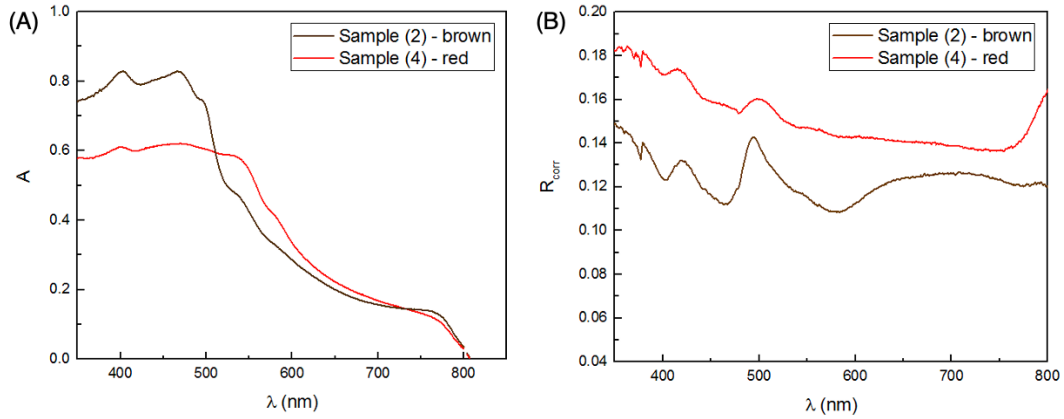

Figure 5.6: UV-Vis-NIR (A) absorptance and (B) reflectance spectra of samples (2) (brown) and (4) (red). Both samples are annealed at T=100 °C for t=30. The absorptance spectra have not been corrected by subtracting the absorption of quartz and glass substrates as it is close to A=0% for both. The reflectance spectra have been corrected considering the reflection of the quartz and glass substrates, around R~8-9% and R~9-10%, respectively. The dashed line prolonging the absorption spectra is present as a guide to the eye to mark the absorption onset and its intercept with the x-axis, related to the bandgap, as the information is missing due to erroneous measurement settings.

Table 5.4: Bandgap values of samples (2) (brown) and (4) (red), calculated from the absorptance spectra. Both samples are annealed at T=100 °C for t=30.

Sample	**E_g (eV)**
(2)	1.53
(4)	1.53

Considering what it is suggested in the literature, for PVK thin-films produced by the same two-step spin coating synthesis technique, it is speculated that the samples characterised by an orange-red coloration rather than dark-brown may present Br^--rich phases [131]. Thus, it can be speculated that the lower absorption of sample (4) which is, as mentioned before, probably caused by the presence of Br^--rich phases, is actually due to the presence of $PbI_{2-x}Br_x$ crystals containing a modest amount of Br^-. Indeed, they are not appearing in the XRD pattern of sample (2).

The existence of round/oval crystals of $PbI_{2-x}Br_x$ is verified by the SEM/EDX analysis carrie dout on sample (4) and presented in Fig. 5.7. In details, the BEs SEM image in Fig. 5.7(A) allows to see the $PbI_{2-x}Br_x$ crystals. As the BEs signal is more intense for high atomic number elements, they can be identified as the white round/oval crystals on the imperfect PVK thin-film surface. Then, their composition is analysed by SEM/EDS. The results shown in Fig. 5.7(B) reveal an non-stoichiometric $PbI_{2-x}Br_x$ compound with a Br^--rich composition. However, it must be underlined that SEM/EDS has some intrinsic limitations in providing an accurate analysis of the chemical composition, so critical thinking in interpreting the data is always necessary.

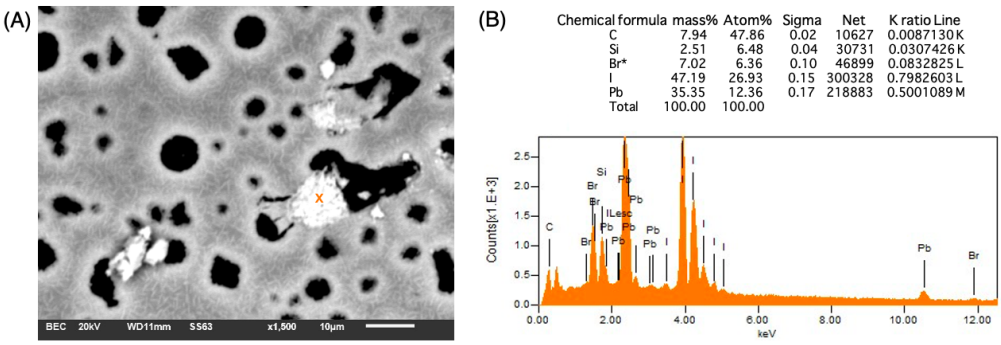

Figure 5.7: (A) BEs SEM image of sample (4), showing the imperfect surface of the PVK thin-film along with the round/oval $PbI_{2-x}Br_x$ crystals (white colour). (B) SEM/EDS chemical analysis performed at the spot indicated by the orange cross in (A) on the $PbI_{2-x}Br_x$ crystals. Sample (2) is annealed at T=100 °C for t=30 min.

Thickness Uniformity

Focusing on the thickness of the spin-coated PVK thin-films, it has to be pointed out that the initial thickness of the $CsPbI_{3-x}Br_x$ layer deposited in step 1 is not measured, as it is kept in the glovebox to avoid exposure to ambient air prior to spin coating of the organic solution of FAI in IPA in step 2. Nonetheless, the final thickness of the PVK thin-films is measured and analysed. Sample (2) and (4) thicknesses are shown in Table 5.5. It can be noticed that the final spin-coated PVK thin-films are rather thick (t_{PVK}~400 nm) and non-uniform, especially when compared to the thermally evaporated PVK thin-films shown in in Chapter 4. The thickness of the samples changes while scanning in different spots along the scratches realised on the samples (see Section 3.5.1) as an effect of the non-uniform spreading of the solutions of PVK precursors during the spinning of the respective substrate. In fact, as already mentioned, an oval halo can typically be seen in spin-coated PVK thin-films. Additionally, although sample (2) is not perfectly smooth, sample (4) is characterised by a noticeably rough appearance due to the surface irregularities and not-uniform coverage, as described in Section 5.1.1. Nevertheless, it can be stated that thickness variations between different samples of the same deposition batch are acceptable.

Table 5.5: Thickness measurements of samples (2) (brown) and (4) (red). Both samples are annealed at T=100 °C for t=30. The columns "Average thickness 1" and "Average thickness 2" refer to the measurements performed across the scratch 1 and scratch 2 engraved on the thin-film, respectively.

Sample	Average thickness 1 (nm)	Average thickness 2 (nm)	Average thickness (nm)
(2)	396.90	389.84	393.37
(4)	404.37	380.80	392.58

By taking into account that the PVK thin-films are rather thick and considering all the previous observations, it is even more evident that the two-step spin coating process does not lead to a complete conversion to the PVK crystal phase, as the PVK thin-films are not as dark in colour as expected, especially considering a thickness of t_{PVK}~400 nm.

It is important to highlight that, despite the predominance of the peaks of the cubic α-PVK, the coexistence of several other phases, most of them non-photoactive, deeply undermines the performance of PVK thin-films. Indeed, only the cubic α-PVK is the one presenting the ideal crystal structure to obtain the best chemico-physical and optoelectronic properties, as explained in Section 2.1. The absence of phase inhomogeneity is detrimental for the photon absorption, charge carriers generation and transport because of the non favourable intrinsic properties the other crystal structures of PVK. In addition to that, the presence of different crystalline domains increase the defect density. The increase in the amount of point defects, lattice mismatches at the GBs, lattice stresses and strains in turn enhances the charge-carrier recombination and ion migration. In a sort of vicious circle, this triggers the structural instability of the PVK thin-films, which can easily encounter degradation [35]. Moreover, the wettability and reactivity problems leading to other unwanted phases than the ideal cubic α phase of the desired multications mixed halides PVK of composition $Cs_xFA_{1-x}PbI_{3-xx}$, non-uniform surface coverage and roughness would need further investigation to adjust the processing parameters and improve the two-step spin coating synthesis technique.

In conclusion, it seems that the interdiffusion reaction does not work properly to form the desired multi-

cations mixed-halides PVK, but it seems that the PVK thin-films presenting a brown colour, have better characteristics, especially under the crystallinity, absorption and uniformity properties viewpoints. Hence, PVK thin-films showing a brown coloration are accepted, while the ones presenting a red colour are discarded.

Lastly, other PVK thin-films synthesised by the exactly same two-step spin coating process during this MSc Thesis Project (not shown here) demonstrate that drying in glovebox for t=10 min the inorganic layer prior to spin coating of the organic solution in leads to more homogeneous and uniform samples. Oppositely, the PVK thin-films obtained by immediate spin coating of the organic solution on the inorganic layer turn into an intermediate phase thin-film, but also show some halos, which are due to the organic solution droplets deposited on the surface becomes visible to the naked eye. This clearly shows a difficult surface spreading and thus wettability problems. Hence, it is concluded that the best PVK thin-films are produced by drying for t=10 min the inorganic layer (step 1) before spin coating of the organic solution (step 2).

In the following Section 5.1.2, the attention will be focus on the processing parameters concerning the organic solution of FAI in IPA step 2 and annealing to try to improve the two-step spin coating synthesis technique.

5.1.2. Step 2 - Organic Solution

After the first development step, in the second development step the focus shifts to the investigation of the processing parameters regarding the organic solution of FAI in IPA. The spun volume and concentration are varied as shown in Table 5.6 to observe the resulting effect on the properties of the PVK thin-films.

Table 5.6: Experiments to investigate the effect of the variation of the spun volume and molarity of the organic solution of FAI PVK precursor to be spin-coated on the inorganic layer in step 2. All samples are characterised by the drying stage of the inorganic layer and annealing at T=100 °C for t=30.

Sample	Spun volume (μL)	Molarity (mol/L)
(1)	80	$0.469 \cdot 10^{-3}$
(2)	120	$0.469 \cdot 10^{-3}$
(3)	120	$0.389 \cdot 10^{-3}$
(4)	120	$0.548 \cdot 10^{-3}$

Effect of the Spun Volume of the Organic Solution

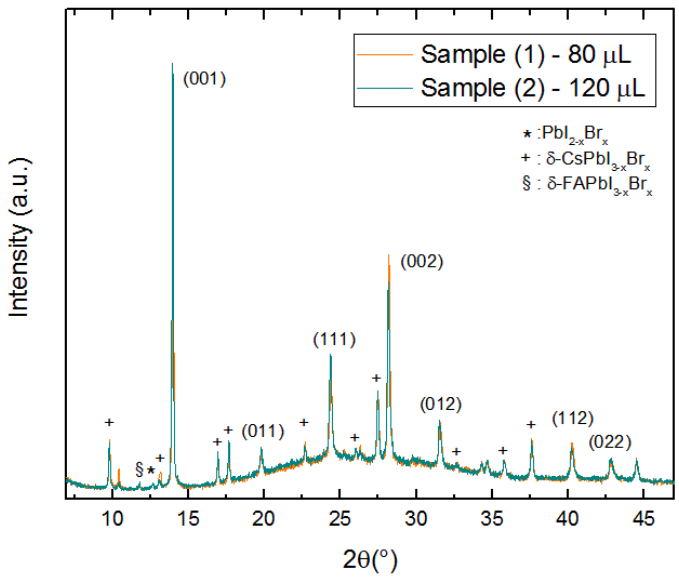

Figure 5.8: (XRD diffractograms of sample (1) (V_{FAI}=80 μL) and sample (2) (V_{FAI}=120 μL). Both samples are characterised by the drying stage of the inorganic layer and annealing at T=100 °C for t=30. The family of lattice planes that are indicated in the XRD pattern refer to the cubic α-phase of PVK. Other crystal phases can be observed. The background signal measured in the range 2θ=20-40° derives from the glass substrate.

By looking at Table 5.6, it is possible to see that two different volumes of FAI in IPA are spun on the inorganic layer surface, namely V_{FAI}=80μL (1) and V_{FAI}=120μL (2), to study the influence of the amount of organic solution deposited on the inorganic layer on the final PVK thin-films. The volume of inorganic solution spun on the glass substrate in step 1 is kept constant at $V_{CsBr+PbI_2}$=80μL in both the experiments (1) and (2). So, the ratio between the spun volumes in step 1 and step 2 ($V_{CsBr+PbI_2}$:V_{FAI}) is equal to 1:1 for sample (1), whereas it is equal to 3:2 for sample (2).

The XRD diffractograms of sample (1) and (2) can be observed in Fig. 5.8. It is possible to recognise a mixture of four crystal phases, namely a cubic α-PVK, $PbI_{2-x}Br_x$, δ-$CsPbI_{3-x}Br_x$ and δ-$FAPbI_{3-x}Br_x$. No γ-$CsPbI_{3-x}Br_x$ phase is identified [89, 123, 124, 131–135]. As mentioned before, predicting the cubic α-PVK composition is not trivial, as it cannot be verified by the measurements carried out in this MSc Thesis Project that the PVK precursors have fully reacted after being deposited. Nevertheless, the composition is supposed to be expressed as $Cs_yFA_{1-y}PbI_{3-x}Br_x$. By looking at the XRD α-PVK peaks position, the content of both Cs^+ and Br^- is assumed to be low. The (001) reflection is located at 2θ=13.97° and the (002) reflection at 2θ=28.17°, thus the tiny right-shift towards higher 2θ angles is supposed to be related to a slight better incorporation of Cs^+ and Br_- in this deposition batch. However, as the difference is almost negligible, this and the absence of γ-$CsPbI_{3-x}Br_x$ phase is attributed to the inherent sensitivity of the spin coating synthesis technique to various atmospheric and human factors. This hinders the reproducibility of such PVK thin-films. Lastly, it is clear that the problems in the interdiffusion reaction and full conversion to a multications mixed-halides PVK are still present.

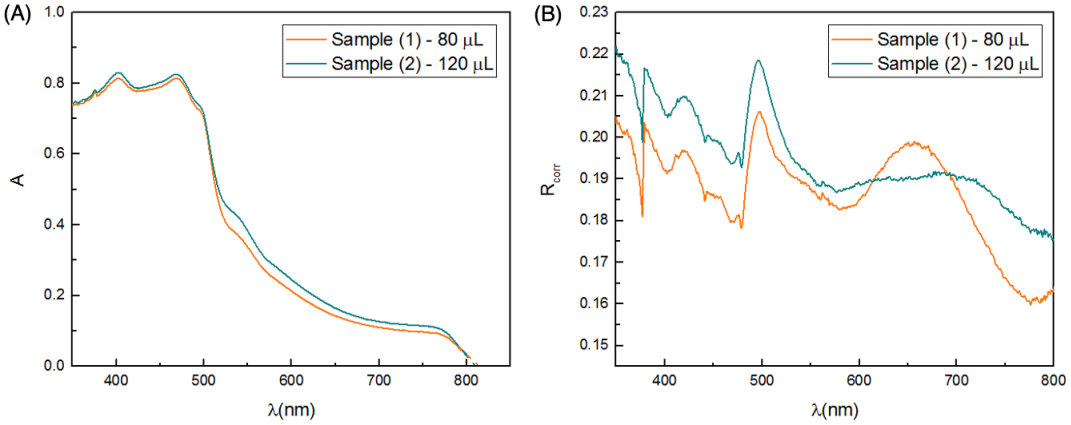

Figure 5.9: UV-Vis-NIR measurements showing the (A) absorptance and (B) reflectance spectra of samples (1) (V_{FAI}=80 μL) and (2) (V_{FAI}=120 μL). Both samples are characterised by the drying stage of the inorganic layer and annealing at T=100 °C for t=30. The absorptance spectra have not been corrected by subtracting the absorption of the glass substrate as it is close to A=0% for both. The reflectance spectra have been corrected considering the reflection of the glass substrate, around R~9-10%. The dashed line prolonging the absorption spectra is present as a guide to the eye to mark the absorption onset and its intercept with the x-axis, related to the bandgap, as the information is missing due to erroneous measurement settings.

Table 5.7: Bandgap values of samples (1) (V_{FAI}=80 μL) and (2) (V_{FAI}=120 μL), calculated from the absorptance spectra. Both samples are characterised by the drying stage of the inorganic layer and annealing at T=100 °C for t=30.

Sample	**E_g (eV)**
(1)	1.52
(2)	1.53

Since the XRD diffractograms of sample (1) and (2) are fairly similar, absorption and reflection properties along with the bandgap values of sample (1) and (2) are analysed in Fig. 5.9 and Table 5.7 to seek for any difference between the two PVK thin-films.

The PVK thin-films show a good absorption profile, as the absorption is high (A~80%) for blue light (λ <500 nm) and drops quite sharply to lower values for the range of wavelengths from green to red light (λ >500 nm). This can be appreciated by envisioning an application in a monolithic PVK/Si tandem solar cell. The absorptance spectra of samples (1) and (2) (Fig. 5.9(A)) are similar too, but, to be more precise, sample (2) shows a slightly higher absorption and sharper absorption onset. Moreover, it presents also a lit-

tle higher reflectance (Fig. 5.9(B)). The bandgap of the two samples is also similar and equal to, respectively, E_g~1.52 eV and E_g~1.53 eV (Table 5.7).

Lastly, the thickness measurements of sample (1) and (2) are presented in Table 5.8. The large thickness typical of two-step spin-coated PVK thin-films that has been noted in Section 5.1.1 is confirmed.

Table 5.8: Thickness measurements of sample (1) (V_{FAI}=80 μL) and sample (2) (V_{FAI}=120 μL). Both samples are characterised by the drying stage of the inorganic layer and annealing at T=100 °C for t=30 min. The columns "Average thickness 1" and "Average thickness 2" refer to the measurements performed across the scratch 1 and scratch 2 engraved on the thin-film, respectively.

Sample	Average thickness 1 (nm)	Average thickness 2 (nm)	Average thickness (nm)
(1)	370.45	375.96	373.21
(2)	382.34	372.00	377.17

All the previous observations leads to the hypothesis that the organic solution of FAI in IPA infiltrates the open morphology structure of the inorganic layer, part of the volume is retained and then the interdiffusion reaction starts to take place (annealing is necessary to complete it) and finally the rest of the solution is ejected off it during spin coating [70]. Thus, dripping a larger volume of organic solution in step 2 on the inorganic layer of step 1 does not entail any significant change. Nonetheless, considering the absorption properties and the bandgap, sample (2) properties appear a little bit better than those of sample (1). Therefore, it is concluded that a larger spun volume of the organic solution is a better choice, as it seems to help, albeit to a very limited extent, the conversion of the inorganic layer into the photoactive cubic α-PVK. Moreover, the residual solution is spread out of the thin-film during the spin-coating in step 2 without any accumulation or any undesirable consequences.

Since the spun volume in step 2 seems to not have a big influence on the quality of the samples, the study of the effect of the concentration of FAI in IPA on the two-step spin-coated PVK thin-films will be carried out in the next Section 5.1.2.

Effect of the Concentration of the Organic Solution

After the investigation of the spun volume, the concentration of the organic solution of FAI in IPA is modified to observe its effect on the PVK thin-films properties. The concentration of the organic solution of step 2 is increased progressively from experiments (3) to (2) to (4) as shown in Table 5.6 to observe the effect on the properties of the resulting PVK thin-films.

The XRD diffractograms of samples (3),(2) and (4) are presented in Fig. 5.10 and Fig. 5.11. It is possible to notice, similarly to Section 5.1.1 and Section 5.1.2, the coexistence of cubic α-PVK, $PbI_{2-x}Br_x$, γ-$CsPbI_{3-x}Br_x$, δ-$CsPbI_{3-x}Br_x$ and δ-$FAPbI_{3-x}Br_x$ [89, 123, 124, 131–135].

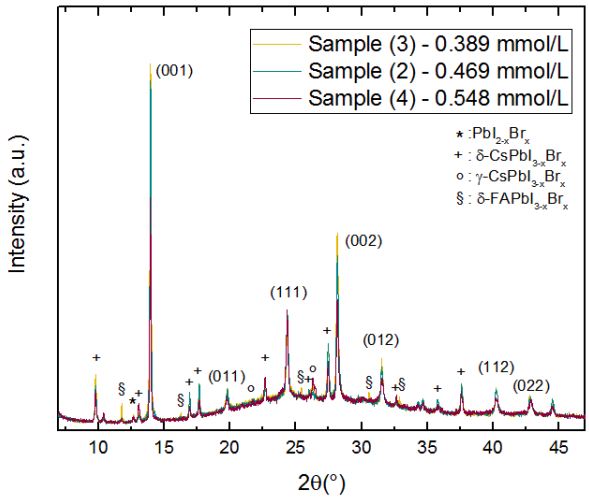

Figure 5.10: XRD diffractograms of sample (3) (M_{FAI}= 0.389 · 10^{-3} mol/L), sample (2) (M_{FAI}= 0.469 · 10^{-3} mol/L) and sample (4) (M_{FAI}= 0.548 · 10^{-3} mol/L). All samples are characterised by the drying stage of the inorganic layer, spun volume of organic solution V_{FAI}=120 μL and annealing at T=100 °C for t=30. The family of lattice planes that are indicated in the XRD pattern refer to the cubic α-phase of PVK. Other crystal phases can be observed. The background signal measured in the range 2θ=20-40° derives from the glass substrate.

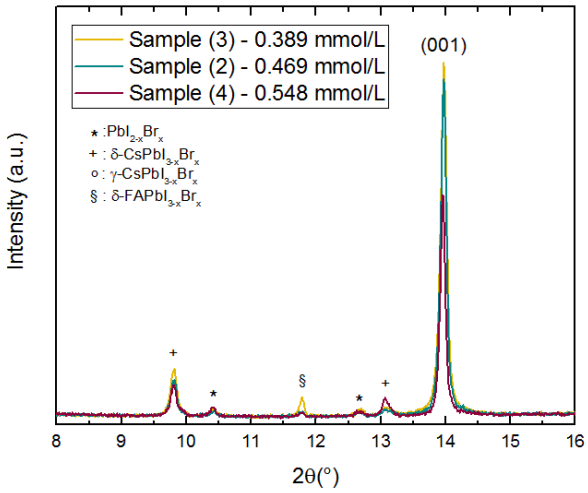

Figure 5.11: (Detail of the XRD pattern for low angles 2θ=8°-16° of sample (3) (M_{FAI}= 0.389 · 10^{-3} mol/L), sample (2) (M_{FAI}= 0.469 · 10^{-3} mol/L) and sample (4) (M_{FAI}= 0.548 · 10^{-3} mol/L). All samples are characterised by the drying stage of the inorganic layer, spun volume of organic solution V_{FAI}=120 μL and annealing at T=100 °C for t=30. The family of lattice planes that are indicated in the XRD pattern refer to the cubic α-phase of PVK. Other crystal phases can be observed. The background signal measured in the range 2θ=20-40° derives from the glass substrate.

Oppositely to the previous stage of the development of the two-step spin coating synthesis technique (Section 5.1.2), some differences can be recognised from one PVK thin-film to another. For sample (3), corresponding to the lowest FAI concentration, the XRD peaks of the cubic α-PVK are the highest, followed by sample (2) and (4). Therefore, it is likely that the lowest the FAI concentration, the more effective the conversion of the inorganic layer into the desired photoactive cubic α phase of PVK. As mentioned previously, the PVK composition is assumed to be $Cs_yFA_{1-y}PbI_{3-x}Br_x$ with a low content of Cs^+ and Br^- as deduced by the position of the (001) and (002) peaks at 2θ=13.97° and 2θ=28.17°, respectively. However, for a low FAI concentration, the XRD peaks of the δ-$FAPbI_{3-x}Br_x$ phase increase in intensity and the PVK thin-film tends to turn red more easily during the two-step spin coating process. On the other hand, for a high FAI concentration (sample(4)), the XRD peaks corresponding to the δ-$CsPbI_{3-x}Br_x$ are a little bit lower than samples (3) and (2), but the XRD reflections of γ-$CsPbI_{3-x}Br_x$ phase appear. Additionally, the PVK thin-film starts to become yellowish when exposed to the ambient air, revealing structural instability of PVK.

Besides, the intermediate FAI concentration (sample (2)) leads to PVK thin-films presenting the second highest intensity XRD peaks of the cubic α-PVK phase, typical caramel brown colour and good structural stability in ambient air. However, the unwanted δ-$CsPbI_{3-x}Br_x$ phase is still present. As already mentioned before, this is probably due to the incomplete conversion of the inorganic layer into the multications mixed-halides cubic α-PVK of interest.

It is hypothesised that changing the concentration of the organic solution of step 2 alters the the intermolecular activity, density, surface tension and viscosity of the organic solution and in turn affects the infiltration of the organic solution into the inorganic layer and interdiffusion reaction between the PVK precursors. The optimum is found for sample (2), corresponding to the intermediate FAI concentration.

Then, the optical properties and the bandgap of samples (3),(2) and (4) are analysed, as shown in Fig. 5.12 and Table 5.9.

As it can be seen in Fig. 5.12(A), Sample (3) (low FAI concentration) presents the lowest absorption for short wavelengths photons ($\lambda \lesssim$500 nm) and the highest for long wavelengths photons ($\lambda \gtrsim$500 nm) among all samples. Conversely, sample (4) (high FAI concentration) shows the highest absorption for short wavelengths photons ($\lambda \lesssim$500 nm) and the lowest for long wavelengths photons ($\lambda \gtrsim$500 nm) among all samples. Therefore, sample (4) is characterised by the best absorption profile for a 2-T PVK-Si tandem application, as explained in Section 5.1.2. Moreover, sample (4) presents a dull absorption onset, which reflects the instability in ambient air and consequent degradation that has been observed before. The optimum absorption is found again for sample (2), corresponding to the intermediate FAI concentration. The reflection properties shown in Fig. 5.12(B) are quite similar for all samples, with the reflectance fluctuating in the range R=16-22%. The bandgap E_g~1.53 eV is the same for all samples (Table 5.9).

Finally, the thicknesses of samples (3),(2) and (4) are presented in Table 5.10. In spite of the typical large

thickness of the PVK thin-films synthesised via the two-step spin coating process of this Section 5.1, it is interesting to note the relationship between the concentration of the organic solution in step 2 and the final thickness of the sample. Indeed, the thickness increases for increasing concentrations of FAI, while from the previous study (Section 5.1.2) the spun volume of organic solution, has no influence. It is therefore assumed that the main factor influencing the wettability of the inorganic layer and the interdiffusion reaction between the PVK precursors is the concentration of the organic solution rather than it amount. Nevertheless, further research is needed on the effect of the concentration of the organic solution in phase 2.

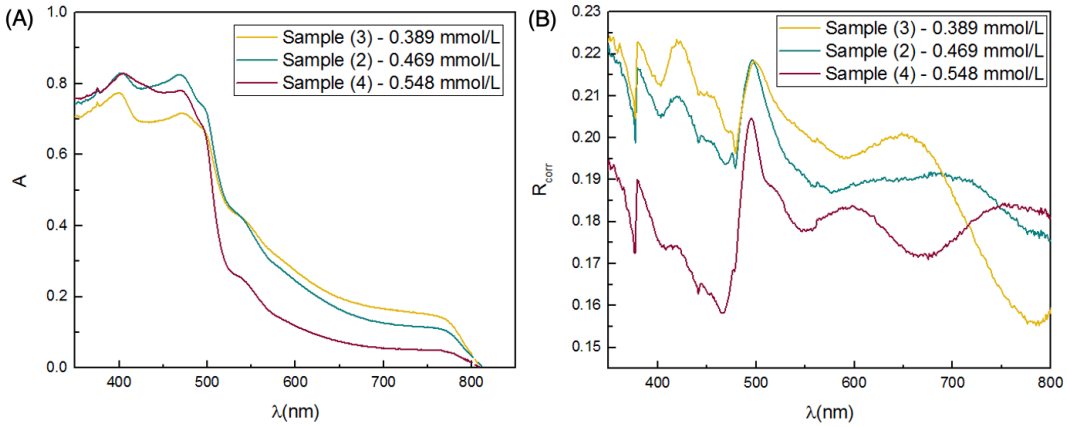

Figure 5.12: UV-Vis-NIR measurements showing the (A) absorptance and (B) reflectance spectra of sample (3) (M_{FAI}= 0.389 · 10^{-3} mol/L), sample (2) (M_{FAI}= 0.469 · 10^{-3} mol/L) and sample (4) (M_{FAI}= 0.548 · 10^{-3} mol/L). All samples are characterised by the drying stage of the inorganic layer, spun volume of organic solution V_{FAI}=120 μL and annealing at T=100 °C for t=30. The absorptance spectra have not been corrected by subtracting the absorption of the glass substrates as it is close to A=0% for both. The reflectance spectra have been corrected considering the reflection of the glass substrate, around R~9-10%. The dashed line prolonging the absorption spectra is present as a guide to the eye to mark the absorption onset and its intercept with the x-axis, related to the bandgap, as the information is missing due to erroneous measurement settings.

Table 5.9: Bandgap values of samples of samples (1) (V_{FAI}=80 μL) and (2) (V_{FAI}=120 μL), calculated from the absorptance spectra. Both samples are characterised by the drying stage of the inorganic layer and annealing at T=100 °C for t=30.

Sample	E_g (eV)
(3)	1.53
(2)	1.53
(4)	1.53

Table 5.10: Thickness measurements of sample (3) (M_{FAI}= 0.389 · 10^{-3} mol/L), sample (2) (M_{FAI}= 0.469 · 10^{-3} mol/L) and sample (4) (M_{FAI}= 0.548 · 10^{-3} mol/L). All samples are characterised by the drying stage of the inorganic layer, spun volume of organic solution V_{FAI}=120 μL and annealing at T=100 °C for t=30.

Sample	Average thickness 1 (nm)	Average thickness 2 (nm)	Average thickness (nm)
(3)	367.78	346.04	356.91
(2)	382.34	372.00	377.17
(4)	446.00	441.74	443.88

To conclude, this analysis leads to individuate V_{FAI}=120 μL and M_{FAI}= 0.469 · 10^{-3} as optimal spun volume and concentration relative to the organic solution of FAI in IPA for step 2. It is thought that such processing parameters favour the formation of a higher fraction of photoactive cubic α phase during the two-step spin coating process.

5.1.3. Effect of the Post-deposition Thermal Annealing

In the third development step, different annealing temperatures and times are tested. As presented in the overview of the experiments in Table 5.11, samples (1),(2) and (3) are subjected to the same annealing temperature T=100 °C, which was found as the optimal for thermally evaporated PVK thin-films as demonstrated

in Chapter 4, for different long annealing times (t=30-90 min). The annealing of sample (4) is performed to analyse the effect of high annealing temperature (T=150 °C) for a short annealing time (t=15 min).

Table 5.11: Experiments to investigate the effect of the variation of annealing temperature and time on the PVK thin-films synthesised by two-step spin coating. All samples are characterised by the drying stage of the inorganic layer, spun volume of organic solution V_{FAI}=120 μL and concentration M_{FAI}= 0.469 · 10^{-3} mol/L.

Sample	Temperature (°C)	Time (min)
(1)	100	30
(2)	100	60
(3)	100	90
(4)	150	15

The XRD patterns of samples (1),(2),(3) and (4) are shown in Fig. 5.13 and Fig. 5.14.

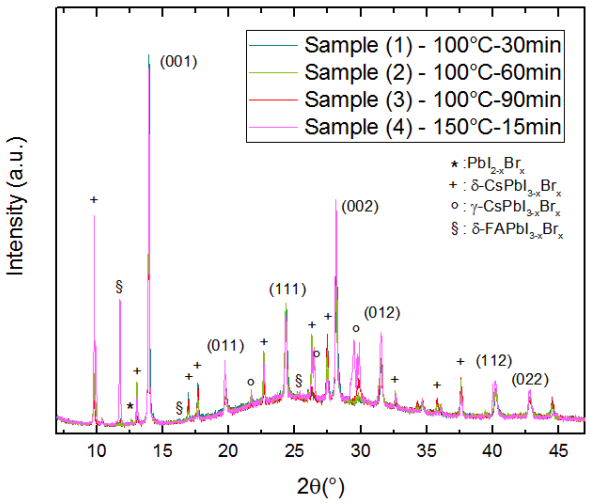

Figure 5.13: (A) XRD diffractograms and of sample (1) (T=100 °C for t=30 min), sample (2) ((T=100 °C for t=60 min)), sample (3) ((T=100 °C for t=90 min)) and sample (4) (T=150 °C for t=15 min). All samples are characterised by the drying stage of the inorganic layer, spun volume of organic solution V_{FAI}=120 μL and concentration M_{FAI}= 0.469 · 10^{-3} mol/L. The family of lattice planes that are indicated in the XRD pattern refer to the cubic α-phase of PVK. Other crystal phases can be observed. The background signal measured in the range 2θ=20-40° derives from the glass substrate.

It can be noted that, as it has been seen for the previous stages of the development of the two-step spin-coating process, a mixture of phases is present in the PVK thin-films, cubic α-PVK, $PbI_{3-x}Br_x$, γ-$CsPbI_{3-x}Br_x$, δ-$CsPbI_{3-x}Br_x$ and δ-$FAPbI_{3-x}Br_x$ [89, 123, 124, 131–135]. Sample (1) presents high intensity XRD peaks of the cubic α-PVK. As the annealing temperature or time increases, the intensity ratio between the XRD peaks of the ideal cubic α phase and the other undesired phases decreases. More precisely, sample (2) and (4) XRD patterns are characterised by split double peaks which are typical of the orthorhombic γ-$CsPbI_{3-x}Br_x$ phase [133]. Sample (2) shows the splitting of the peak at 2θ=26.29° and 2θ=26.45°. In addition to this, sample (4) presents not only another split peak at 2θ=29.49° and 2θ=29.89°, but also highly intense XRD peaks of δ-$FAPbI_{3-x}Br_x$ phase.

Therefore, the phase analysis based on the XRD diffractograms already clarifies that high annealing temperatures (T=150 °C) and, even though to a minor extent, long annealing times (t≥60 min), induce the formation of higher fractions of unwanted phases, i.e. γ-$CsPbI_{3-x}Br_x$, δ-$CsPbI_{3-x}Br_x$ and δ-$FAPbI_{3-x}Br_x$ with respect to the ideal cubic α phase PVK crystal structure.

In closing, the optimal annealing parameters for these two-step spin-coated PVK thin-films are T=100 °C for t=30 min, similarly to thermally evaporated PVK thin-films.

The optical properties, bandgap and thickness measurements and calculations of these PVK thin-films can be seen in Appendix C.

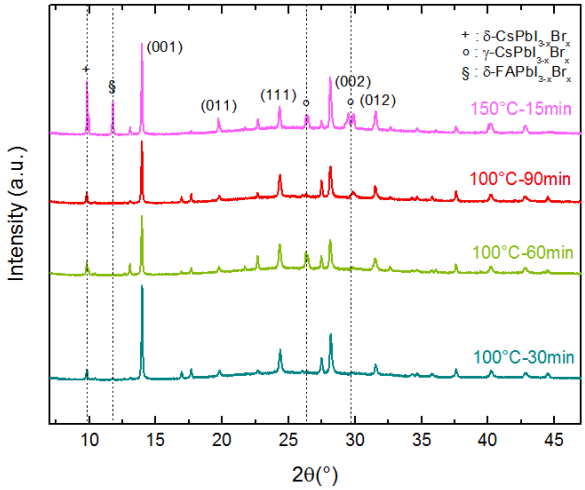

Figure 5.14: (A) Comparison of the XRD diffractograms and of sample (1) (T=100 °C for t=30 min), sample (2) ((T=100 °C for t=60 min)), sample (3) ((T=100 °C for t=90 min)) and sample (4) (T=150 °C for t=15 min), showing the XRD peaks of the cubic α-phase of PVK together with a main XRD peak for each of the other phases present in the PVK thin-films. All samples are characterised by the drying stage of the inorganic layer, spun volume of organic solution V_{FAI}=120 μL and concentration M_{FAI}= $0.469 \cdot 10^{-3}$ mol/L. The family of lattice planes that are indicated in the XRD pattern refer to the cubic α-phase of PVK. Other crystal phases can be observed. One main peak for each is indicated and black dashed lines are present as a guide to the eye to the other XRD patterns. The background signal measured in the range 2θ=20-40° derives from the glass substrate.

5.2. Development of the Thermal Evaporation/Spin Coating Hybrid Synthesis Technique

The development of the thermal evaporation/spin coating hybrid synthesis in this MSc Thesis Project is based on the observations from the layer-by layer multisource thermal evaporation in Chapter 4 and the preliminary study based on the development of the two-step spin coating process in Section 5.1.

In order to compare the two different synthesis techniques, the goal is to obtain hybrid $Cs_xFA_{1-x}PbI_{3-x}Br_x$ PVK thin-films with the same or similar composition to the two-step spin-coated ones developed during the preliminary study in Section 5.1. However, the spin-coated PVK thin-films have exhibited problems in terms of the incorporation of Cs^+ and Br^-. Therefore, the content of Cs^+ and Br^- in the multication mixed-halides PVK thin-films is kept low at this early stage of the development of the hybrid synthesis technique. In terms of PVK engineering, the long-term aim is to modify the composition of hybrid PVK thin-films to approximate that of thermally evaporated ones, so that these two methods compatible for depositions of non-flat substrates can be compared, and then to address the optimisation of the bandgap for a monolithic PVK/Si tandem application.

It should be kept in mind that thermal evaporation allows a certain degree of control over the composition of PVK through the processing parameters. In particular, the Cs:Br molar ratio equal to 1:1 is guaranteed by the use of CsBr as source material and the content of Cs^+ and Br^- can be adjust by modifying the thicknesses of the individual thermally evaporated layers. On the other hand, the amount of FAI incorporated in the thermally evaporated inorganic layer during the spin coating step is not easy to determine.

Taking into account all the above considerations, for this initial stage of the development of the hybrid synthesis technique the aim is to obtain PVK thin-films showing the cubic α-phase PVK, phase homogeneity, good optical properties and uniform surface coverage. In terms of compositional engineering, considering the lack of complete control on the composition of PVK, the bandgap optimisation for a monolithic PVK/Si tandem application (Section 2.3.2) and the charge transport properties analysis are not considered a priority at this stage of the hybrid synthesis method development.

5.2.1. Thermal Evaporation of the Inorganic Layer

Phase Analysis

As first development stage, the structural properties of the thermally evaporated inorganic bilayer of CsBr and PbI_2 are investigated.

The processing parameters of the thermal evaporation/spin coating hybrid method developed in this MSc

Thesis Project are explained more precisely in Section 3.4.2, but some of them are reported in Table 5.12 to help in the comprehension of some aspects explained in the herein Section 5.2.1.

Table 5.12: Individual layer thicknesses and deposition rates referred to the inorganic bilayer of CsBr and Pb_2.

Material	**Layer thickness (nm)**	**Deposition rate (Å/s)**
CsBr	18	0.2
PbI_2	360	0.7

The XRD diffractogram of the as-deposited thermally evaporated inorganic bilayer is shown in Fig. 5.15.

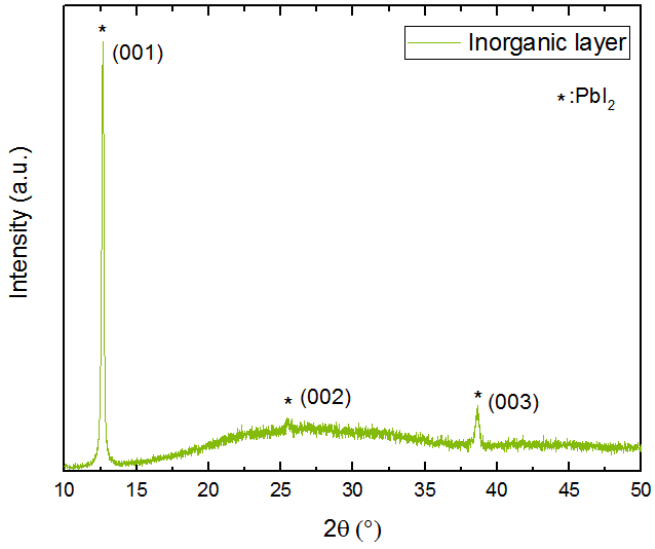

Figure 5.15: XRD diffractogram of the as-deposited thermally evaporated inorganic bilayer showing an hexagonal PbI_2 crystal phase. For each XRD peak, the corresponding family of lattice planes of PbI_2 is indicated. The background signal measured in the range 2θ=20-40° is produced by the glass substrate.

It is possible to recognise the typical XRD peaks of crystalline PbI_2. The main (001) reflection of the hexagonal crystal structure of PbI_2 can be observed at 2θ=12.67°, along with two other XRD peaks corresponding to the (002) and (003) family of lattice planes at 2θ=25.49° and 2θ=38.65°, respectively [89, 123, 124]. The high intensity of (001) reflection make it dominate with respect to the other peaks and it suggests a preferential orientation growth of the crystallites of PbI_2 in the low pressure conditions of the HV chamber of the thermal evaporator. The presence of only PbI_2 in the thermally evaporated inorganic bilayer is expected as a result from the structural analysis, considering the absence of any annealing treatment to diffuse the small amount of Cs^+ ad Br^- throughout the thin-film thickness and the penetration depth of the X-ray analysis Section 3.5.3. Indeed, only the thick PbI_2 layer evaporated on top the thin CsBr one (see Table 5.12) can be seen in the XRD pattern. Interestingly, considering the information that can be found in the literature and the overall low intensity of the PbI_2 peaks in the XRD diffraction pattern compared to the background signal of the glass substrate, the typical morphology taken by the hexagonal PbI_2 crystals in forming the thermally evaporated inorganic bilayer is based on plate-like crystals and small grains. These create a porous CsBr/PbI_2 scaffold for the infiltration and interdiffusion reaction of the spin-coated organic solution during the next step of the hybrid process [70, 108].

Wettability and Reactivity

In terms of wettability and reactivity of the thermally evaporated inorganic layer, several experiments need to be carried out before achieving the conversion into a sufficiently stable PVK thin-film. Given that thin-films deposited by thermal evaporation are generally homogeneous and uniform, no particular problems of wettability have been are noticed. In fact, the only visible halo is the oval one inherent to the spin coating process itself (see Section 5.1.1) and no sign of the droplets of organic solution can be noted, as shown in Fig. 5.16. Interestingly, after dripping the organic solution of FAI in IPA, the inorganic layer is not immediately

converted into an intermediate PVK phase, turning into a light brown colour as the two-step spin-coated PVK thin-films. Completely in contrast with the two-step spin coating reaction mechanism, the inorganic layer retains its yellowish colour until annealing, which activates the interdiffusion reaction between the PVK precursors. After the annealing treatment, the layer is thus completely converted into a compact and uniform PVK thin-films.

Figure 5.16: Photograph of the hybrid PVK thin-film showing the oval halo due to the spreading of the organic solution during spin coating on the inorganic bilayer of PbI_2/CsBr.

5.2.2. Spin Coating of the Organic Solution

After the structural analysis of the inorganic bilayer of PbI_2/CsBr deposited by thermal evaporation, the second development step focuses on the investigation of the spin coating of the organic solution of FAI in IPA on it. The spin coating processing parameters used in this second development stage and derived from the preliminary study in Section 5.1 are shown in Table 5.13.

Table 5.13: Processing parameters related to the spin coating of organic solution step in the synthesis of thermal evaporation/spin coating hybrid PVK thin-films.

Sample	**Drying (CsBr+PbI_2)**	**V_{FAI} (μL)**	**M_{FAI} (mol/L)**	**Annealing (PVK)**
Hybrid	t=10 min	120	$0.469 \cdot 10^{-3}$	T=135 °C - t=15 min

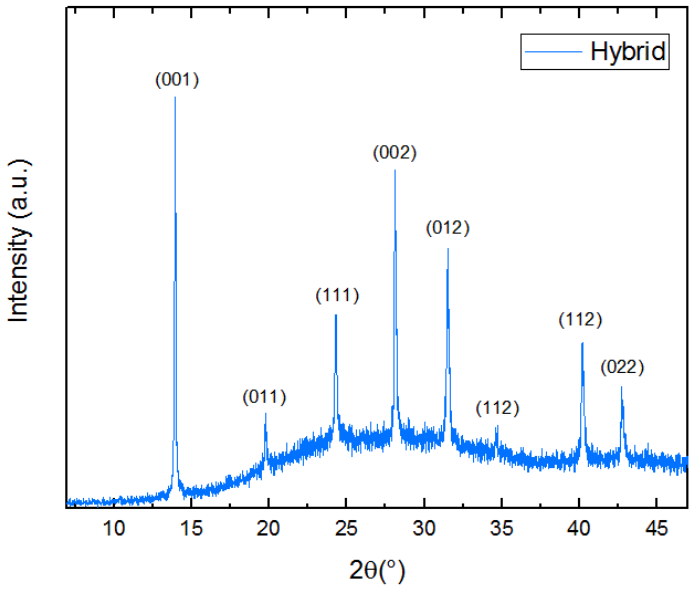

Figure 5.17: XRD diffractogram of the thermally evaporated/spin coating hybrid PVK thin-film. The family of lattice planes that are indicated in the XRD pattern refer to the cubic α-phase of PVK. The background signal measured in the range 2θ=20-40° derives from the glass substrate.

The XRD diffractogram of the hybrid PVK thin-film that has been developed in this MSc Thesis Project can be seen in Fig. 5.17. All XRD peaks shown by the PVK thin-film correspond to the cubic α phase of PVK [48] and no other phases are identified, revealing the excellent homogeneity of the hybrid PVK thin-film in

comparison to the two-step spin-coated ones shown in Section 5.1. In detail, the first (001) peak is located around 2θ=13.95°, while the second (002) peak is placed at about 2θ=28.11° [19, 119, 122]. Considering the XRD peaks position, the composition of this PVK is $Cs_xFA_{1-x}PbI_{3-x}Br_x$ and a low content of Cs^+ and Br^- of x<0.1 is expected, taking into account the set processing parameters for the inorganic bilayer thermal evaporation step. The XRD PVK peaks are sharp ad narrow, demonstrating the high level of crystallinity and the low defect density of the cubic α-PVK phase present in the PVK thin-film. However, the overall low intensity of the XRD peaks with respect to the background signal of the glass substrate suggests a low amount of crystalline material. Therefore, it is assumed that the inorganic layer is not completely converted to PVK after spin coating of the organic solution. However, despite this conjecture, more experiments and measurements are needed to confirm these observations.

The optical properties and the bandgap of the hybrid PVK thin-film are shown in Fig. 5.18 and Table 5.14.

As it can be observed in Fig. 5.18(A), the PVK thin-film shows a good absorption profile as the two-step spin-coated ones (see Section 5.1.2), especially when imagining a monolithic PVK/Si tandem application. Indeed, it presents high absorption (A~70%) for blue-light wavelengths ($\lambda \lesssim$<500 nm) and low absorption for green-, yellow- and red-light wavelengths ($\lambda \gtrsim$500 nm). Moreover, the fairly sharp absorption onset is in line with the aforementioned high level crystallinity of the formed photoactive cubic α-phase of PVK formed by the hybrid synthesis technique. On the other side, the reflection (Fig. 5.18(B)) stays around R~20-24% for the whole range of wavelengths considered. Finally, the bandgap equal to E_g~1.53 eV confirms, as expected from the thermal evaporation processing parameters and the XRD PVK peaks position, the presence of a quite low content of Cs^+ and Br^- of x<0.1. Further tuning through PVK engineering is necessary to increase the bandgap in future research for a 2-T PVK-Si tandem application.

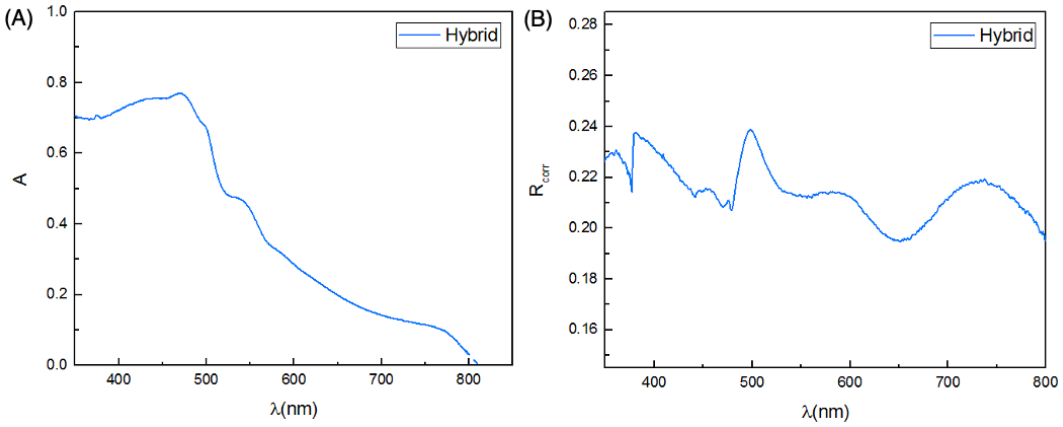

Figure 5.18: UV-Vis-NIR measurements showing the (A) absorptance and (B) reflectance spectra of the thermally evaporated/spin coating hybrid PVK thin-film. The absorptance spectra have not been corrected by subtracting the absorption of the glass substrates as it is close to A=0% for both. The reflectance spectra have been corrected considering the reflection of the glass substrate, around R~9-10%. The dashed line prolonging the absorption spectra is present as a guide to the eye to mark the absorption onset and its intercept with the x-axis, related to the bandgap, as the information is missing due to erroneous measurement settings.

Table 5.14: Bandgap values of the hybrid PVK thin-film, calculated from the absorptance spectra.

Sample	**E_g (eV)**
Hybrid	1.53

Thickness Estimation

By considering similar studies found in the literature [70, 128, 136], the expected thickness of the hybrid PVK thin-film after spin coating of the organic solution is shown in Eq. (34):

$$t_{PVK} \sim 1.8 \div 2.0 \cdot t_{PbI_2/CsBr} \tag{34}$$

Where t_{PVK} is the final thickness of the hybrid PVK thin-film and $t_{PbI_2/CsBr}$ is the thickness of the initial thermally evaporated inorganic bilayer.

Thus, since the hybrid PVK thin-film seems to approximately double in thickness from the thermal evaporation of the inorganic bilayer to the spin coating of the organic solution, it is possible to estimate its final thickness, as it can be seen in Eq. (35):

$$t_{PVK} \sim 1.8 \cdot t_{PbI_2/CsBr} = 1.8 \cdot t_{PbI_2} \cdot TF \qquad (nm) \tag{35}$$

Ignoring the contribution to the thickness of the CsBr thin layer of only t_{CsBr}=18 nm and considering only the evaporation of a layer of PbI_2 of t_{PbI_2}=360 nm and a tooling factor of TF~0.653 of the resulting PVK, as described in Section 4.2.1, the expected final thickness of the hybrid PVK thin-film is approximately t_{PVK}~423 nm.

As a final remark, it should be highlighted that the surface of the hybrid PVK thin-film looks reasonably uniform and smooth thanks to the characteristics of the inorganic bilayer deposited by thermal evaporation.

In closing, the thermal evaporation/spin coating hybrid synthesis technique allows to produce homogeneous PVK thin-films showing the presence of highly crystalline ideal cubic α phase of PVK of composition $Cs_xFA_{1-x}PbI_{3-x}Br_x$ with a low content of Cs^+ and Br^- of x<0.1. However, incomplete conversion of the thin-film to PVK is suspected. Moreover, the PVK thin-films surface appears quite uniform and smooth. The uniform surface coverage and the absorption and reflection properties look promising for a monolithic PVK/Si tandem application, even though further PVK engineering studies are required for optimising the bandgap.

5.2.3. Annealing

The resulting PVK thin-film is annealed at T=135 °C for t=15 min. These annealing parameters have been chosen after comparing different annealing treatments found in the literature, which have been performed on similar thermal evaporation/spin coating hybrid PVK thin-films [70, 108, 137]. Optimisation of such annealing parameters is needed to obtain high-quality hybrid PVK thin-films.

6

Conclusions and Recommendations

6.1. Conclusions

The herein MSc Thesis Project focuses on the development of PVK absorber layers synthesised by techniques compatible with non-flat substrates, starting from the guidelines of the experimental methods presented in the literature. Five main objectives are pursued. The main conclusions that can be drawn from this MSc Thesis Project are:

- **Thermal evaporation synthesis** The main conclusions drawn from the optimisation process are:
  1. Multisource layer-by-layer thermal evaporation allows to synthesise high-quality multications mixed-halides PVK thin-films of composition $Cs_xFA_{1-x}PbI_{3-x}Br_x$ (x~0.16-0.17);
  2. The thermally evaporated PVK thin-films show valuable properties in terms of crystallinity, homogeneity, absorption (A≤60% for $\lambda \lesssim 500$ nm and $\alpha \sim 10^4$-10^5 cm^{-1}) and thickness uniformity, while the small average grain size might hamper the charge carriers transport and facilitate the PVK degradation;
  3. The best annealing parameters are T=100 °C and t=30 min;
  4. It is possible to obtain highly crystalline and homogeneous cubic α phase PVK thin-films, even though the synthesis technique presents some limitations in the control of composition of PVK, an aspect that can potentially lead to the occurrence of degradation phenomena;
  5. The bandgap tuning leads to E_g~1.60 eV, which is close to the optimal bandgap range for a monolithic PVK/Si tandem application, although it needs to be further optimised to obtain current matching.
- **Thermal evaporation/spin coating hybrid synthesis** The main conclusions drawn from the development process are:
  1. The thermal/evaporation hybrid synthesis technique, which have been developed on the basis of a preliminary study on two-step spin-coating, enables the production of PVK thin-films of composition $Cs_xFA_{1-x}PbI_{3-x}Br_x$ with a low content of Cs^+ and Br^- (x<0.1), which can be adjusted by controlling the thermal evaporation deposition parameters of the inorganic PVK precursors layer;
  2. The analysis of the wettability properties of the inorganic layer and interdiffusion reaction between the PVK precursors for the two-step spin coating synthesis technique allows to individuate the optimal spun volume (V_{FAI}=120 μL) and concentration (M_{FAI}= $0.469 \cdot 10^{-3}$ mol/L) of the organic PVK precursor solution, so that the resulting hybrid PVK thin-films achieve excellent crystallinity and homogeneity, good absorption properties (A~70% for $\lambda \lesssim 500$ nm) and their surface appears quite uniform and smooth;
  3. For the two-step spin-coated PVK thin-films process, the optimal annealing parameters are T=100 °C and t=30 min;
  4. Albeit the incomplete conversion to PVK is suspected, an highly crystalline and homogeneous cubic α phase of PVK can be obtained;

5. The achieved bandgap is only E_g~1.53 eV, thus it must be increased to enter in the optimal bandgap range for a monolithic PVK/Si tandem application.

In conclusion, the PVK engineering concepts applied to both thermally evaporated and thermal evaporation/spin coating hybrid $Cs_xFA_{1-x}PbI_{3-x}Br_x$ thin-films has lead to synthesise PVK thin-films that, in spite of the necessary further optimisation, looks promising for the deposition on non-flat substrates, e.g. on the randomly distributed microsized pyramids texture of a c-Si solar cell to fabricate a monolithic PVK/Si tandem solar cell.

6.2. Recommendations for Future Work

Further research is necessary to develop and optimise thermal evaporation and thermal evaporation/spin coating hybrid techniques in order to obtain high-quality large-area fully-textured PSCs for monolithic PVK/Si tandem applications. PVK engineering is an open field of research. In terms of compositional engineering, particular attention should be paid to the effect of content of Cs^+ and Br^- on the structural stability in atmospheric conditions to avoid PVK degradation and charge-carrier dynamics and transport. The latter may be studied with more precision by the mean of characterisation techniques as time-resolved photoluminescence (TRPL) and time-resolved microwave conductivity (TRMC). Considering bandgap tuning, the content of Cs^+ and Br^- should be optimised to achieve bandgaps in the range E_g~1.65-1.73 eV for monolithich PVK/Si tandem applications, aiming to superior V_{oc} and bandgap utilisation.

Taking into account the optimisation of multisource layer-by-layer thermal evaporation synthesis technique, thermal evaporation has been found to lead to PVK thin-films with a smaller average grain size compared to other synthesis techniques. When such absorber layer is applied to a PSC, it might reduce the charge-carrier mobility and contribute to their recombination. Therefore, the effect of the substrate properties on the grain growth and morphology of the PVK should be under investigation, aiming to structures (e.g. large grains, preferential crystal orientation, compact and dense layer and uniform surface) favouring high charge carriers mobilities and lifetimes. In addition to this, potential passivation methods can be studied for reducing the density of the interface defects which create between the PVK and the transport layers, causing charge-carrier recombination. This would also improve the resistance of the PSC to degradation. Furthermore, it is recommended to optimise (increase) the thicknesses of the individual layers of CsBr, PbI_2 and FAI and the total PVK thin-film thickness, to sort out the composition discrepancies from one deposition batch to another may and to observe the change in the optical properties in a thicker PVK absorber layer.

In reference to the development of thermal evaporation/spin coating hybrid synthesis technique, further experiments should focus on analysing more in depth the causes behind the problems of wettability and reactivity of the inorganic layer of CsBr and PbI_2, observing the material properties through characterisation techniques as UV-Vis-NIR, profilometry, X-ray photoelectron spectroscopy (XPS) and SEM. Furthermore, the combination of in situ measurements via grazing-incidence wide-angle X-ray scattering (GIWAXS) and photoluminescence (PL) would allow to better understand the crystallisation dynamics of the PVK thin-films by looking at the structural intermediates and transformation kinetics. This would help in the optimisation of the organic solution concentration and the annealing parameters. Moreover, a study of the average grain size and morphology together with the PVK thin-film charge carriers transport properties would be particularly interesting. Similarly to thermally evaporated PVK thin-films, the effect of different substrates on the crystals growth mode should be analysed. In fact, in relation to PSCs manufacturing, the deposition of PVK on the TCO/HTL layer might change its composition, crystallisation mechanism and grains dimension and morphology. SEM analysis could also be applied to observe the surface features and properties of the hybrid PVK thin-films. Lastly, the final thickness of the absorber layer must be optimised for application in a PSC.

Then, it is recommended to test the deposition of PVK on non-flat surfaces, as the characteristics of the final PVK thin-film might differ depending on the PVK synthesis technique.

Lastly, in relation to the full PSC and regardless of the synthesis technique, the thickness of the PVK absorber layer should be optimised in relation to the neighbouring transport layers thickness to achieve the best possible optoelectronic properties. Finally, optical simulations of the complete PSC can be performed to reduce thermalization and reflection losses.

In closing, it should be pointed out that PSCs have not reached the PV market yet, but thanks to the enormous research effort focusing on PVK and its applications in the field of solar energy, their commercialization can be envisage in the coming years as an actual alternative to the classic c-Si-based solar cells.

A

Appendix - UV-Vis-NIR Absorptance and Reflectance Spectra of Glass

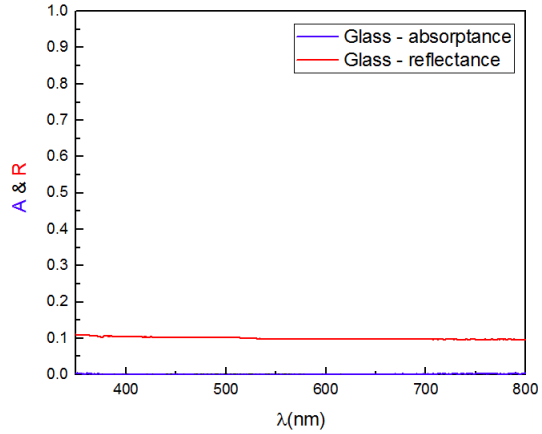

Figure A.1: UV-Vis-NIR absorptance and reflectance spectra for glass. Its contribution needs to be subtracted from the optical properties measurements of PVK thin-films deposited on glass substrates. The absorptance of glass is around A=0% for all the range of wavelengths of interest (350 nm< λ <800 nm), while the reflectance stays around R=9-10%.

B

Appendix - Development of Two-step Spin Coating Synthesis Technique - Step 1

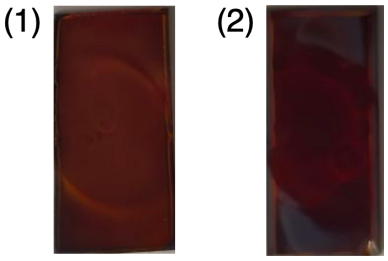

Figure B.1: Photographs of PVK thin-films presenting either (1) brown or (2) red colour synthesised by two-step spin coating, showing their differences in homogeneity and uniformity. Sample (1) looks quite homogeneous and uniform, while sample (2) clearly shows circular halos in the central zone where the droplets of the organic solution of FAI in IPA have been deposited on the inorganic layer of composition $CsPbI_{3-x}Br_x$. The processing parameters that are modified in the two-step spin coating process of these PVK thin-films with respect to those presented in Section 3.4.2 can be seen in Table B.1.

Table B.1: Processing parameters that are modified in the two-step spin coating process with respect to those presented in Section 3.4.2, which leads to PVK thin-films showing either brown or red colour. Both samples are annealed at T=100 °C for t=30 min.

Sample	**Drying (CsBr+PbI_2)**	**$V_{CsBr+Pb_2}$=V_{FAI} (μL)**	**M_{FAI} (mol/L)**
(1)	t=10 min	80	$0.389 \cdot 10^{-3}$
(2)	-	80	$0.389 \cdot 10^{-3}$

C

Appendix - Development of Two-step Spin Coating Synthesis Technique - Step 2

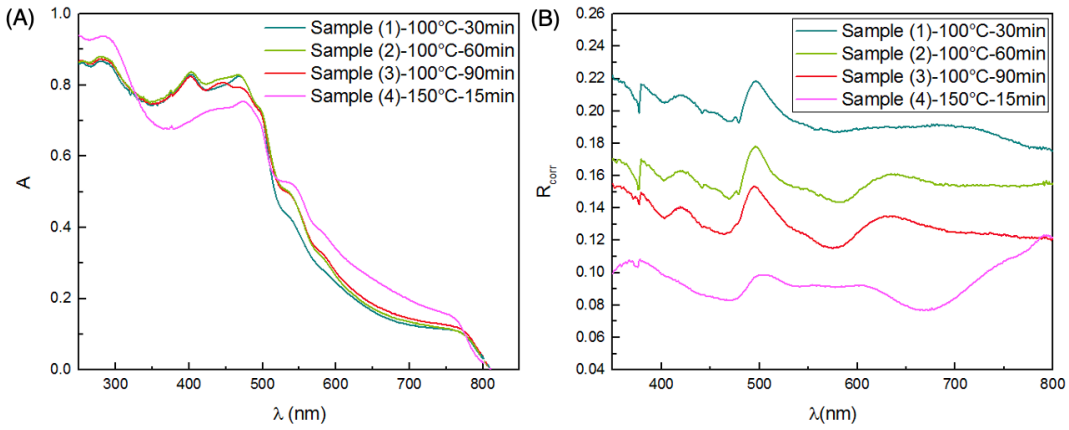

Figure C.1: UV-Vis-NIR measurements from the annealing stage of the development of the two-step spin coating synthesis technique. The (A) absorptance and (B) reflectance spectra of sample (1) (T=100 °C for t=30 min), sample (2) ((T=100 °C for t=60 min)), sample (3) ((T=100 °C for t=90 min)) and sample (4) (T=150 °C for t=15 min) are shown. All samples are characterised by the drying stage of the inorganic layer, spun volume of organic solution V_{FAI}=120 μL and concentration M_{FAI}= 0.469 · 10^{-3} mol/L. The absorptance spectra have not been corrected by subtracting the absorption of the glass substrates as it is close to A=0% for both. The reflectance spectra have been corrected considering the reflection of the glass substrate, around R~9-10%. The dashed line prolonging the absorption spectra is present as a guide to the eye to mark the absorption onset and its intercept with the x-axis, related to the bandgap, as the information is missing due to erroneous measurement settings.

Table C.1: Bandgap evaluation (calculated from the absorptance spectra) of samples from the annealing stage of the development of the two-step spin coating synthesis technique. The bandgaps of sample (1) (T=100 °C for t=30 min), sample (2) ((T=100 °C for t=60 min)), sample (3) ((T=100 °C for t=90 min)) and sample (4) (T=150 °C for t=15 min) are shown. All samples are characterised by the drying stage of the inorganic layer, spun volume of organic solution V_{FAI}=120 μL and concentration M_{FAI}= 0.469 · 10^{-3} mol/L.

Sample	**E_g (eV)**
(1)	1.53
(2)	1.53
(3)	1.53
(4)	1.53

Table C.2: Thickness measurements of sample (1) (T=100 °C for t=30 min), sample (2) ((T=100 °C for t=60 min)), sample (3) ((T=100 °C for t=90 min)) and sample (4) (T=150 °C for t=15 min). All samples are characterised by the drying stage of the inorganic layer, spun volume of organic solution V_{FAI}=120 μL and concentration M_{FAI}= 0.469 · 10^{-3} mol/L.

Sample	**Average thickness 1 (nm)**	**Average thickness 2 (nm)**	**Average thickness (nm)**
(1)	382.34	372.00	377.17
(2)	386.25	430.79	408.52
(3)	381.78	402.80	392.29
(4)	367.17	371.39	369.28

Bibliography

[1] BP plc. (2020). Statistical Review of World Energy. 66. https://www.bp.com/content/dam/bp/business-sites/en/global/corporate/pdfs/energy-economics/statistical-review/bp-stats-review-2020-full-report.pdf

[2] Wojciechowski, K., Forgács, D., Rivera, T. (2019). Industrial Opportunities and Challenges for Perovskite Photovoltaic Technology. Solar RRL, 3(9), 1–9. https://doi.org/10.1002/solr.201900144

[3] Anaya, M., Lozano, G., Calvo, M. E., Míguez, H. (2017). ABX_3 Perovskites for Tandem Solar Cells. Joule, 1(4), 769–793. https://doi.org/10.1016/j.joule.2017.09.017

[4] IEA. (2021). Net Zero by 2050: A Roadmap for the Global Energy Sector. 222. https://iea.blob.core.windows.net/assets/ad0d4830-bd7e-47b6-838c-40d115733c13/NetZeroby2050-ARoadmapfortheGlobalEnergySector.pdf

[5] Thomas, S., Thankappan, A. (2018). Perovskite photovoltaics: Basic to advanced concepts and implementation. Perovskite Photovoltaics: Basic to Advanced Concepts and Implementation. https://doi.org/10.1016/C2016-0-03790-7

[6] Fraunhofer Institute for Solar Energy Systems (ISE). (2021, July). Photovoltaics Report. https://www.ise.fraunhofer.de/content/dam/ise/de/documents/publications/studies/Photovoltaics-Report.pdf

[7] National Renewable Energy Laboratory. (2020). NREL Best Research-Cell Efficiencies. https://www.nrel.gov/pv/assets/pdfs/best-research-cell-efficiencies.20200128.pdf.

[8] Yoshikawa, K., Kawasaki, H., Yoshida, W., Irie, T., Konishi, K., Nakano, K., Uto, T., Adachi, D., Kanematsu, M., Uzu, H., Yamamoto, K. (2017). Silicon heterojunction solar cell with interdigitated back contacts for a photoconversion efficiency over 26%. Nature Energy, 2(5). https://doi.org/10.1038/nenergy.2017.32

[9] Werner, J., Weng, C. H., Walter, A., Fesquet, L., Seif, J. P., De Wolf, S., Niesen, B., Ballif, C. (2016). Efficient Monolithic Perovskite/Silicon Tandem Solar Cell with Cell Area > 1 cm^2. Journal of Physical Chemistry Letters, 7(1), 161–166. https://doi.org/10.1021/acs.jpclett.5b02686

[10] Richter, A., Hermle, M., Glunz, S. W. (2013). Reassessment of the limiting efficiency for crystalline silicon solar cells. IEEE journal of photovoltaics, 3(4), 1184-1191. https://doi.org/ 10.1109/JPHOTOV.2013.2270351

[11] Energie, H. B. F. M. U. (2021, November 22). World record again at HZB: Almost 30% efficiency for next-generation tandem solar cells. HZB Website. https://www.helmholtz-berlin.de/pubbin/news_seite?nid=23248;sprache=en;seitenid=1

[12] Zhu, P., Zhu, J. (2020). Low-dimensional metal halide perovskites and related optoelectronic applications. InfoMat (Vol. 2, Issue 2). https://doi.org/10.1002/inf2.12086

[13] Smets, A., Jäger, K., Isabella, O., Swaaij van, R., Zeman, M. (2016). Solar Energy: The Physics and Engineering of Photovoltaic Conversion Technologies and Systems. UIT Cambridge Ltd.

[14] Wilson, B. (2020, November 11). Perovskites – the best material you've never heard of. TheGIST - The Glasgow Insight into Science and Technology. https://the-gist.org/2020/01/perovskites-best-material-youve-never-heard-of/

[15] Philippe, B., Jacobsson, T. J., Correa-Baena, J. P., Jena, N. K., Banerjee, A., Chakraborty, S., Cappel, U. B., Ahuja, R., Hagfeldt, A., Odelius, M., Rensmo, H. (2017). Valence Level Character in a Mixed Perovskite Material and Determination of the Valence Band Maximum from Photoelectron Spectroscopy: Variation with Photon Energy. Journal of Physical Chemistry C, 121(48), 26655–26666. https://doi.org/10.1021/acs.jpcc.7b08948

[16] Brenner, T. M., Egger, D. A., Kronik, L., Hodes, G., Cahen, D. (2016). Hybrid organic - Inorganic perovskites: Low-cost semiconductors with intriguing charge-transport properties. Nature Reviews Materials, 1(1), 1–16. https://doi.org/10.1038/natrevmats.2015.7

[17] Sadhanala, A., Deschler, F., Thomas, T. H., Dutton, S. E., Goedel, K. C., Hanusch, F. C., ... Friend, R. H. (2014). Preparation of single-phase films of $CH_3NH_3Pb(I_{1-x}Br_x)_3$ with sharp optical band edges. The Journal of Physical Chemistry Letters, 5(15), 2501-2505. https://doi-org.tudelft.idm.oclc.org/10.1021/jz501332v

[18] De Wolf, S., Holovsky, J., Moon, S. J., Löper, P., Niesen, B., Ledinsky, M., Haug, F. J., Yum, J. H., Ballif, C. (2014). Organometallic halide perovskites: Sharp optical absorption edge and its relation to photovoltaic performance. Journal of Physical Chemistry Letters, 5(6), 1035–1039. https://doi.org/10.1021/jz500279b

[19] Gil-Escrig, L., Momblona, C., La-Placa, M. G., Boix, P. P., Sessolo, M., Bolink, H. J. (2018). Vacuum Deposited Triple-Cation Mixed-Halide Perovskite Solar Cells. Advanced Energy Materials, 8(14), 1–6. https://doi.org/10.1002/aenm.201703506

[20] Werner, J., Nogay, G., Sahli, F., Yang, T. C. J., Bräuninger, M., Christmann, G., Walter, A., Kamino, B. A., Fiala, P., Löper, P., Nicolay, S., Jeangros, Q., Niesen, B., Ballif, C. (2018). Complex Refractive Indices of Cesium-Formamidinium-Based Mixed-Halide Perovskites with Optical Band Gaps from 1.5 to 1.8 eV. ACS Energy Letters, 3(3), 742–747. https://doi.org/10.1021/acsenergylett.8b00089

[21] Momblona, C., Malinkiewicz, O., Roldán-Carmona, C., Soriano, A., Gil-Escrig, L., Bandiello, E., Scheepers, M., Edri, E., Bolink, H. J. (2014). Efficient methylammonium lead iodide perovskite solar cells with active layers from 300 to 900 nm. APL Materials, 2(8). https://doi.org/10.1063/1.4890056

[22] Liu, Z., Sofia, S. E., Laine, H. S., Woodhouse, M., Wieghold, S., Peters, I. M., Buonassisi, T. (2020). Revisiting thin silicon for photovoltaics: A technoeconomic perspective. Energy and Environmental Science, 13(1), 12–23. https://doi.org/10.1039/c9ee02452b

[23] Ponseca, C. S., Abdellah, M., Zheng, K., Yartsev, A., Pascher, T., Harlang, T., Chabera, P., Pullerits, T., Stepanov, A., Wolf, J. P., Sundström, V. (2014). Ultrafast charge generation, high and balanced charge carrier mobilities in organo halide perovskite solar cell. Optics InfoBase Conference Papers. https://doi.org/10.1364/up.2014.08.tue.e.1

[24] Galkowski, K., Mitioglu, A., Miyata, A., Plochocka, P., Portugall, O., Eperon, G. E., Wang, J. T. W., Stergiopoulos, T., Stranks, S. D., Snaith, H. J., Nicholas, R. J. (2016). Determination of the exciton binding energy and effective masses for methylammonium and formamidinium lead tri-halide perovskite semiconductors. Energy and Environmental Science, 9(3), 962–970. https://doi.org/10.1039/c5ee03435c

[25] Chen, X., Lu, H., Yang, Y., Beard, M. C. (2018). Excitonic Effects in Methylammonium Lead Halide Perovskites. Journal of Physical Chemistry Letters, 9(10), 2595–2603. https://doi.org/10.1021/acs.jpclett.8b00526

[26] Brenner, T. M., Egger, D. A., Rappe, A. M., Kronik, L., Hodes, G., Cahen, D. (2015). Are Mobilities in Hybrid Organic-Inorganic Halide Perovskites Actually "high"? Journal of Physical Chemistry Letters, 6(23), 4754–4757. https://doi.org/10.1021/acs.jpclett.5b02390

[27] Giorgi, G., Fujisawa, J. I., Segawa, H., Yamashita, K. (2013). Small photocarrier effective masses featuring ambipolar transport in methylammonium lead iodide perovskite: A density functional analysis. Journal of Physical Chemistry Letters, 4(24), 4213–4216. https://doi.org/10.1021/jz4023865

[28] Chang, Y. H., Park, C. H., Matsuishi, K. (2004). First-principles study of the structural and the electronic properties of the lead-halide-based inorganic-organic perovskites $(CH_3NH_3)PbX_3$ and $CsPbX_3$ (X = Cl, Br, I). Journal of the Korean Physical Society, 44(4), 889–893.

[29] Maynard, B., Long, Q., Schiff, E. A., Yang, M., Zhu, K., Kottokkaran, R., Abbas, H., Dalal, V. L. (2016). Electron and hole drift mobility measurements on methylammonium lead iodide perovskite solar cells. Applied Physics Letters, 108(17), 1–5. https://doi.org/10.1063/1.4948344

[30] Liu, X., Xu, M., Hao, Y., Fu, J., Wang, F., Zhang, B., Bennett, S., Sellin, P., Jie, W., Xu, Y. (2021). Solution-Grown Formamidinium Hybrid Perovskite (FAPbBr3) Single Crystals for -Particle and -Ray Detection at Room Temperature. ACS Applied Materials and Interfaces, 13(13), 15383–15390. https://doi.org/10.1021/acsami.1c00174

[31] Gélvez-Rueda, M. C., Renaud, N., Grozema, F. C. (2017). Temperature Dependent Charge Carrier Dynamics in Formamidinium Lead Iodide Perovskite. Journal of Physical Chemistry C, 121(42), 23392–23397. https://doi.org/10.1021/acs.jpcc.7b09303

[32] Zhu, X. Y., Podzorov, V. (2015). Charge Carriers in Hybrid Organic-Inorganic Lead Halide Perovskites Might Be Protected as Large Polarons. Journal of Physical Chemistry Letters, 6(23), 4758–4761. https://doi.org/10.1021/acs.jpclett.5b02462

[33] Herz, L. M. (2017). Charge-Carrier Mobilities in Metal Halide Perovskites: Fundamental Mechanisms and Limits. ACS Energy Letters, 2(7), 1539–1548. https://doi.org/10.1021/acsenergylett.7b00276

[34] Ma, J., Wang, L. W. (2017). The Nature of Electron Mobility in Hybrid Perovskite $CH_3NH_3PbI_3$. Nano Letters, 17(6), 3646–3654. https://doi.org/10.1021/acs.nanolett.7b00832

[35] Rehman, W., McMeekin, D. P., Patel, J. B., Milot, R. L., Johnston, M. B., Snaith, H. J., Herz, L. M. (2017). Photovoltaic mixed-cation lead mixed-halide perovskites: Links between crystallinity, photo-stability and electronic properties. Energy and Environmental Science, 10(1), 361–369. https://doi.org/10.1039/c6ee03014a

[36] Liu, Z., Krückemeier, L., Krogmeier, B., Klingebiel, B., Márquez, J. A., Levcenko, S., Öz, S., Mathur, S., Rau, U., Unold, T., Kirchartz, T. (2019). Open-Circuit Voltages Exceeding 1.26 v in Planar Methylammonium Lead Iodide Perovskite Solar Cells. ACS Energy Letters, 4(1), 110–117. https://doi.org/10.1021/acsenergylett.8b01906

[37] Kirchartz, T. (2019). High Open-Circuit Voltages in Lead-Halide Perovskite Solar Cells: Experiment, Theory and Open Questions. Philosophical Transactions of the Royal Society A, 377(2152). https://doi-org.tudelft.idm.oclc.org/10.1098/rsta.2018.0286

[38] Augusto, A., Herasimenka, S. Y., King, R. R., Bowden, S. G., Honsberg, C. (2017). Analysis of the recombination mechanisms of a silicon solar cell with low bandgap-voltage offset. Journal of Applied Physics, 121(20). https://doi.org/10.1063/1.4984071

[39] Yin, W. J., Shi, T., Yan, Y. (2014). Unique properties of halide perovskites as possible origins of the superior solar cell performance. Advanced Materials, 26(27), 4653–4658. https://doi.org/10.1002/adma.201306281

[40] Castro-Mendez, A. F., Hidalgo, J., Correa-Baena, J. P. (2019). The Role of Grain Boundaries in Perovskite Solar Cells. Advanced Energy Materials, 9(38), 1–10. https://doi.org/10.1002/aenm.201901489

[41] Sato, T., Takagi, S., Deledda, S., Hauback, B. C., Orimo, S. I. (2016). Extending the applicability of the Goldschmidt tolerance factor to arbitrary ionic compounds. Scientific Reports, 6(March), 1–10. https://doi.org/10.1038/srep23592

[42] Capitani, F., Marini, C., Caramazza, S., Postorino, P., Garbarino, G., Hanfland, M., Pisanu, A., Quadrelli, P., Malavasi, L. (2016). High-pressure behavior of methylammonium lead iodide (MAPbI3) hybrid perovskite. Journal of Applied Physics, 119(18). https://doi.org/10.1063/1.4948577

[43] Szafrański, M., Katrusiak, A. (2017). Photovoltaic Hybrid Perovskites under Pressure. Journal of Physical Chemistry Letters, 8(11), 2496–2506. https://doi.org/10.1021/acs.jpclett.7b00520

[44] Masi, S., Gualdrón-Reyes, A. F., Mora-Seró, I. (2020). Stabilization of Black Perovskite Phase in FAPbI3and CsPbI3. ACS Energy Letters, 5(6), 1974–1985. https://doi.org/10.1021/acsenergylett.0c00801

[45] Gholipour, S., Saliba, M. (2019). Bandgap tuning and compositional exchange for lead halide perovskite materials. Characterization Techniques for Perovskite Solar Cell Materials. Elsevier Inc. https://doi.org/10.1016/B978-0-12-814727-6.00001-3

[46] Saliba, M., Matsui, T., Seo, J. Y., Domanski, K., Correa-Baena, J. P., Nazeeruddin, M. K., Zakeeruddin, S. M., Tress, W., Abate, A., Hagfeldt, A., Grätzel, M. (2016). Cesium-containing triple cation perovskite solar cells: Improved stability, reproducibility and high efficiency. Energy and Environmental Science, 9(6), 1989–1997. https://doi.org/10.1039/c5ee03874j

[47] Eperon, G. E., Stranks, S. D., Menelaou, C., Johnston, M. B., Herz, L. M., Snaith, H. J. (2014). Formamidinium lead trihalide: A broadly tunable perovskite for efficient planar heterojunction solar cells. Energy and Environmental Science, 7(3), 982–988. https://doi.org/10.1039/c3ee43822h

[48] Ji, R., Zhang, Z., Cho, C., An, Q., Paulus, F., Kroll, M., Löffler, M., Nehm, F., Rellinghaus, B., Leo, K., Vaynzof, Y. (2020). Thermally evaporated methylammonium-free perovskite solar cells. Journal of Materials Chemistry C, 8(23), 7725–7733. https://doi.org/10.1039/d0tc01550d

[49] Lee, J. W., Kim, D. H., Kim, H. S., Seo, S. W., Cho, S. M., Park, N. G. (2015). Formamidinium and cesium hybridization for photo- and moisture-stable perovskite solar cell. Advanced Energy Materials, 5(20). https://doi.org/10.1002/aenm.201501310

[50] Yi, C., Luo, J., Meloni, S., Boziki, A., Ashari-Astani, N., Grätzel, C., Zakeeruddin, S. M., Röthlisberger, U., Grätzel, M. (2016). Entropic stabilization of mixed A-cation ABX3 metal halide perovskites for high performance perovskite solar cells. Energy and Environmental Science, 9(2), 656–662. https://doi.org/10.1039/c5ee03255e

[51] Kar, M., Körzdörfer, T. (2020). Computational high throughput screening of inorganic cation based halide perovskites for perovskite only tandem solar cells. Materials Research Express, 7(5). https://doi.org/10.1088/2053-1591/ab8c0d

[52] Fu, F., Feurer, T., Weiss, T. P., Pisoni, S., Avancini, E., Andres, C., Buecheler, S., Tiwari, A. N. (2017). High-efficiency inverted semi-transparent planar perovskite solar cells in substrate configuration. Nature Energy, 2(1). https://doi.org/10.1038/nenergy.2016.190

[53] Uddin, A., Upama, M. B., Yi, H., Duan, L. (2019). Encapsulation of organic and perovskite solar cells: A review. Coatings, 9(2), 1–17. https://doi.org/10.3390/coatings9020065

[54] Krishnan, U. (2019). Factors affecting the stability of perovskite solar cells: a comprehensive review. Journal of Photonics for Energy, 9(02), 1. https://doi.org/10.1117/1.jpe.9.021001

[55] Bush, K. A., Palmstrom, A. F., Yu, Z. J., Boccard, M., Cheacharoen, R., Mailoa, J. P., McMeekin, D. P., Hoye, R. L. Z., Bailie, C. D., Leijtens, T., Peters, I. M., Minichetti, M. C., Rolston, N., Prasanna, R., Sofia, S., Harwood, D., Ma, W., Moghadam, F., Snaith, H. J., ... McGehee, M. D. (2017). 23.6%-Efficient Monolithic Perovskite/Silicon Tandem Solar Cells With Improved Stability. Nature Energy, 2(4), 1–7. https://doi.org/10.1038/nenergy.2017.9

[56] Liu, D., Kelly, T. L. (2014). Perovskite solar cells with a planar heterojunction structure prepared using room-temperature solution processing techniques. Nature Photonics, 8(2), 133–138. https://doi.org/10.1038/nphoton.2013.342

[57] Sanehira, E. M., Tremolet De Villers, B. J., Schulz, P., Reese, M. O., Ferrere, S., Zhu, K., Lin, L. Y., Berry, J. J., Luther, J. M. (2016). Influence of Electrode Interfaces on the Stability of Perovskite Solar Cells: Reduced Degradation Using MoOx/Al for Hole Collection. ACS Energy Letters, 1(1), 38–45. https://doi.org/10.1021/acsenergylett.6b00013

[58] Jiang, Q., Zhang, L., Wang, H., Yang, X., Meng, J., Liu, H., Yin, Z., Wu, J., Zhang, X., You, J. (2017). Enhanced electron extraction using SnO2 for high-efficiency planar-structure HC(NH2)2 PbI3-based perovskite solar cells. Nature Energy, 2(1). https://doi.org/10.1038/nenergy.2016.177

[59] Wang, K., Shi, Y., Dong, Q., Li, Y., Wang, S., Yu, X., Wu, M., Ma, T. (2015). Low-temperature and solution-processed amorphous WOX as electron-selective layer for perovskite solar cells. Journal of Physical Chemistry Letters, 6(5), 755–759. https://doi.org/10.1021/acs.jpclett.5b00010

[60] Wang, L., Fu, W., Gu, Z., Fan, C., Yang, X., Li, H., Chen, H. (2014). Low temperature solution processed planar heterojunction perovskite solar cells with a CdSe nanocrystal as an electron transport/extraction layer. Journal of Materials Chemistry C, 2(43), 9087–9090. https://doi.org/10.1039/c4tc01875c

[61] Liu, J., Gao, C., Luo, L., Ye, Q., He, X., Ouyang, L., Guo, X., Zhuang, D., Liao, C., Mei, J., Lau, W. (2015). Low-temperature, solution processed metal sulfide as an electron transport layer for efficient planar perovskite solar cells. Journal of Materials Chemistry A, 3(22), 11750–11755. https://doi.org/10.1039/c5ta01200g

[62] Roß, M., Gil-Escrig, L., Al-Ashouri, A., Tockhorn, P., Jošt, M., Rech, B., Albrecht, S. (2020). Co-Evaporated p-i-n Perovskite Solar Cells beyond 20% Efficiency: Impact of Substrate Temperature and Hole-Transport Layer. ACS Applied Materials and Interfaces, 12(35), 39261–39272. https://doi.org/10.1021/acsami.0c10898

[63] Meng, L., You, J., Guo, T. F., Yang, Y. (2016). Recent Advances in the Inverted Planar Structure of Perovskite Solar Cells. Accounts of Chemical Research, 49(1), 155–165. https://doi.org/10.1021/acs.accounts.5b00404

[64] Luo, D., Yang, W., Wang, Z., Sadhanala, A., Hu, Q., Su, R., Shivanna, R., Trindade, G. F., Watts, J. F., Xu, Z., Liu, T., Chen, K., Ye, F., Wu, P., Zhao, L., Wu, J., Tu, Y., Zhang, Y., Yang, X., … Zhu, R. (2018). Enhanced photovoltage for inverted planar heterojunction perovskite solar cells. Science, 360(6396), 1442–1446. https://doi.org/10.1126/science.aap9282

[65] Jäger, K., Korte, L., Rech, B., Albrecht, S. (2017). Numerical optical optimization of monolithic planar perovskite-silicon tandem solar cells with regular and inverted device architectures. Optics Express, 25(12), A473. https://doi.org/10.1364/oe.25.00a473

[66] Zheng, X., Hou, Y., Bao, C., Yin, J., Yuan, F., Huang, Z., Song, K., Liu, J., Troughton, J., Gasparini, N., Zhou, C., Lin, Y., Xue, D. J., Chen, B., Johnston, A. K., Wei, N., Hedhili, M. N., Wei, M., Alsalloum, A. Y., … Bakr, O. M. (2020). Managing grains and interfaces via ligand anchoring enables 22.3%-efficiency inverted perovskite solar cells. Nature Energy, 5(2), 131–140. https://doi.org/10.1038/s41560-019-0538-4

[67] Momblona, C., Gil-Escrig, L., Bandiello, E., Hutter, E. M., Sessolo, M., Lederer, K., Blochwitz-Nimoth, J., Bolink, H. J. (2016). Efficient vacuum deposited p-i-n and n-i-p perovskite solar cells employing doped charge transport layers. Energy and Environmental Science, 9(11), 3456–3463. https://doi.org/10.1039/c6ee02100j

[68] Mazzarella, L., Lin, Y. H., Kirner, S., Morales-Vilches, A. B., Korte, L., Albrecht, S., Crossland, E., Stannowski, B., Case, C., Snaith, H. J., Schlatmann, R. (2019). Infrared Light Management Using a Nanocrystalline Silicon Oxide Interlayer in Monolithic Perovskite/Silicon Heterojunction Tandem Solar Cells with Efficiency above 25%. Advanced Energy Materials, 9(14), 1–9. https://doi.org/10.1002/aenm.201803241

[69] Santbergen, R., Uzu, H., Yamamoto, K., Zeman, M. (2019). Optimization of Three-Terminal Perovskite/Silicon Tandem Solar Cells. IEEE Journal of Photovoltaics, 9(2), 446–451. https://doi.org/10.1109/JPHOTOV.2018.2888832

[70] Sahli, F., Werner, J., Kamino, B. A., Bräuninger, M., Monnard, R., Paviet-Salomon, B., Barraud, L., Ding, L., Diaz Leon, J. J., Sacchetto, D., Cattaneo, G., Despeisse, M., Boccard, M., Nicolay, S., Jeangros, Q., Niesen, B., Ballif, C. (2018). Fully textured monolithic perovskite/silicon tandem solar cells with 25.2% power conversion efficiency. Nature Materials, 17(9), 820–826. https://doi.org/10.1038/s41563-018-0115-4

[71] Duong, T., Wu, Y. L., Shen, H., Peng, J., Fu, X., Jacobs, D., Wang, E. C., Kho, T. C., Fong, K. C., Stocks, M., Franklin, E., Blakers, A., Zin, N., McIntosh, K., Li, W., Cheng, Y. B., White, T. P., Weber, K., Catchpole, K. (2017). Rubidium Multication Perovskite with Optimized Bandgap for Perovskite-Silicon Tandem with over 26% Efficiency. Advanced Energy Materials, 7(14), 1–11. https://doi.org/10.1002/aenm.201700228

[72] Al-Ashouri, A., Köhnen, E., Li, B., Magomedov, A., Hempel, H., Caprioglio, P., Márquez, J. A., Vilches, A. B. M., Kasparavicius, E., Smith, J. A., Phung, N., Menzel, D., Grischek, M., Kegelmann, L., Skroblin, D., Gollwitzer, C., Malinauskas, T., Jošt, M., Matič, G., … Albrecht, S. (2020). Monolithic perovskite/silicon tandem solar cell with >29% efficiency by enhanced hole extraction. Science, 370(6522), 1300–1309. https://doi.org/10.1126/science.abd4016

[73] Richter, A., Benick, J., Feldmann, F., Fell, A., Hermle, M., Glunz, S. W. (2017). n-Type Si solar cells with passivating electron contact: Identifying sources for efficiency limitations by wafer thickness and resistivity variation. Solar Energy Materials and Solar Cells, 173(May), 96–105. https://doi.org/10.1016/j.solmat.2017.05.042

[74] Ehrler, B., Alarcón-Lladó, E., Tabernig, S. W., Veeken, T., Garnett, E. C., Polman, A. (2020). Photovoltaics reaching for the shockley-queisser limit. ACS Energy Letters, 5(9), 3029–3033. https://doi.org/10.1021/acsenergylett.0c01790

[75] Hörantner, M. T., Snaith, H. J. (2017). Predicting and optimising the energy yield of perovskite-on-silicon tandem solar cells under real world conditions. Energy and Environmental Science, 10(9), 1983–1993. https://doi.org/10.1039/c7ee01232b

[76] Jošt, M., Kegelmann, L., Korte, L., Albrecht, S. (2020). Monolithic Perovskite Tandem Solar Cells: A Review of the Present Status and Advanced Characterization Methods Toward 30% Efficiency. Advanced Energy Materials, 10(26). https://doi.org/10.1002/aenm.201904102

[77] Jäger, K., Sutter, J., Hammerschmidt, M., Schneider, P. I., Becker, C. (2021). Prospects of light management in perovskite/silicon tandem solar cells. Nanophotonics, 1599. https://doi.org/10.1515/nanoph-2020-0674

[78] PV Tech. (2021, February 6). Oxford PV pushes tandem SHJ/perovskite cell conversion efficiency to record 29.52%. https://www.pv-tech.org/oxford-pv-pushes-tandem-shj-perovskite-cell-conversion-efficiency-to-record-29-52/

[79] Fang, Z., Zeng, Q., Zuo, C., Zhang, L., Xiao, H., Cheng, M., Hao, F., Bao, Q., Zhang, L., Yuan, Y., Wu, W. Q., Zhao, D., Cheng, Y., Tan, H., Xiao, Z., Yang, S., Liu, F., Jin, Z., Yan, J., Ding, L. (2020). Perovskite-based tandem solar cells. Science Bulletin, 66(6), 621–636. https://doi.org/10.1016/j.scib.2020.11.006

[80] Niu, G., Guo, X., Wang, L. (2015). Review of recent progress in chemical stability of perovskite solar cells. Journal of Materials Chemistry A, 3(17), 8970–8980. https://doi.org/10.1039/c4ta04994b

[81] Li, Z., Yang, M., Park, J. S., Wei, S. H., Berry, J. J., Zhu, K. (2016). Stabilizing Perovskite Structures by Tuning Tolerance Factor: Formation of Formamidinium and Cesium Lead Iodide Solid-State Alloys. Chemistry of Materials, 28(1), 284–292. https://doi.org/10.1021/acs.chemmater.5b04107

[82] Akbulatov, A. F., Ustinova, M. I., Gutsev, L., Tsarev, S. A., Dremova, N. N., Zhidkov, I., Luchkin, S. Y., Ramachandran, B. R., Frolova, L., Kurmaev, E. Z., Stevenson, K. J., Aldoshin, S. M., Troshin, P. A. (2021). When iodide meets bromide: Halide mixing facilitates the light-induced decomposition of perovskite absorber films. Nano Energy, 86(April), 106082. https://doi.org/10.1016/j.nanoen.2021.106082

[83] Meng, Q., Chen, Y., Xiao, Y. Y., Sun, J., Zhang, X., Han, C. B., Gao, H., Zhang, Y., Yan, H. (2020). Effect of temperature on the performance of perovskite solar cells. Journal of Materials Science: Materials in Electronics, 32(10), 12784–12792. https://doi.org/10.1007/s10854-020-03029-y

[84] Back, H., Kim, G., Kim, J., Kong, J., Kim, T. K., Kang, H., Kim, H., Lee, J., Lee, S., Lee, K. (2016). Achieving long-term stable perovskite solar cells: Via ion neutralization. Energy and Environmental Science, 9(4), 1258–1263. https://doi.org/10.1039/c6ee00612d

[85] Wang, D., Wright, M., Elumalai, N. K., Uddin, A. (2016). Stability of perovskite solar cells. Solar Energy Materials and Solar Cells, 147, 255–275. https://doi.org/10.1016/j.solmat.2015.12.025

[86] Niu, G., Li, W., Meng, F., Wang, L., Dong, H., Qiu, Y. (2014). Study on the stability of CH3NH3PbI3 films and the effect of post-modification by aluminum oxide in all-solid-state hybrid solar cells. Journal of Materials Chemistry A, 2(3), 705–710. https://doi.org/10.1039/c3ta13606j

[87] Zhao, X., Park, N. G. (2015). Stability issues on perovskite solar cells. Photonics, 2(4), 1139–1151. https://doi.org/10.3390/photonics2041139

[88] Bryant, D., Aristidou, N., Pont, S., Sanchez-Molina, I., Chotchunangatchaval, T., Wheeler, S., Durrant, J. R., Haque, S. A. (2016). Light and oxygen induced degradation limits the operational stability of methylammonium lead triiodide perovskite solar cells. Energy and Environmental Science, 9(5), 1655–1660. https://doi.org/10.1039/c6ee00409a

[89] Chiang, Y. H., Anaya, M., Stranks, S. D. (2020). Multisource Vacuum Deposition of Methylammonium-Free Perovskite Solar Cells. ACS Energy Letters, 5(8), 2498–2504. https://doi.org/10.1021/acsenergylett.0c00839

[90] Pisoni, A., Jacimovic, J., Barisic, O. S., Spina, M., Gaál, R., Forró, L., Horváth, E. (2014). Ultra-low thermal conductivity in organic–inorganic hybrid perovskite CH3NH3PbI3. The journal of physical chemistry letters, 5(14), 2488-2492. https://doi-org.tudelft.idm.oclc.org/10.1021/jz501210

[91] Noh, J. H., Im, S. H., Heo, J. H., Mandal, T. N., Seok, S. Il. (2013). Chemical management for colorful, efficient, and stable inorganic-organic hybrid nanostructured solar cells. Nano Letters, 13(4), 1764–1769. https://doi.org/10.1021/nl400349b

[92] Tai, Q., You, P., Sang, H., Liu, Z., Hu, C., Chan, H. L. W., Yan, F. (2016). Efficient and stable perovskite solar cells prepared in ambient air irrespective of the humidity. Nature Communications, 7, 1–8. https://doi.org/10.1038/ncomms11105

[93] Soto-Montero, T., Soltanpoor, W., Morales-Masis, M. (2020). Pressing challenges of halide perovskite thin film growth. APL Materials, 8(11). https://doi.org/10.1063/5.0027573

[94] Howard, I. A., Abzieher, T., Hossain, I. M., Eggers, H., Schackmar, F., Coated and Printed Perovskites for Photovoltaic Applications. Ternes, S., Richards, B. S., Lemmer, U., Paetzold, U. W. (2019). Advanced Materials, 31(26). https://doi.org/10.1002/adma.201806702

[95] Chondroudis, K., Mitzi, D. B., Brock, P. (2000). Effect of thermal annealing on the optical and morphological properties of (AETH)PbX4 (X = Br, I) perovskite films prepared using single source thermal ablation. Chemistry of Materials, 12(1), 169–175. https://doi.org/10.1021/cm990516l

[96] Vaynzof, Y. (2020). The Future of Perovskite Photovoltaics—Thermal Evaporation or Solution Processing? Advanced Energy Materials, 10(48). https://doi.org/10.1002/aenm.202003073

[97] Liu, M., Johnston, M. B., Snaith, H. J. (2013). Efficient planar heterojunction perovskite solar cells by vapour deposition. Nature, 501(7467), 395–398. https://doi.org/10.1038/nature12509

[98] Zhao, D., Ke, W., Grice, C. R., Cimaroli, A. J., Tan, X., Yang, M., Collins, R. W., Zhang, H., Zhu, K., Yan, Y. (2016). Annealing-free efficient vacuum-deposited planar perovskite solar cells with evaporated fullerenes as electron-selective layers. Nano Energy, 19, 88–97. https://doi.org/10.1016/j.nanoen.2015.11.008

[99] Chen, C.-W., Kang, H.-W., Hsiao, S.-Y., Yang, P.-F., Chiang, K.-M., Lin, H.-W. (2014). Efficient and Uniform Planar-Type Perovskite Solar Cells by Simple Sequential Vacuum Deposition. Advanced Materials, 26(38), 6647–6652. https://doi.org/10.1002/adma.201402461

[100] Tavakoli, M. M., Simchi, A., Mo, X., Fan, Z. (2017). High-quality organohalide lead perovskite films fabricated by layer-by-layer alternating vacuum deposition for high efficiency photovoltaics. Materials Chemistry Frontiers, 1(8), 1520–1525. https://doi.org/10.1039/c6qm00379f

[101] Tavakoli, M. M., Yadav, P., Prochowicz, D., Tavakoli, R., Saliba, M. (2019). Multilayer evaporation of MAFAPbI3-xClx for the fabrication of efficient and large-scale device perovskite solar cells. Journal of Physics D: Applied Physics, 52(3). https://doi.org/10.1088/1361-6463/aaebf1

[102] Roß, M., Gil-Escrig, L., Al-Ashouri, A., Tockhorn, P., Jošt, M., Rech, B., Albrecht, S. (2020). Co-Evaporated p-i-n Perovskite Solar Cells beyond 20% Efficiency: Impact of Substrate Temperature and Hole-Transport Layer. ACS Applied Materials and Interfaces, 12(35), 39261–39272. https://doi.org/10.1021/acsami.0c10898

[103] Ono, L. K., Leyden, M. R., Wang, S., Qi, Y. (2016). Organometal halide perovskite thin films and solar cells by vapor deposition. Journal of Materials Chemistry A, 4(18), 6693–6713. https://doi.org/10.1039/c5ta08963h

[104] Longo, G., Gil-Escrig, L., Degen, M. J., Sessolo, M., Bolink, H. J. (2015). Perovskite solar cells prepared by flash evaporation. Chemical Communications, 51(34), 7376–7378. https://doi.org/10.1039/c5cc01103e

[105] Chen, Q., Zhou, H., Hong, Z., Luo, S., Duan, H. S., Wang, H. H., Liu, Y., Li, G., Yang, Y. (2014). Planar heterojunction perovskite solar cells via vapor-assisted solution process. Journal of the American Chemical Society, 136(2), 622–625. https://doi.org/10.1021/ja411509g

[106] Wang, S. (2014). How to UV Ozone Cleaning. https://chem.uiowa.edu/sites/chem.uiowa.edu/files/people/shaw/Scarlett-How%20to%20UV-OZONE%20Sep_15th.pdf

[107] Elseman, A. M. (2018). Organometal Halide Perovskites Thin Film and Their Impact on the Efficiency of Perovskite Solar Cells. Coatings and Thin-Film Technologies. https://doi.org/10.5772/intechopen.79678

[108] Schulze, P. S. C., Wienands, K., Bett, A. J., Rafizadeh, S., Mundt, L. E., Cojocaru, L., Hermle, M., Glunz, S. W., Hillebrecht, H., Goldschmidt, J. C. (2020). Perovskite hybrid evaporation/ spin coating method: From band gap tuning to thin film deposition on textures. Thin Solid Films, 704(October 2019), 137970. https://doi.org/10.1016/j.tsf.2020.137970

[109] Japan, T. S. S. S. O. (2018a). Compendium of Surface and Interface Analysis (Softcover reprint of the original 1st ed. 2018 ed.). Tokyo, Japan: Springer. https://doi.org/10.1007/978-981-10-6156-1

[110] Pazoki, M., Hagfeldt, A., Edvinsson, T. (2019). Characterization Techniques for Perovskite Solar Cell Materials (1st ed.). Elsevier. https://doi.org/10.1016/C2017-0-01993-6

[111] Rocha, F. S., Gomes, A. J., Lunardi, C. N., Kaliaguine, S., Patience, G. S. (2018). Experimental methods in chemical engineering: Ultraviolet visible spectroscopy—UV-Vis. Canadian Journal of Chemical Engineering, 96(12), 2512–2517. https://doi.org/10.1002/cjce.23344

[112] PerkinElmer. (2004). Applications and Use of Integrating Spheres With the LAMBDA 650 and 850 UV/Vis and LAMBDA 950 UV/Vis/NIR Spectrophotometers. https://www.perkinelmer.com/CMSResources/Images/ 44-74191APP_LAMBDA650IntegratingSpheres.pdf

[113] Benno, G., Joachim, K. (2003). Optical properties of thin semiconductor films. http://home.fnal.gov/ jkopp/tum/pdf/F/hl_spekt.pdf.

[114] Yan, J., Song, X., Chen, Y., Zhang, Y. (2020). Gradient band gap perovskite films with multiple photoluminescence peaks. Optical Materials, 99(October 2019), 109513. https://doi.org/10.1016/j.optmat.2019.109513

[115] Röhm, H., Leonhard, T., Schulz, A. D., Wagner, S., Hoffmann, M. J., Colsmann, A. (2019). Ferroelectric Properties of Perovskite Thin Films and Their Implications for Solar Energy Conversion. Advanced Materials, 31(26). https://doi.org/10.1002/adma.201806661

[116] Gauglitz, G., Moore, D. S. (2003). Handbook of Spectroscopy. Hoboken, NJ, United States: Wiley. https://doi.org/10.1021/ja033666c

[117] JEOL Ltd. (n.d.). JEOL Ltd. https://www.jeol.co.jp/en/

[118] Chauhan, A. (2018). Deformation and damage mechanisms of ODS steels under high-temperature cyclic loading. International Journal of Fatigue, 93, 1–17. https://publikationen.bibliothek.kit.edu/1000080339

[119] Tan, W., Bowring, A. R., Meng, A. C., McGehee, M. D., McIntyre, P. C. (2018). Thermal Stability of Mixed Cation Metal Halide Perovskites in Air. ACS Applied Materials and Interfaces, 10(6), 5485–5491. https://doi.org/10.1021/acsami.7b15263

[120] Xu, F., Zhang, T., Li, G., Zhao, Y. (2017). Mixed cation hybrid lead halide perovskites with enhanced performance and stability. Journal of Materials Chemistry A, 5(23), 11450–11461. https://doi.org/10.1039/c7ta00042a

[121] Jariwala, S., Burke, S., Dunfield, S., Shallcross, R. C., Taddei, M., Wang, J., Eperon, G. E., Armstrong, N. R., Berry, J. J., Ginger, D. S. (2021). Reducing surface recombination velocity of methylammonium-free mixed-cation mixed-halide perovskites via surface passivation. Chemistry of Materials, 33(13), 5035–5044. https://doi.org/10.1021/acs.chemmater.1c00848

[122] Pham, H. T., Duong, T., Rickard, W. D. A., Kremer, F., Weber, K. J., Wong-Leung, J. (2019). Understanding the Chemical and Structural Properties of Multiple-Cation Mixed Halide Perovskite. Journal of Physical Chemistry C, 123(43), 26718–26726. https://doi.org/10.1021/acs.jpcc.9b09035

[123] Da Silva Filho, J. M. C., Marques, F. C. (2018). Growth of Perovskite Nanorods from PbS Quantum Dots. MRS Advances, 3(32), 1843–1848. https://doi.org/10.1557/adv.2018.188

[124] Luo, S., Daoud, W. A. (2016). Crystal structure formation of CH3NH3Pbi3-xClx perovskite. Materials, 9(3), 1–13. https://doi.org/10.3390/ma9030123

[125] Kumar, Y., Regalado-Pérez, E., Ayala, A. M., Mathews, N. R., Mathew, X. (2016). Effect of heat treatment on the electrical properties of perovskite solar cells. Solar Energy Materials and Solar Cells, 157, 10–17. https://doi.org/10.1016/j.solmat.2016.04.055

[126] Girgsdies, F. Peak Profile Analysis in X-ray Powder Diffraction. Fritz-Haber-Institut der MPG. http://www.fhi-berlin.mpg.de/acnew/department/pages/teaching/pages/teaching__wintersemester__2015_2016/frank_girgsdies__peak_profile_fitting_in_xrd__151106.pdf

[127] Teuscher, J., Ulianov, A., Müntener, O., Grätzel, M., Tétreault, N. (2015). Control and Study of the Stoichiometry in Evaporated Perovskite Solar Cells. ChemSusChem, 8(22), 3847–3852. https://doi.org/10.1002/cssc.201500972

[128] Abzieher, T., Feeney, T., Schackmar, F., Donie, Y. J., Hossain, I. M., Schwenzer, J. A., Hellmann, T., Mayer, T., Powalla, M., Paetzold, U. W. (2021). From Groundwork to Efficient Solar Cells: On the Importance of the Substrate Material in Co-Evaporated Perovskite Solar Cells. Advanced Functional Materials, 31(42). https://doi.org/10.1002/adfm.202104482

[129] Jaysankar, M., Qiu, W., Bastos, J., Tait, J. G., Debucquoy, M., Paetzold, U. W., Cheyns, D., Poortmans, J. (2016). Crystallisation dynamics in wide-bandgap perovskite films. Journal of Materials Chemistry A, 4(27), 10524–10531. https://doi.org/10.1039/c6ta02769e

[130] Tai, M., Lau, C. F. J., Lin, H., Wang, Z. (2020). Advances in Phase Stability of Cesium Lead Halide Perovskites. Solar RRL, 4(12), 1–17. https://doi.org/10.1002/solr.202000495

[131] Qiu, W., Ray, A., Jaysankar, M., Merckx, T., Bastos, J. P., Cheyns, D., Gehlhaar, R., Poortmans, J., Heremans, P. (2017). An Interdiffusion Method for Highly Performing Cesium/Formamidinium Double Cation Perovskites. Advanced Functional Materials, 27(28), 1–9. https://doi.org/10.1002/adfm.201700920

[132] Ye, Q., Zhao, Y., Mu, S., Gao, P., Zhang, X., You, J. (2019). Stabilizing the black phase of cesium lead halide inorganic perovskite for efficient solar cells. Science China Chemistry, 62(7), 810–821. https://doi.org/10.1007/s11426-019-9504-x

[133] Burwig, T., Fränzel, W., Pistor, P. (2018). Crystal Phases and Thermal Stability of Co-evaporated CsPbX3 (X = I, Br) Thin Films. Journal of Physical Chemistry Letters, 9(16), 4808–4813. https://doi.org/10.1021/acs.jpclett.8b02059

[134] Beal, R. E., Slotcavage, D. J., Leijtens, T., Bowring, A. R., Belisle, R. A., Nguyen, W. H., Burkhard, G. F., Hoke, E. T., McGehee, M. D. (2016). Cesium Lead Halide Perovskites with Improved Stability for Tandem Solar Cells. Journal of Physical Chemistry Letters, 7(5), 746–751. https://doi.org/10.1021/acs.jpclett.6b00002

[135] Deretzis, I., Bongiorno, C., Mannino, G., Smecca, E., Sanzaro, S., Valastro, S., Fisicaro, G., Magna, A. La, Alberti, A. (2021). Exploring the structural competition between the black and the yellow phase of cspbi3. Nanomaterials, 11(5), 1–11. https://doi.org/10.3390/nano11051282

[136] Siegrist, S., Yang, S.-C., Gilshtein, E., Sun, X., Tiwari, A. N., Fu, F. (2021). Triple-cation perovskite solar cells fabricated by hybrid PVD/blade coating process using green solvents. http://arxiv.org/abs/2108.13794

[137] Rafizadeh, S., Wienands, K., Schulze, P. S. C., Bett, A. J., Andreani, L. C., Hermle, M., Glunz, S., Goldschmidt, J. C. (2019). Efficiency Enhancement and Hysteresis Mitigation by Manipulation of Grain Growth Conditions in Hybrid Evaporated-Spin-coated Perovskite Solar Cells. ACS Applied Materials and Interfaces, 11(1), 722–729. https://doi.org/10.1021/acsami.8b16963